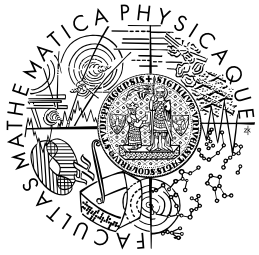

FACULTY
OF MATHEMATICS
AND PHYSICS
Charles University

DOCTORAL THESIS

RNDr. Denisa Kubániová

Magnetic nanoparticles of iron oxides for medicine

Department of low temperature physics

Supervisor of the doctoral thesis:	Assoc. Prof. Mgr. Jaroslav Kohout, Dr.
Study programme:	Physics
Study branch:	Physics of condensed matter and materials research

Prague 2024

I declare that I carried out this doctoral thesis on my own, and only with the cited sources, literature and other professional sources.

I understand that my work relates to the rights and obligations under the Act No. 121/2000 Sb., the Copyright Act, as amended, in particular the fact that the Charles University has the right to conclude a license agreement on the use of this work as a school work pursuant to Section 60 subsection 1 of the Copyright Act.

In Prague, 19 February 2024

Acknowledgment

In this important passage of the thesis, I wish to convey my appreciation for the numerous discussions I had with my colleagues to share our opinions and ideas. Although these conversations may have seemed unrelated or unproductive at the time, they ultimately shaped my current scientific and academic reality.

First of all, I would like to express my gratitude to my supervisor Assoc. Prof. Mgr. Jaroslav Kohout, Dr. for all the patient support and guidance from the very bachelor studies. Together with the consultants of this thesis, RNDr. Karel Závěta, CSc., RNDr. Jan Kuriplach, CSc., and Mgr. Vít Herynek, Ph.D., they provided valuable advice and suggestions during experimental and theoretical work, interpretation of the data, in fulfilling academic duties, as well as in the pathways of dissemination of original results and fundraising.

Furthermore, I would like to extend my gratitude to colleagues who contributed to the presented studies by synthesizing and coating the nanoparticles, conducting experimental work, offering consultations and valuable insights during manuscript preparation, as well as technicians who participated in design and construction of the Mössbauer probe and MPS device.

I would like to mention and thank all my friends and colleagues from the Laboratory of Mössbauer spectroscopy and Department of low temperature physics for a positive work environment they helped to create. Special thanks belong to RNDr. Tomáš Kmječ, Ph.D. for his work enthusiasm and technical assistance, and to Patrik Švančara, Ph.D. and Mgr. Emil Varga, Ph.D. for highly functional nature trips and coffee breaks and encouragement that kept me motivated to complete this extensive project.

I express my gratitude to Assoc. Prof. RNDr. Vojtěch Chlan, Ph.D. and Assoc. Prof. Mgr. Jiří Tuček, Ph.D., for their stimulating remarks and conscientious proofreading of the text of this doctoral thesis.

Moreover, I would like to thank my mother for her unwavering support during my academic journey and throughout the entire process of composing this thesis. I am grateful for those important moments spent with people who supported me greatly, even though they may never know the extent of their impact.

Title: Magnetic nanoparticles of iron oxides for medicine

Author: RNDr. Denisa Kubániová

Department: Department of low temperature physics

Supervisor: Assoc. Prof. Mgr. Jaroslav Kohout, Dr.,
Department of low temperature physics

Abstract: Magnetic nanoparticles of iron oxides, particularly those of ferric oxides, magnetite, substituted variants, including functional derivatives, have attracted significant interest because of promising capabilities in emerging diagnostic imaging methods and novel therapeutic interventions. In addition to the rapid development of syntheses and functionalization methods, a comprehensive understanding of their fundamental physical characteristics and the complex link among composition, microstructure, magnetic properties, and relaxation characteristics is pivotal for the rational design of well-defined magnetic nanoparticle systems. Generally, the magnetic behavior of nanoparticles deviates from bulk materials not only due to finite-size and surface effects but also by the occurrence of new crystal structures (polymorphs) and metastable states, such as non-equilibrium cation distribution. The doctoral thesis investigates the key physical characteristics of selected nanoparticle systems (simple ferric oxides of various crystal structure and morphology; Zn-, Co- and Mn-substituted magnetite-maghemite; coated by various hydrophilic and biologically inert surface layers), primarily by ^{57}Fe Mössbauer spectroscopy and supplemented by other available techniques. For that purpose, Mössbauer spectroscopy that employs the atomic nuclei as local probes to examine the hyperfine interactions with their electron shells is advanced for a specific use in nanoparticle research (in particular for magnetic particle suspensions in a frozen state). To evaluate the attributes of magnetic nanoparticle suspensions critical for applications in magnetic resonance imaging, magnetic particle imaging, magnetic hyperthermia, and targeted drug delivery, a magnetic particle spectrometer, an emerging method that exploits the nonlinear response of magnetic nanoparticle suspensions when subjected to an alternating magnetic field, was developed, with a broad spectrum of operating frequencies and magnitudes of the driving field.

Keywords: magnetic nanoparticles, iron oxides, theranostics, Mössbauer spectroscopy, hyperfine interactions, magnetic particle spectroscopy, Brown and Néel relaxation

Contents

1. Introduction

Magnetic nanoparticles, among other structures that are interesting in terms of application potential, are easily modifiable and economically obtainable on large scales. Besides the rapid development of syntheses and functionalization methods, understanding the complex link among composition (eventually stabilizing elements), microstructure (crystal structure, cation distribution, size, shape, and their dispersities) and even macrostructure (clustering, self-arrangement, etc.), magnetic properties (static and dynamic), and relaxation characteristics is pivotal for the rational design of well-defined magnetic materials and their applications in various fields and industries, from technical through environmental to biomedical. Generally, the magnetic behavior of nanoparticles deviates from their bulk counterparts not only due to finite-size and surface effects but also by the occurrence of metastable states, such as non-equilibrium cation distribution. Moreover, new polymorphs that are not observed in bulk might occur. At the same time, enormous variability of nanoparticle properties illustrates difficulties in one-to-one correlation of these parameters, as a fully characterized set of samples with variation in one feature alone is rarely found in the literature.

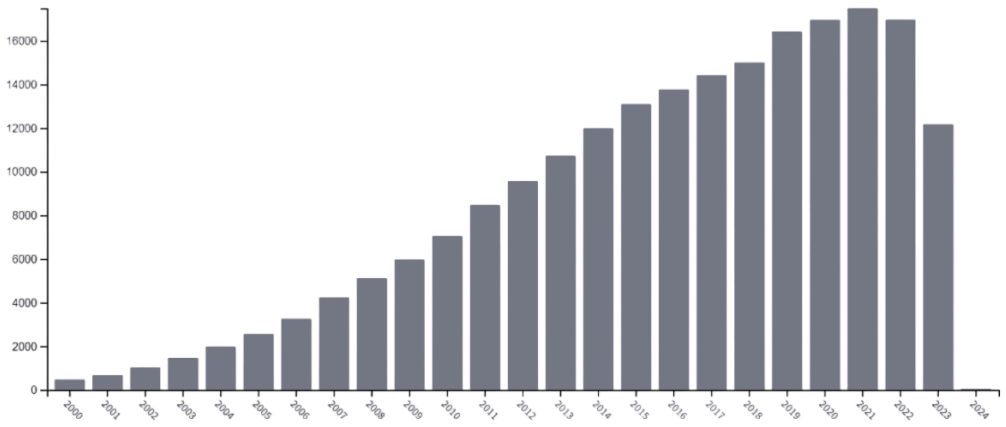

Figure 1.1: Occurrence of keyword 'nanoparticle' in Topic of the publications indexed in Web of Science Core Collection by year (212140 publications in total).

In addition to the quantitative approach in human medicine, modern biomedical research now shifts to individualized medicine and integration of diagnostic and therapeutic methods into a single approach, so-called theranostics, to reduce the load of drugs and procedures and associated health risks for the patient. Theranostic nanoparticles with magnetic cores could serve as contrast agents for magnetic resonance imaging (MRI), labeling agents for exceptionally sensitive magnetic particle imaging (MPI), heating mediators for self-regulated magnetic hyperthermia [1], and advanced drug delivery systems with magnetically triggered effects [2]. Simple iron oxide nanoparticles, namely maghemite, magnetite, and unstoichiometric materials between these two structurally related phases in a broad range of sizes and shapes, have been widely studied over the past two decades due to their low toxicity, ease of preparation, and extensive knowledge of their properties and biological effect. The specific requirements of advanced applications encourage further efforts to tailor the magnetic properties

of nanoparticles based on ternary and more complex compounds in search of ways to increase the magnetization or tune the magnetic anisotropy of particles by the selection of a convenient parent compound and suitable substitutions. Our recent studies have suggested various spinel ferrites, with ferrimagnetic ordering substituted with a diamagnetic cation with a particular preference for the tetrahedral site (here Zn^{2+}), including Co-Zn [3] and Mn-Zn [P8] ferrites, and substituted magnetite(maghemite) $Zn_cFe_{3-c}O_4$ phases that offer an excellent platform for the development of efficient contrast agents for magnetic resonance imaging due to increased magnetization. Magnetic cores for theranostic applications are commonly encapsulated with hydrophilic coatings (e.g. amorphous silica), providing a stable barrier around magnetic cores that ideally does not alter its properties, and a biologically inert surface that potentially allows further surface modifications.

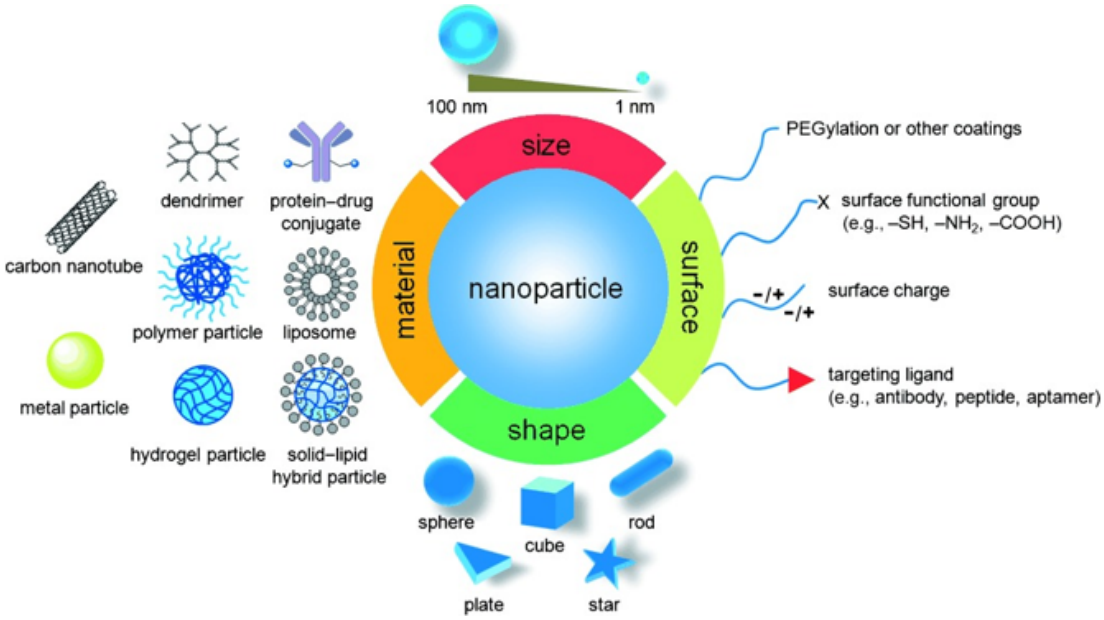

Figure 1.2: Strategies for nanoparticle functionalization for theranostic applications [4]. Reproduced with permissions from John Wiley & Sons, Inc.

The doctoral thesis focuses on magnetic nanoparticles of iron oxides for medical applications, exploring their fundamental properties with a brief mention of potential applications. The study aims to investigate key physical characteristics of selected nanoparticle systems based on ferric oxides and substituted magnetite, including crystal structure, cationic occupation of crystallographic positions, magnetic ordering, morphology, and size distribution. In addition to the general context, the introductory chapter of the thesis focuses on the application and advancement of ^{57}Fe Mössbauer spectroscopy (MS) as the main experimental technique, which utilizes atomic nuclei as local probes to examine hyperfine interactions within the studied systems, within the specific area of nanoparticle research, covering experimental, constructional, and theoretical aspects. The subsequent sections of the thesis delve into the detailed characterization and optimization of the magnetic properties of the studied iron oxide nanoparticles and their derivatives, primarily employing MS. The analyzes are supplemented by other techniques such as transmission electron microscopy (TEM), X-ray powder diffraction (XRPD), X-ray fluorescence (XRF), magnetic property measurements,

etc., and supported by density functional theory (DFT) calculations of electronic structures; however, these are not elaborated on extensively.

While working with nanoparticles of potential use as contrast agents in magnetic resonance imaging (MRI) [P8, P5] and magnetic particle imaging [P2], a new direction for the doctoral project emerged; thus the final chapters concentrate on magnetic particle spectroscopy (MPS), a novel method that exploits the nonlinear response of magnetic nanoparticle suspensions when subjected to an alternating-current (AC) magnetic field, demonstrating Brownian and Néel relaxation properties. A magnetic particle spectrometer, with a broad spectrum of operating frequencies and magnitudes of the driving field, was developed, tuned, calibrated, and tested to evaluate the attributes of selected magnetic nanoparticle suspensions intended for applications such as contrast agents in MRI, MPI, magnetic hyperthermia [5, 6], for drug delivery and its targeted release [7].

2. Applied methods of Mössbauer spectroscopy

2.1 Fundamental principles

Mössbauer spectroscopy exploits the Mössbauer effect (ME), i.e. a recoil-free resonant nuclear fluorescence discovered and explained by Rudolf Mössbauer [8] in 1958 who observed an anomalous increase in the resonance absorption of 129 keV γ-radiation by ^{191}Ir nuclei upon the temperature decrease during the work on his doctorate thesis [9–11]. The Mössbauer effect can be observed only for nuclei of specific chemical elements tightly bound in a crystal lattice, making it impossible to experiment with materials in gaseous or liquid phases and nearly-free ultrafine (quantum) objects. The key advantage of Mössbauer spectroscopy is its extreme relative energy resolution (e.g. $\sim 10^{13}$ for ^{57}Fe), which allows for a detailed investigation of hyperfine interactions of the nuclei with different electric and magnetic fields depending on the host lattice, possibly subjected to other external factors such as electromagnetic fields or stress, that causes shifts of nuclear energy levels and splittings of nuclear energy degenerate levels of the order of the natural linewidth. Unlike nuclear magnetic (quadrupole) resonance, which is sensitive to changes in the nuclear ground state (via transitions between levels in the ground state), Mössbauer spectroscopy is sensitive to changes in both the nuclear ground and excited states (via transitions between these two).

Hamiltonian $\mathcal{H}_{\mathrm{hf}}$ describing the hyperfine interaction [12] might be simplified in the form of

$$\begin{aligned} &\mathcal{H}_{\mathrm{hf}} = \mathcal{H}_{\mathrm{el}} + \mathcal{H}_{\mathrm{mag}} \\ &\langle \psi_{\mathrm{nuc}} | \mathcal{H}_{\mathrm{hf}} | \psi_{\mathrm{nuc}} \rangle = E_{\mathrm{el}}^{(0)} + E_{\mathrm{el}}^{(2)} + E_{\mathrm{mag}}^{(1)} + \textit{higher order terms}, \end{aligned} \tag{2.1}$$

where $\mathcal{H}_{\mathrm{el}}$ and $\mathcal{H}_{\mathrm{mag}}$ stand for the interactions of the nuclear charge distribution in an external electrostatic potential and the nuclear magnetic moment under the influence of a magnetic field, respectively, and ψ_{nuc} is the nuclear wave function. Taylor expansion of the electrostatic potential at the place of the nucleus leads to multiple dominant contributions [13], some of which will not affect the overall energy due to nuclear parity (terms $E_{\mathrm{el}}^{(2n+1)}$, $n \in \mathbb{Z}^{0+}$ non-negative integers including zero). Because $E_{\mathrm{el}}^{(0)}$, being the Coulomb energy of the point nucleus, will not contribute to the observed spectra, the only relevant term $E_{\mathrm{el}}^{(2)}$ given by the quadratic approximation of the electrostatic energy can be split further into the contributions of the electric monopole and the quadrupole interaction to the energy, $E_{\mathrm{el}}^{(2)} = E_{\mathrm{C}} + E_{\mathrm{Q}}$. The non-existence of magnetic monopoles gives only a magnetic dipole interaction energy $E_{\mathrm{mag}}^{(1)}$ as being relevant.

These are three dominant hyperfine interactions that determine the nuclear energy levels. The respective hyperfine parameters can be extracted from the Mössbauer spectra that show the transitions between the ground and excited states of the nuclei. The isomer shift δ, originating from the electric monopole interaction, is equal to the difference of the transition energies between the excited

state (ex) and the ground state (gr) of the nuclei in the absorber (A) and the source (S), respectively,

$$\delta = E_{\mathrm{A}} - E_{\mathrm{S}} = \frac{2\pi}{5} Ze^2[\langle r_{\mathrm{ex}}^2\rangle - \langle r_{\mathrm{gr}}^2\rangle][|\psi_{\mathrm{A}}(0)|^2 - |\psi_{\mathrm{S}}(0)|^2], \tag{2.2}$$

where $Ze\langle r^2\rangle$ characterizes the nuclear (isotropic) charge distribution (Z is atomic number, e electron charge) and $e|\psi(0)|^2$ is the electronic charge density at the nucleus. For the electric quadrupole interaction, the exact energies are available only for the nuclear state with the spin quantum number $I > 1/2$. The quadrupole interaction splits the fully degenerate ^{57}Fe excited level $|3/2, m_{\mathrm{I}}\rangle$ into two degenerate sublevels $|3/2, \pm 1/2\rangle$ and $|3/2, \pm 3/2\rangle$ based on the value of the nuclear magnetic spin quantum number m_{I}, leading to the splitting of the line in the Mössbauer spectrum into two, separated by a quadrupole splitting ΔE_{Q}, sometimes also designated as QS or simply Δ:

$$\begin{aligned} E_Q(|3/2, m_{\mathrm{I}}\rangle) &= eQV_{\mathrm{zz}} \frac{3m_{\mathrm{I}}^2 - I(I+1)}{4I(2I-1)} \sqrt{1 + \frac{\eta^2}{3}}, \\ \Delta E_{\mathrm{Q}} &= E_{\mathrm{Q}}(|3/2, \pm 3/2\rangle) - E_{\mathrm{Q}}(|3/2, \pm 1/2\rangle). \end{aligned} \tag{2.3}$$

Here, it is assumed that non-zero both the quadrupole moment of ^{57}Fe nuclei in the excited state and the largest component V_{zz} of the electric field gradient (EFG) tensor, given by the second derivatives of the electric potential at the nucleus $V_{\mathrm{ij}} = (\partial^2 V/\partial i \partial j)$ $(i, j \in \{x, y, z\})$, are non-zero. Only five of these components are independent because of the symmetric form of the tensor and Laplace's equation which requires the EFG to be a traceless tensor. In addition to V_{zz}, any EFG diagonalized by rotation to a principal axes system is specified by the asymmetry parameter $\eta = (V_{\mathrm{xx}} - V_{\mathrm{yy}})/V_{\mathrm{zz}}$, whose magnitude lies in the interval of $0 \leq \eta \leq 1$. The nuclear energy levels for pure magnetic dipole interaction are given by the Zeeman multiplet described by the first term in equation 2.4, where g_{N} is the nuclear Landé splitting factor (g-factor), μ_{N} nuclear magneton, and B_{eff} is an effective hyperfine magnetic field.

In the case of a much weaker electric quadrupole interaction compared to the magnetic dipole interaction, the diagonal elements of the total Hamiltonian matrix that describe the combined interaction in the first order of perturbation theory for a nucleus in a state $|I, m_{\mathrm{I}}\rangle$ are given as

$$\begin{aligned} \langle I, m_{\mathrm{I}}|\mathcal{H}_{\mathrm{mag,Q}}|I, m_{\mathrm{I}}\rangle = &- g_{\mathrm{N}}\mu_{\mathrm{N}} B_{\mathrm{eff}} m_{\mathrm{I}} \\ &+ \frac{eQV_{\mathrm{zz}}}{2} \frac{3m_{\mathrm{I}}^2 - I(I+1)}{4I(2I-1)} (3\cos^2\theta - 1 + \eta \sin^2\theta \cos 2\varphi). \end{aligned} \tag{2.4}$$

The magnitude of the quadrupole shift ϵ (or QS) of the $I = 3/2$ nuclear states depends on the polar θ and azimuthal φ angles between the principal axes of the EFG tensor and the direction of the effective hyperfine magnetic field at the nuclei. Having the $\vec{B}_{\mathrm{eff}}$ vector oriented in an arbitrary direction, the scaling factor can be visualized as the length of the vector that points from the atomic origin to the intersection of the $\vec{B}_{\mathrm{eff}}$ vector and the surface plot of the EFG tensor as shown by the example in figure 2.1.

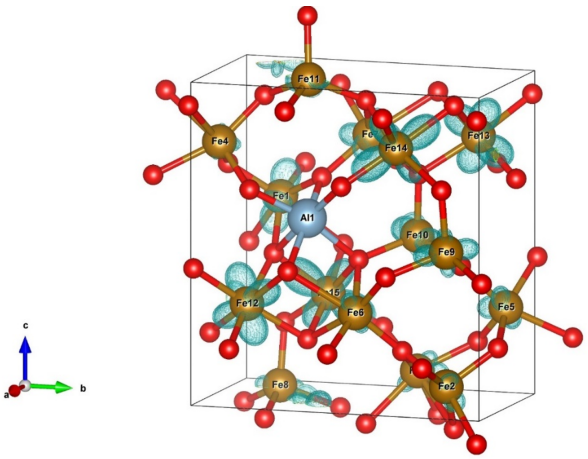

Figure 2.1: Surface plots (angular dependence of the first-order quadrupole shift of magnetically split Mössbauer spectrum) of the EFG tensors calculated by density functional theory (DFT) for Al-substituted ε-Fe_2O_3 with structural parameters similar to [P5].

The simplified picture of the effect of various shifts and splittings of the ^{57}Fe nuclear energy levels caused by basic hyperfine interactions on the observed Mössbauer spectra is presented in figure 2.2. The isomer shift reflects the oxidation (valence) state, spin state, ligand bonding states (covalent or ionic), and coordination number. The quadrupole splitting/shift offers insights into the local symmetry of the electronic charge distribution around the nucleus and can indicate the presence of noncubic crystal fields (linear, trigonal or square planar, square pyramidal, trigonal bipyramidal, distorted octahedra, tetrahedra, etc.). Complementary to the isomer shift, it also provides information on valence, spin state, and bonding. For the nuclei of ^{57}Fe exposed to a hyperfine field within the high-field approximation, only six transitions are allowed between the Zeeman split nuclear sublevels of the excited state and those of the ground state, according to the selection rules $\Delta I = 1$ and $\Delta m_{\mathrm{I}} = 0, \pm 1$. The magnetic splitting, and respective hyperfine magnetic field, are informative on the magnetic structure of the material, including the magnitude and direction of the magnetic moments.

2.2 Experimental equipment

The long-lived radioactive parent isotope ^{57}Co is typically used for observations of the Mössbauer effect (ME) in a stable isotope of ^{57}Fe. ^{57}Co decays into the ^{57}Fe excited state of nuclear spin $I = 5/2$ with a halflife of 271.74(6) days, initially caused by K-shell electron capture. Subsequently, the nucleus decays to the ground state with $I = 1/2$ directly by emission of 136 keV photon with probability of 9 % , or via multistep emission through a metastable state (Mössbauer level) that emits a 14.4 keV γ-photon with a halflife of 97.8 ns. For the ^{57}Fe Mössbauer spectra acquisition, the ^{57}Co source diffused into a Rh matrix (activity 50 mCi or 100 mCi) moving forth and back in line with the absorber with constant acceleration was employed. An unfolded Mössbauer spectrum represents the detected count rate plotted as a function of the channel number that is synchronized with the immediate velocity of the transducer, which modifies the energy of the emitted γ-photon due to the Doppler effect (mm/s $\sim$ neV). The velocity (energy) range of the spectrometer can be adjusted by setting the maximal velocity (up to $\pm$ 300 mm/s with standard guide springs) and the number of channels (up to 4096) of the multichannel analyzer.

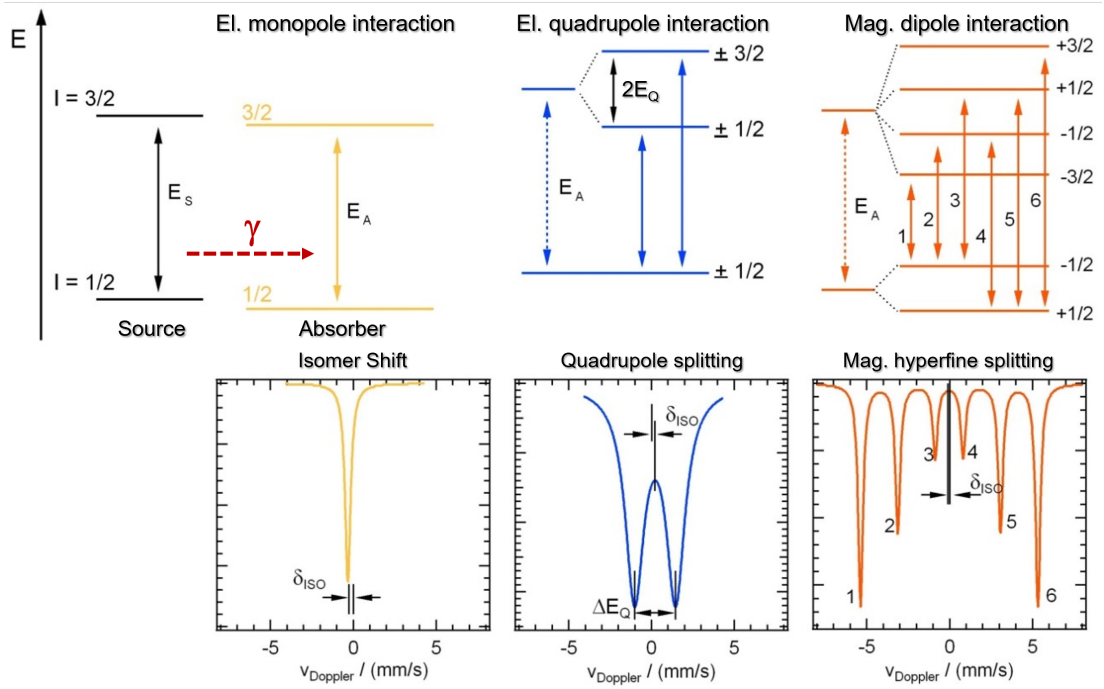

Figure 2.2: (Top) nuclear energy levels of ^{57}Fe nuclei displaced by the electric monopole interaction, and split by the electric quadrupole interaction or by the magnetic dipole interaction (Zeeman splitting) in this order from left to right, (bottom) respective Mössbauer spectra shape and hyperfine parameters (isomer shift δ_{ISO} and quadrupole splitting ΔE_{Q}). Adapted from [14].

All of the experiments presented in this work were realized with a transmission geometry in which we detect absorption spectra of primary γ-rays from the source by the purpose-designed gas or scintillator detector, each providing specific advantages. Although the gas detector provides a higher energy resolution, the scintillator stands out by higher detection efficiency and shorter dead time. Besides, the Laboratory of Mössbauer spectroscopy (see web domain mossbauer.cz) offers Conversion Electron (CEMS) and X-ray Mössbauer spectroscopy (CXMS) options realized in reflection geometries, in which the information about hyperfine interactions is contained in the secondary γ-ray originating from the absorber volume. The measurement time varies for each setting to reach reasonable data statistics, that is, the quality of the spectrum is given by the signal-to-noise ratio (SNR) defined as $(N_{\mathrm{max}} - N_0)/\sqrt{N_{\mathrm{max}}}$, where N_0 and N_{max} are the count numbers in and out of the resonance. The effect of the spectrum, referred to later in the text, is defined as $(N_{\mathrm{max}} - N_0)/N_{\mathrm{max}} \times 100\%$. The velocity calibration of WissEL spectrometers [15] was performed by means of a standard 12.5 µm α–Fe (i.e. metallic iron) foil by Goodfellow [16] - isomer shifts are given relative to this standard at 296 K.

Thermal anchoring of the whole volume of the sample to the heater and temperature sensor might be a source of relatively significant errors in determining the actual experimental temperature, and the samples might supposedly present themselves with different hyperfine parameters and other characteristics of the spectra than expected. This might become very obvious for e.g. material with strong temperature dependence of hyperfine parameters or a voluminous sus-

Figure 2.3: Air-tight sample holder (left) and suspension holder (very right) for Mössbauer spectroscopy experiments in the whole temperature range provided by the spectrometers. The sample stability during the experiment was tested down to 4.2 K and theoretically can reach up to a melting point of the indium seal or temperature limit of the installed temperature probe.

pension of particles with distributions of particle size and/or magnetocrystalline anisotropy. To ensure proper thermal anchoring and homogeneous temperature in the sample volume, the sample container was made of highly thermally conductive material, pushed tightly against the probe using a mediating indium layer, and the beam-facing surfaces were covered with aluminum foil (containing small amounts of diluted Fe) to eliminate temperature gradients in the sample volume as much as possible. For rapidly oxidizing samples, where it is necessary to prevent access to air, a similar approach was employed in the construction of an air-tight sample holder shown in figure 2.3. In a glove box, an aluminum sheet is pressed together with indium wire sealant against an aluminum cup filled with a sample and secured by screws. To further increase the efficiency of the use of experimental time, given the limitations of the available cryostat, we recently designed and constructed a two- and three-sample gilded copper holder (shown in figure 2.4) and augmented the probe with a stepper motor with a linear guide for automated positioning of the sample into the γ-beam.

For each sample, tens of milligrams of powdered particles were measured as such or encapsulated in aluminum foil, both to create a uniform layer with a diameter of 8 mm. The holder with the sample was directly bolted onto a transducer unit with a radioactive source for room-temperature experiments or, in case of low-temperature experiments, onto a dedicated probe that was subsequently handled according to cryostat specifications. For samples that are liquid at room temperature (water and oil suspensions, hydrated particles of consistency of mud, etc.), an aliquot of hundreds of microliters of suspension was pipetted under oxic conditions into a brass sample container (see figure 2.3), sealed with Mylar foil, and frozen in vapor above liquid nitrogen temperature (close to 77 K) shortly before measurement in a helium bath cryostat. Although multiple setups were available at the time in the laboratory, the experiments in two cryostats are presented in this work only.

The helium bath cryostat by Janis Research Co. Model 12CNDT-6T with Mössbauer insert operates in the temperature range of 4.2-300 K and allows for the application of an external magnetic field up to 6 T oriented perpendicularly to the γ-beam [17]. The upper temperature limit is constrained mainly by the specifics of the Cernox temperature probe [18]. In reality, experiments above approx. 200 K are significantly affected by vibrations originating in the boiling of liquid helium in the inner shield, leading to spectral line broadening. Experiments at increased temperature require that the heat exchange gas is pumped out of the sample space (as low as $\sim 10^{-6}$ mbar) to decrease the evaporation of cryogenic

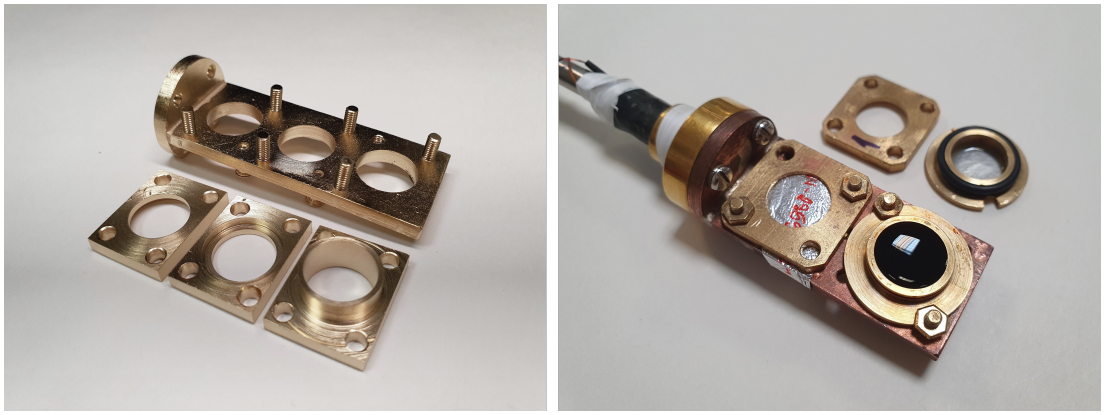

Figure 2.4: Multiple-sample holder extensions for the existing cryostat probe.

liquids (mainly LHe) and the cost of experimental time.

The liquid nitrogen finger cryostat of homemade design [19] is constructed to operate within temperature range of 93-300 K. In contrast to the bath design mentioned above, the sample is mounted on a copper plate thermally anchored directly to the outer casing of the finger submerged in liquid nitrogen stored in the Dewar vessel. This construction requires the sample space to be pumped before any operation (maximum reachable vacuum of $\sim 10^{-4}$ mbar) which makes it difficult to work with suspensions that need to be frozen in dry air before pumping.

For measurement on a well-tuned spectrometer, the experimental error is estimated as half of the channel, which, for a standard velocity resolution of 24 mm/s per 1024 channels for an unfolded spectrum, gives ~ 0.012 mm/s. Apart from the experimental error, the hyperfine parameters are prone to statistical errors arising from the fit of the spectrum. Systematic errors are hard to recognize. Previous scientific experience with the material and specifics of a fitting software plays a significant role in the determination of leading parameters that model the acquired spectra.

2.3 Spectra processing methods

Hyperfine parameter fits, using a standard least-squares fit routine, were performed with interactive Confit2000 software [20], MossWinn [21] and SpectrRelax software [22]. Each software provides some advantages and disadvantages compared to each other and toward other available solutions and code packages worldwide. Apart from user-friendly GUI and reporting, the field of use and implied limitations of the software are mainly predetermined by the mathematical and numerical strategy [23–26] to decompose a spectrum and calculate the respective control parameters, and approximate models of physical reality available [27–30]. In most cases, the acquired spectra can be viewed differently from different perspectives (availability of data from other characterization methods, personnel experience in the specific field of material research, objective for data analysis) and modeled accordingly. Reasoning for the use of specific software or methodology for each study presented is justified in the next chapters.

The Mössbauer spectral line is usually modeled by a theoretically justified

Lorentz-line shape, or pseudo-Voight profile (linear combination of Lorentz and Gauss-line shape) that renders the observed spectral lines with a higher accuracy. The reasoning behind line shapes can be found elsewhere [31, 32]. The asymmetric line broadening can be explained by the distribution of local environments of the resonant iron ions, which might be a result of small particle size, imperfect crystallinity, deviations from stoichiometry, chemical impurities, surface effects, and/or second- and higher-order corrections. There are several approaches to modeling the spectra with such broadenings - (1) a model-free approach which uses a large set of superposed spectral components, whose hyperfine parameters vary in discrete steps with additional restrictions imposed on shared control parameters, (2) a hypothesized model comprised of a minimal number of superposed spectral components that reasonably well fits the data and allows one to promptly estimate desired parameters with a reasonable error, (3) a physically correct model that allows for detailed interpretation of acquired spectra; however, it is time-consuming, and as a rule of thumb it must be supported by supplemental information from relevant characterization methods. As fundamental science is centered on the exploration and description (and, figuratively speaking, exploitation) of physical reality to the extent of what is achievable at the given moment and beyond, we tend to the third option whenever possible.

When more information on the physical and chemical properties of the studied material is available from complementary characterization methods (e.g. chemical composition, crystal structure, stoichiometry, distributions in size or other properties) over a wider range of experimental parameters (temperature, external magnetic field, pressure, specific atmosphere, etc.), one tends to develop and deploy a physical model that ought to capture all the observed tendencies. Unless some structural transition affects the electron density in the nuclei, the contribution of the second-order Doppler shift δ_{SOD} causes a gradual decrease in isomer shifts δ with increasing temperature (see equation 2.5, where k_{B} is Boltzmann constant, E_γ transition energy, M_{eff} effective mass that takes into account collective motions of the Mössbauer atom together with its ligands, c is speed of light in vacuum, θ_{M} Mössbauer temperature, and T temperature) [13]. In practice, δ_{SOD} may already be negligible at the liquid helium temperature (4.2 K). Then,

$$IS = \delta + \delta_{\mathrm{SOD}} = \delta - \frac{9 k_{\mathrm{B}} E_\gamma}{16 M_{\mathrm{eff}} c^2} \left(\theta_{\mathrm{M}} + 8T \left(\frac{T}{\theta_{\mathrm{M}}} \right)^3 \int_0^{T/\theta_{\mathrm{M}}} \frac{x^3}{e^x - 1} \, \mathrm{d}x \right). \tag{2.5}$$

Similar behavior can also be observed for the quadrupole shift/splitting, which is given by the magnitude of the electric field gradient at the nucleus and reflects a local symmetry of the electron system: in the first approximation, the QS of Fe(III) cations remains constant with increasing temperature, while that of Fe(II) decreases as a polyexponential function [13, 33]. The hyperfine magnetic field at the nuclei follows the evolution of magnetization. For iron compounds, it reaches tens of Tesla because of a strong Fermi (contact-type) interaction and other minor contributions originating from the interaction with the spins and orbital moments of electrons from the electron shell and magnetic dipole-dipole interaction with magnetic moments of surrounding atoms. With some exaggeration, one could claim that the set of hyperfine parameters is a fingerprint for experimentally distinguishable phases.

$$f(T) = \exp\left[\frac{-3E_\gamma^2}{k_\mathrm{B}\theta_\mathrm{D}Mc^2}\left(\frac{1}{4}\left(\frac{T}{\theta_\mathrm{D}}\right)^2\int_0^{\theta_\mathrm{D}/T}\frac{x}{e^x-1}\,\mathrm{d}x\right)\right] \tag{2.6}$$

The assumption of equality of the Lamb–Mössbauer (f) factor and its temperature evolution (given by the equation above, where θ_D is Debye temperature) for non-equivalent Fe crystallographic sites (that is, the probability of recoil-free absorption of the incident photon), commonly used to relate the relative spectral area I of the fitted components to the relative site occupancy and thus also to the sample composition, is not always met for compounds containing both ferric and ferrous ions [34–37]. As a direct consequence, the absolute values of the relative spectral area I, determined from Mössbauer spectra, systematically overestimate the molar content of Fe(III) (at 296 K up to $\sim$ 16 a.u.%). On the other hand, the I values can be used to demonstrate the comparability of structurally similar compounds such as those presented here. In eligible cases, some spectral parameters are shared among spectral components (subspectra) to decrease the degrees of freedom of the model – commonly, in equal relative intensity and linewidth of doublet lines when no preferred orientation (texture) or Goldanskii-Karyagin effect (anisotropic recoil-free fraction) is expected [34, 38]; below a magnetic ordering temperature, in equal linewidth of individual lines of sextets, in spectral area ratio of 3:2:1:1:2:3 if random orientation of magnetic moments (fields) typical for powders is suggested by the fit; and in many others where reasonable.

The majority of spectrometers in operation modify the shape of spectra (so-called spectrometer function that is convoluted with the physical spectrum) or contain impurities in the path of the spectrometer that are necessarily detected as additional signal. In our results, a doublet components in the central part of Mössbauer spectra acquired at room temperature model the contribution of a paramagnetic Fe(III) diluted in aluminum foil covering the detector (where present) and in aluminum foil used to contain and thermally anchor the sample (if used). The parameters of Fe from detector-covering foil are as follows: IS = 0.17(3) mm/s, quadrupole splitting QS = 0.48(5) mm/s, absolute intensity $\sim$ 0.1 %, line intensity ratio $I_2/I_1 = 1.44(2)$. The parameters of Fe from sample-covering foil evolve with temperature; at room temperature, they are: IS = 0.32(3) mm/s, QS = 0.34(9) mm/s, Γ = 0.32(2) mm/s, relative intensity <1 %, line intensity ratio $I_2/I_1 \in \langle 1, 1.75\rangle$, caused by the texture imprinted by a foil rolling in dependence on the tilt angle with respect to γ-beam due to a variation in the angle θ_q between the propagation direction of the γ-rays and the principal axis of the EFG, $I_2/I_1 = (1+\cos^2\theta_\mathrm{q})/(2/3\sin^2\theta_\mathrm{q})$. In most cases, the neglection of these contributions does not lead to significant deviations in the results. If an external magnetic field is applied, the latter doublet is split into a sextet with the same isomer shift as would be observed at that respective temperature, the quadrupole shift approaches 0 mm/s, and the hyperfine field B_eff follows the magnitude of the applied field up to 6.2(2) T.

2.4 Mössbauer spectroscopy of nanoparticles

The development of instrumentation and methods that allow for a detailed investigation of nanostructures has led to an increase in scientific interest in this field over the past few decades (see figure 1.1). Mössbauer spectroscopy advances over other physical characterization methods that fail in the range below $\sim$ 10 nm because, as a local nondestructive method, it does not require long-range order and can be utilized in a laboratory setting from an operational point of view. The Mössbauer isotope, structurally bound in the investigated material, offers a local center to probe the hyperfine interactions that are modulated by close sources (electron density around the nucleus, uncompensated spins, local anisotropy, chemical impurities, intraparticle interactions, etc.) as well as more distant ones (interparticle interactions) [39]. Mössbauer spectroscopy offers, similarly to other local, ab initio, and DFT-based methods, a view from within the material that can be correlated with the macroscopic properties that the material exhibits at larger scales.

The surface layers of any finite material are often structurally and magnetically disordered and represent a break of symmetry (a boundary) in a perfect crystal lattice. As the size of the material is reduced towards nanoscales, their relative share over volume of a particle increases, and the overall material properties are affected in such a way that completely new and unexpected chemical and physical properties appear that were not previously observed in the bulk counterparts. Some examples studied in more detail in this work might be the occurrence of metastable materials (see Chapter 3), metastable states due to an unbalanced distribution of cations in a structure, superparamagnetism as a collective behavior of nanoparticle spins (for both, see Chapter 4), or quasi-discrete band structure.

The size reduction and respective consequences (see figure 2.5) imply changes

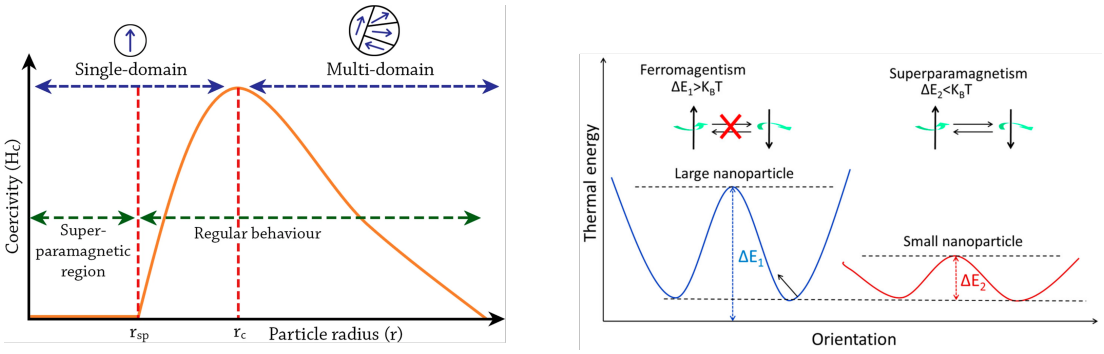

Figure 2.5: (Left) effect of nanoparticle size on magnetic coercivity. Below the critical radius r_c, all magnetic spins in the nanoparticle align to one direction and nanoparticles possess single magnetic domain structures because it is energetically favored for the nanoparticle to exist without domain walls. In order to be superparamagnetic, the nanoparticle radius has to be lower than the threshold radius for superparamagnetism r_{sp}, i.e. where thermal fluctuations overcome the energy barrier for spinflip given by the magnetocrystalline energy. (Right) the energy levels of magnetic nanoparticles with the size between r_c and r_{sp} (large), and below r_{sp} (small). Adapted from [40] and [41].

in observed spectra that might not always be fully decoupled into the contributions/effects of various origin since there is usually no or limited a priori information on the material and on the translation of the material characteristics into hyperfine interactions and shape of the spectrum. Minor spectral components and/or minor effects might be covered by major spectral components and/or major effects, in contrast to superimposed, well-discernible spectral components and effects. Even when discerned, their parameters might correlate strongly and be burdened by high relative errors. On the other hand, some contributions cannot be well described due to the lack of accurate descriptive models. In all cases, the fitting of the spectrum represents a numerical procedure of finding the global minimum in a multiparameter space that poses a problem of its own, and each software applies various approaches to tackle this with a limited computational resources and time.

Specific to (nano)particles and the superparamagnetic (SPM) state is the blocking temperature at which the thermally induced oscillating particle superspin is frozen into the direction with minimum energy (determined by competing magnetocrystalline anisotropy energy $\Delta E = K_{\text{eff}}V$ and external factors such as electromagnetic fields or stress). Apart from the crystallite dimensions, the blocking temperature decreases with decreasing strength of interparticle magnetic dipole interaction (i.e. the distance between particle cores caused by coverage of particles by nonmagnetic shell and/or their concentration in suspension). There is contradicting information in the literature on the strength of the interparticle distance effect on the blocking temperature for, e.g., antiferromagnetic particles, ranging in the order of tenths to tens of Kelvin, to mention some [42, 43]. The time window of Mössbauer spectroscopy is given by the halflife of the excited Mössbauer level, which decays by a radiative transition to the ground state ($\tau_{\text{MS}} \sim 1.43\times10^{-7}$ s). When the blocking temperature is approached from below, the nanoparticle gradually loses its internal magnetic order and becomes superparamagnetic. The spin relaxation time ($\tau \sim 10^{-8}$-10^{-7} s) is given by the well-known equation [44] in the form of

$$\tau = \tau_0 \exp\left(\frac{K_{\text{eff}}V}{k_{\text{B}}T}\right), \tag{2.7}$$

where τ_0 is the material constant ($\sim 10^{-12}$-10^{-9} s), K_{eff} is the magnetocrystalline anisotropy, V is the volume of a particle, k_{B} is the Boltzmann constant and T is the temperature. In the temperature dependence of the Mössbauer spectrum, this is manifested by a dropping contribution of (sharp) sextets to the spectrum, with the doublet contribution emerging simultaneously. In the transition region, the increased spin fluctuation rate leads to a rapid decrease of hyperfine fields and a change in quadrupole shifts. For the nuclei of ^{57}Fe in the limit of the high-field condition described in Section 2.1, one would observe a gradual collapse of two outermost lines and four inner lines separately into a two-line spectrum or a single-line spectrum in the absence of electric quadrupole interaction.

To describe the relaxation effects observed in Mössbauer spectra, Blume and Tjon [29] as the first applied the stochastic theory developed by Anderson for all possible orientations of the magnetization of a SPM particle with a spin S with respect to the quantization axis explicitly in the calculation of the Mössbauer

line shape [45]. Compared to the Blume-Tjon model provided by MossWinn software, the many-state relaxation model developed by Jones and Srivastata [30] available in SpectrRelax software does not include the assumption of the random-phase approximation that Dattagupta and Blume used in their treatment of superparamagnetism as a many-state relaxation problem [46]. Even though this model is the best option implemented so far, it sometimes also fails to provide a reasonably well fit because of the primary assumptions included during its development (e.g. uniaxial anisotropy) and uncertainties in the determination of some parameters.

Almost every software treats distributions of static hyperfine parameters found in nanoparticle systems to some extent using an extended Voigt-based analytic lineshape that treats an arbitrary-shape partial distribution in the form of a sum of Voigt lines using a model of the total probability density distribution. In contrast to the other mentioned software, user-friendly Confit2000 allows only for a symmetric (Gaussian-like) distribution that performs well in the cases of high correlation between spectral subcomponents fitted to the overall shape of the spectrum and allows for simplifying physical interpretation. On the other hand, it lacks a wide range of options for parameter binding introduced by two other software and a possibility to solve the static Hamiltonian of mixed magnetic and electric hyperfine interactions in the case of violation of high-field condition.

Another model relevant in Mössbauer analysis of nanoparticles is the magnetic core-shell model (MCS) first suggested by Coey [47] for $\sim$ 8-nanometer particles of γ-Fe_2O_3 and further developed during the bachelor project [48] regarding nanoparticles of ε-Fe_2O_3. Since the particles of non-ellipsoidal shape cannot be homogeneously magnetized, the spin arrangement in the particles is certainly not collinear. Crystal lattice vacancies and breaks of bond periodicity in the surface layer of nanoparticles lead to increased atomic disorder and, through exchange and dipole-dipole interaction, cause the magnetic moments of boundary and deeper layers to deviate from their normal direction. Moreover, to minimize the surface energy of the single-domain particle, the magnetic moments in the surface layer spontaneously rotate to close the magnetic flux that the particle generates. The MCS model assumes that a particle has a core with a collinear spin arrangement and a surface layer (shell) in which the spins of the ions are inclined at some angle to their normal direction, which depends on their magnetic nearest neighbors. For the deconvolution of the Mössbauer spectra of the ε-phase of Fe_2O_3 (components S_2-S_5 in the representative Mössbauer spectrum presented in figure 2.6), instead, we assumed randomly oriented magnetic moments in the shell.

The intensity of the spectral lines is divided among two subspectra - one ascribed to collinear ordered magnetic moments in the core and another to randomly oriented magnetic moments in the shell of nanoparticles. Generally, the magnetic surface layer may be thicker than the crystallographic one; the iron nuclei in the magnetic shell have the same electron density at the nuclei as those in the core, and hence we suppose the same isomer shifts for the corresponding core and shell components. This assumption is broken for a few outermost layers; however, this has a negligible effect on the spectra. Due to the random canting of magnetic moments in the shell, the average quadrupole shift for the shell components, given by the integration of the second term in the Hamiltonian (equation 2.4) over

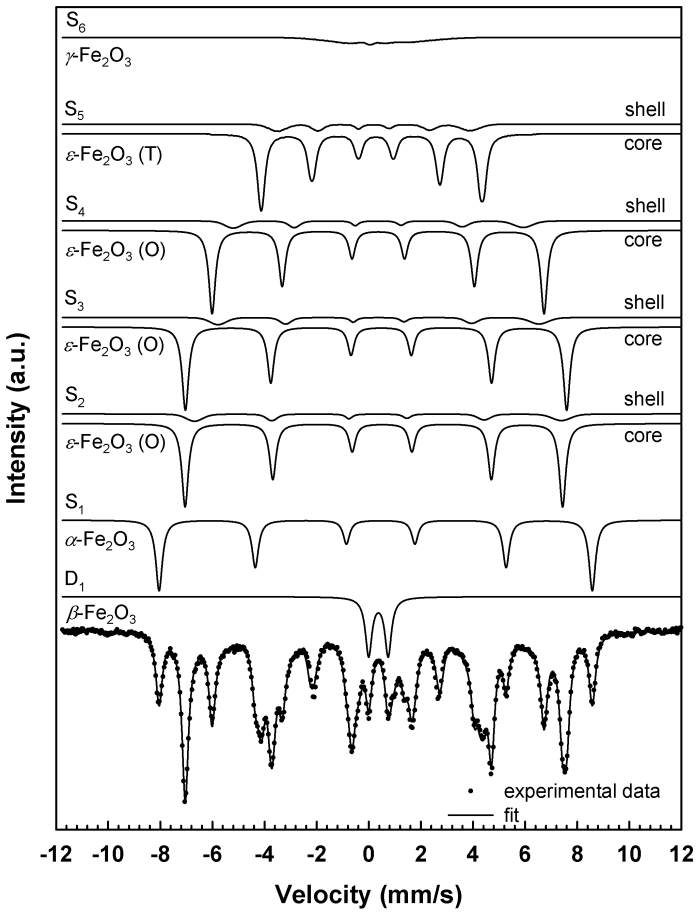

Figure 2.6: Deconvolution of a representative Mössbauer spectrum of Fe_2O_3 nanoparticles homogeneously dispersed in SiO_2 matrix recorded at room temperature using magnetic core-shell model (40%@1125 sample described in more detail in the reference [P6] and Section 3.1).

space angles, gives a zero value, and the mean value of the hyperfine magnetic field shifts to lower magnitudes. As a result of the hyperfine field anisotropy, the spectral components exhibit the distributions of hyperfine magnetic field, the shape of which is kept the same for all the shell components as a simplification. Considering all these assumptions results in a significant decrease in the number of free parameters of the model.

For in-field spectra, the ratio of spectral line intensities b given by the mean angle between the γ-beam and the $\vec{B}_{\mathrm{eff}}$ vector

$$b = I_{2,5}/I_{3,4} = 4\sin^2\theta_{\mathrm{m}}/(1+\cos^2\theta_{\mathrm{m}}) \tag{2.8}$$

would equal to 4 in the aligned core and 2 in the disordered shell [12]. Due to the enhanced anisotropy at the surface, even an external magnetic field as high as 6 T might not be sufficient to align all magnetic moments in the shell with the direction of the applied field, which is perpendicular to the γ-beam in the experimental setup employed. As a consequence, a certain deviation of the mean angle θ_{m} from 90° occurs with increasing surface-to-volume ratio [P3].

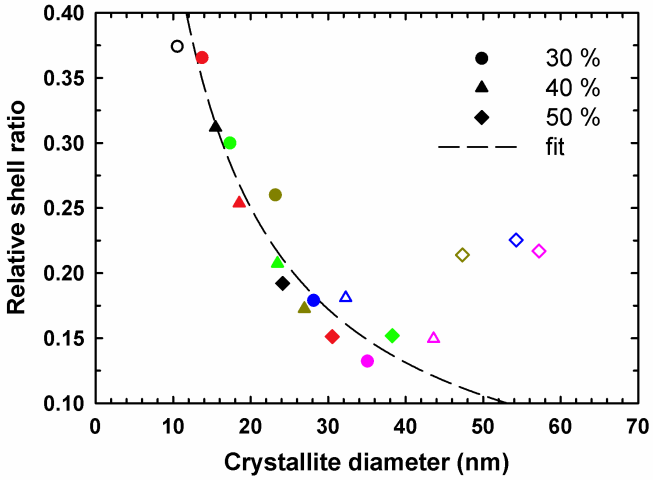

Figure 2.7: Relative content of the magnetic shell layer volume in ε-Fe_2O_3/SiO_2 nanoparticles (determined by MS) prepared by the sol-gel method as a function of mean diameter of the particles (determined by XRPD). Only filled data points were used for the fit, others were omitted due to reasons explained in [P6]. The shapes of the data points correspond with the Fe_2O_3 mass fraction in the initial mixture of a single precursor in which both functional groups for silica matrix and iron oxide were present while colors correspond with the annealing temperature.

In finer particles, the above defined shell represents a significant part of the volume and has a non-negligible effect on the macroscopic magnetic properties [P6, P9]. If we would consider the ε-Fe_2O_3 nanoparticles spherical and assume that the thickness of the shell does not change with the size of the nanoparticle, the fit of the data presented in figure 2.7 leads to a shell thickness of 1.83(5) nm. Another explanation of the lineshape asymmetry toward smaller hyperfine magnetic fields might be that Si cations from the silica matrix become embedded in the structure of nanoparticles during nucleation. However, follow-up studies (not presented here) of high-purity ε-Fe_2O_3 nanoparticle composite described in Chapter 3 by TEM and ab initio calculations have not yet provided clear evidence for this hypothesis. The possibility of some canting of the magnetic moments in the core of the particles cannot be excluded, as there is likely to be an extra, random concentration of vacancies, which can be appreciable in the smallest fraction in the size distribution.

A strong correlation of fit parameters often does not allow to unambiguously resolve the Mössbauer spectra of nanoparticles with multiple components of close magnitudes of hyperfine magnetic field B_{hf} in particular, such as those presented here. The application of an external magnetic field B_{ext} of sufficient strength to overcome the magnetocrystalline anisotropy energy causes the magnetic moments in the sample to align in the direction of the applied field to minimize their magnetic energy. If the magnetic moments in magnetic sublattices are coupled antiferromagnetically (case of e.g. ferrimagnetic order), the effective hyperfine magnetic fields acting on the ^{57}Fe nuclei in each magnetic sublattice are proportionally shifted in an opposite direction according to the result of $\vec{B}_{\mathrm{eff}} = \vec{B}_{\mathrm{hf}} + \vec{B}_{\mathrm{ext}}$, which might promote the separation of the spectral components.

3. Ferric oxide nanoparticles

Iron oxides in all their various forms are one of the most widely used metal oxides with various applications in both scientific and industrial fields [49]. Ferric oxide nanoparticles have interesting magnetic, catalytic, biochemical, and other properties that make them suitable for specific technical, environmental, and biomedical applications [50]. Under ambient conditions, ferric oxide (Fe_2O_3) occurs in five crystalline polymorphs with significantly different structural and magnetic properties - α-, β-, γ-, ε-, and ζ-Fe_2O_3 - even though the last one is prepared under high pressure [51]. While the crystalline α-Fe_2O_3 and γ-Fe_2O_3 can be found in nature as minerals hematite and maghemite, β-Fe_2O_3 and ε-Fe_2O_3 are almost exclusively produced in research laboratories. An exhaustive description of each polymorph can be found in [48, P6].

3.1 Identification of polymorphs

Admixtures of multiple polymorphs typically occur in the synthesized ferric iron nanoparticles. In order to prepare a product suitable for high-tech applications, it is necessary to precisely control the phase purity, nanoparticle size, and distribution width. In the paper [P6] we show that a single characterization method, with its specific advantages and limitations, is not sufficient for the identification of ferric oxide polymorphs in nanoparticles. Only a combination of complementary methods can provide sufficient comprehensive information; in our particular case, we employed the synergy of XRPD, direct-current (DC) magnetic measurements, and Mössbauer spectroscopy. Specifically, we report the effects of annealing temperature T_a and Fe_2O_3 mass fraction w_f in the initial mixture of precursors on the composition of ferric oxide nanoparticles in the nanocomposite, prepared by the sol-gel method. In the following text, the samples are denoted as $w_f@T_a$. For each sample, the color of the curves within different figures is kept the same.

TEM of Fe_2O_3 nanoparticles, presented in figure 3.1, evidences for nanoparticles of various shapes, from globular to rod-shaped, homogeneously dispersed in an amorphous silica matrix. The equivalent diameter distributions of the particles obtained from the TEM micrographs of samples with the highest concentration of ε-Fe_2O_3 polymorph, fitted by the log-normal distribution [52] (see equation 3.4), show a similar mean particle size d_0 for all investigated w_f in the range of 30-50 %, annealed at different temperatures in the interval of $1000-1125°C$ for 4 hours. However, their polydispersity index (pdi) increases slightly with increasing w_f, suggesting the means of narrowing the width of the size distribution.

Using the combination of XRPD (see figure 3.2), DC magnetic measurements (see figure 3.9), and Mössbauer spectroscopy (see figure 3.3), it was possible to provide a reliable estimate of the phase composition of ferric oxide nanoparticles in a sample for all detected phases of Fe_2O_3 (α, β, γ and ε), with a detection limit below 1 wt%. Although the results on phase composition, determined from XRPD and Mössbauer spectroscopy, agree very well, the advantages and limitations of the experimental methods should be mentioned. In some cases, a worse detection limit of XRPD is caused mainly by the overlap of the diffractions from the ε- phase and ultrafine nanoparticles of the γ-phase with broad diffraction lines, which arise

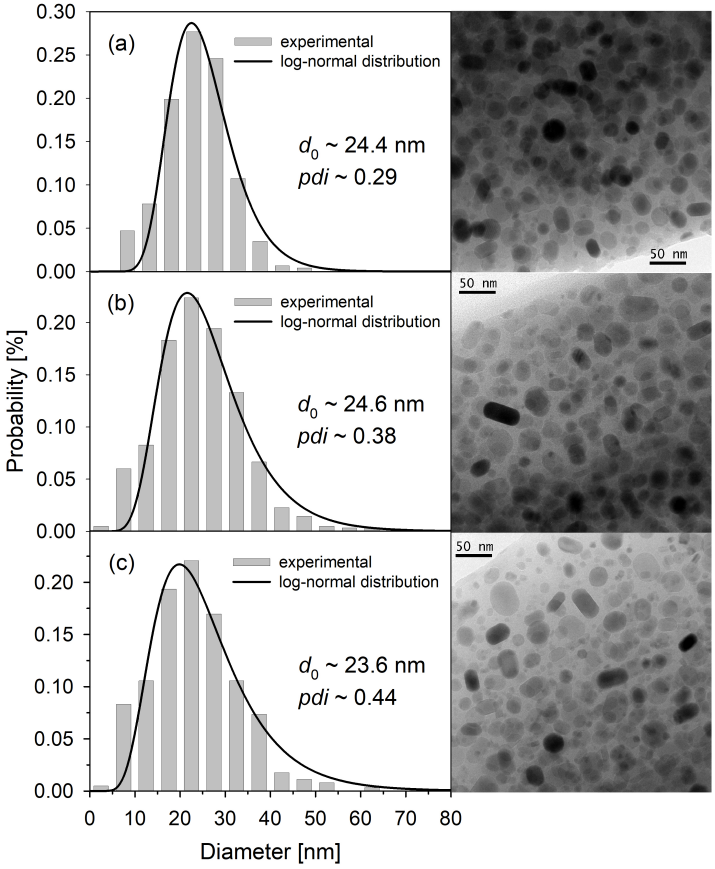

Figure 3.1: (Right) TEM micrographs of Fe_2O_3 nanoparticles dispersed in amorphous silica matrix - (a) 30%@1100°C, (b) 40%@1075°C, and (c) 50%@1025°C samples, (left) respective size distributions fitted under the assumption of the lognormal distribution profile. Adapted from [P6].

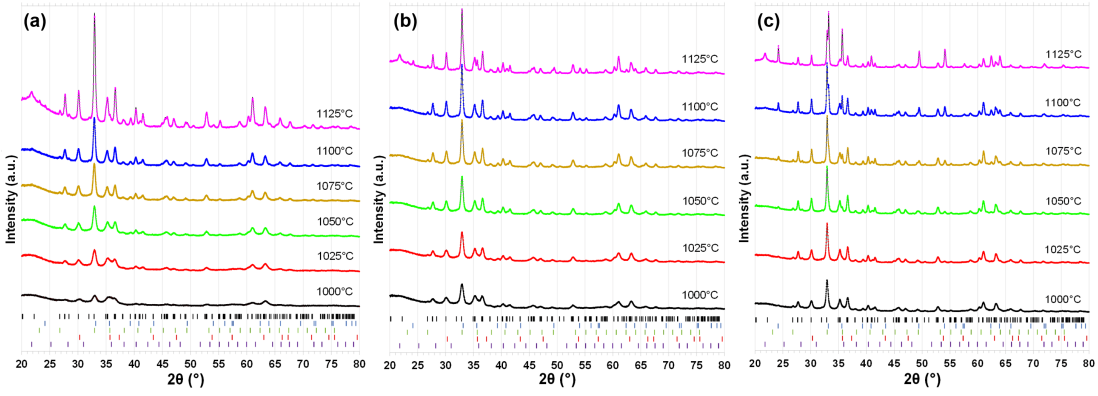

Figure 3.2: XRPD diffractograms of Fe_2O_3 nanoparticles of various ferric oxide mass fraction - (a) 30 %, (b) 40 %, and (c) 50 % - annealed at different temperatures. The reflections obtained by Rietveld analysis of the patterns are provided below the curves in this order from top to bottom - α-, β-, γ-, ε-phase of Fe_2O_3, and a-cristobalite (crystalline SiO_2 phase produced from the initially amorphous silica by annealing the sample). Adapted from [P6].

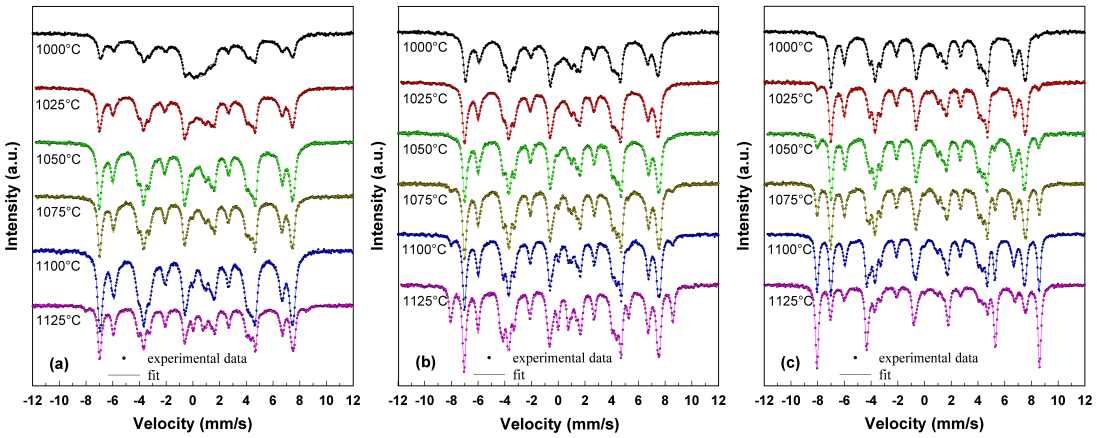

Figure 3.3: Mössbauer spectra of Fe_2O_3 nanoparticles of various ferric oxide mass fraction - (a) 30 %, (b) 40 %, and (c) 50 % - annealed at different temperatures. Decomposition of typical spectrum can be found in Section 2.4. Adapted from [P6].

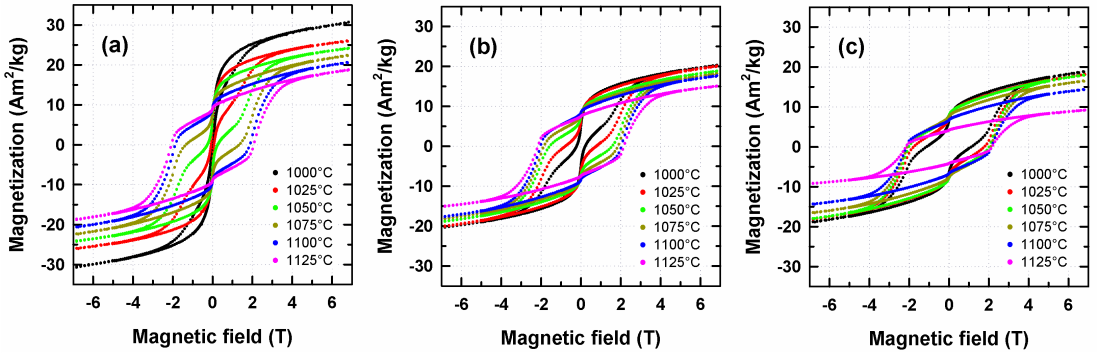

Figure 3.4: Hysteresis loops of Fe_2O_3 nanoparticles of various ferric oxide mass fraction - (a) 30 %, (b) 40 %, and (c) 50 % - annealed at different temperatures. Adapted from [P6].

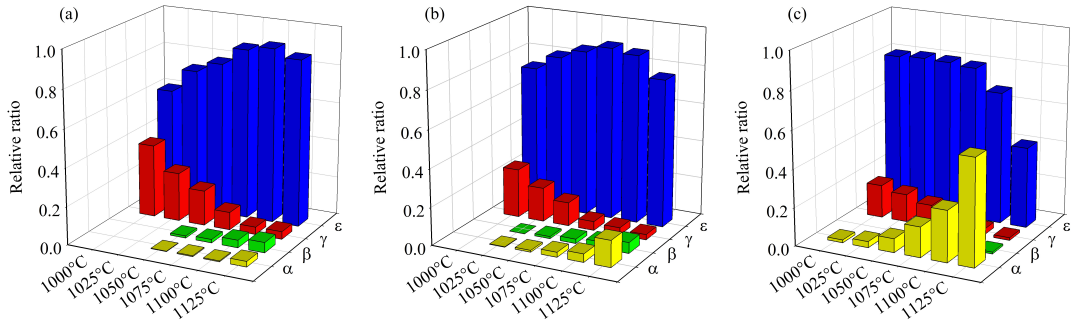

Figure 3.5: Phase composition of Fe_2O_3 nanoparticles dispersed in amorphous silica matrix as deduced from Mössbauer spectra - (a) 30 %, (b) 40 %, and (c) 50 % - annealed at different temperatures. Adapted from [P6].

especially for the samples prepared with lower Fe_2O_3 mass fraction and the lowest annealing temperatures (see figure 3.2). Compared to XRPD, only short-range order is necessary for a particular structure to contribute to the Mössbauer spectrum, thus allowing the disclosure of ultrafine nanoparticles with diameters of less than 5 nm as well (see also Section 3.4). Mössbauer spectroscopy is very well suited for the detection of the α phase, as the outermost lines of the relatively broad sextet with a large hyperfine magnetic field $B_{\mathrm{hf}} \sim 51.7$ T (see figures 3.16 and 3.3(c)) do not overlap with the signal from other ferric phases. In a similar manner, the β-phase manifests itself by a distinct doublet in the middle part of the spectrum. Even though the presence of γ-phase is also observable in XRPD patterns and Mössbauer spectra, it could be completely overlooked due to the significant broadening of its diffraction and spectral lines for ultrasmall particles, respectively, and an overlap with complex ε-Fe_2O_3 pattern/spectrum. Therefore, magnetic measurement is necessary to detect the possible presence of the γ-phase in the sample of ε-Fe_2O_3, which is characteristic by a large coercivity of 2.1 T and a saturated magnetization of ~ 17 Am^2/kg, see figure 3.4(left)). Due to a large saturated magnetization of ~ 80 Am^2/kg and almost zero coercivity (see figure 3.6(right)), γ-Fe_2O_3 manifests itself by the sharp change of magnetization observed in small fields in hysteresis loops (visually seen as the 'necking' of the loop) and an increase in the saturated magnetization (see figures 3.4(a) and 3.5(a)). In contrast, the presence of weakly ferromagnetic α-Fe_2O_3 (see also Section 3.4) leads to a decrease in the saturated magnetization (see figures 3.4(b,c) and 3.5(b,c)).

The optimal conditions for preparation of ε-Fe_2O_3-rich sample were established - the highest ε-Fe_2O_3 content of 91 % was achieved for the 30%@1100°C sample with a particle size of ~ 25 nm, together with the very low relative content of parasitic α-Fe_2O_3 in this sample, which is characteristic by low magnetization. It was observed that with an increase in the mass fraction of Fe_2O_3 in the initial mixture of precursors, the optimal annealing temperature decreases, while the width of the particle size distribution tends to increase. As is evident from the figure 3.5, the gradual transformation of maghemite into thermodynamically stable hematite with increasing annealing temperature, accompanied by the formation of intermediate phases [53], can be observed directly in the Mössbauer spectra.

3.2 Maghemite nanoparticles

To study the effect of surface (charge) modification on the performance of MPI tracers [P2], γ-Fe_2O_3 magnetic cores with an average diameter of 8.0 nm and 8.7 nm were synthetised by coprecipitation of ferrous and ferric salts with ammonium hydroxide, followed by oxidation with hydrogen peroxide and stabilization as a cationic (by addition of hydrochloric acid, designated as γ-$Fe_2O_3{}^{\oplus}$, ζ potential of +52 mV) or anionic (by addition of a trisodium citrate dihydrate solution prior to oxidation, designated as γ-$Fe_2O_3{}^{\ominus}$, ζ potential of -60 eV) colloid. For the coating of the prepared nanoparticles, polar derivatives of linear poly(HPMA-co-HAO) polymer were chosen because of its bioinert properties and ability to form a sterically stabilizing coating. The particles were characterized by TEM, XRPD, dynamic light scattering (DLS), inductively coupled plasma mass spectrometry

Table 3.1: Structural and magnetic characteristics of the maghemite nanoparticles. Parameter designations: d_X - mean particle size determined by TEM or mean hydrodynamic sized determined by DLS, pdi_X - respective polydispersity indices, M - magnetization.

Core	Coating	d_{TEM}	pdi_{TEM}	d_{DLS}	pdi_{DLS}	M @ 300 K, 3 T [Am^2/kg]
γ-$Fe_2O_3^{\oplus}$	none	8	1.3	96.9	0.153	79.9
γ-$Fe_2O_3^{\ominus}$	none	8.7	1.3	96	0.17	82.5
γ-$Fe_2O_3^{\oplus}$	poly(HPMA-co-HAO)	-	-	118	0.141	-
γ-$Fe_2O_3^{\ominus}$	poly(HPMA-co-HAO)	-	-	109.1	0.12	-

(ICP-MS), superconducting quantum interference device (SQUID) magnetometry, and Mössbauer spectroscopy.

For both uncoated and coated magnetic cores, the TEM micrographs showed a spherical shape of the particles with a narrow size distribution. XRPD analysis of uncoated samples indicated the single-phase nature and spinel structure of the prepared particles with the cubic space group of $Fd\bar{3}m$ and the lattice parameters a = 8.3508(4) Å, 8.3515(2) Å, and 8.3549(5) Å, pointing to a similar oxygen stoichiometry of both samples. The magnetization curves, shown in figure 3.6, confirmed superparamagnetic behavior at room temperature. The summary of determined parameters is provided in table 3.1.

Maghemite has a modified spinel structure described as $(Fe^{3+})[Fe^{3+}_{5/3}\square_{1/3}]O_4$, where ( ) denotes the tetrahedral A sites, [ ] stands for the octahedral B sites, and $\square$ represents the cation vacancies at the octahedral sites. The respective spectral components and their hyperfine parameters in the Mössbauer spectra, acquired at 4.2 K are shown in figure 3.7, could be resolved only by fixing the ratio of the iron in tetrahedral and octahedral sites determined by in-field measurement at 6 T. Their contributions to the spectra were modeled by two sextets with a distribution of the effective hyperfine magnetic field (see Section 4.1), well distinguished by their characteristic isomer shifts and nearly zero quadrupole shift. No other iron oxide polymorphs (see Section 3.1) were discerned within the

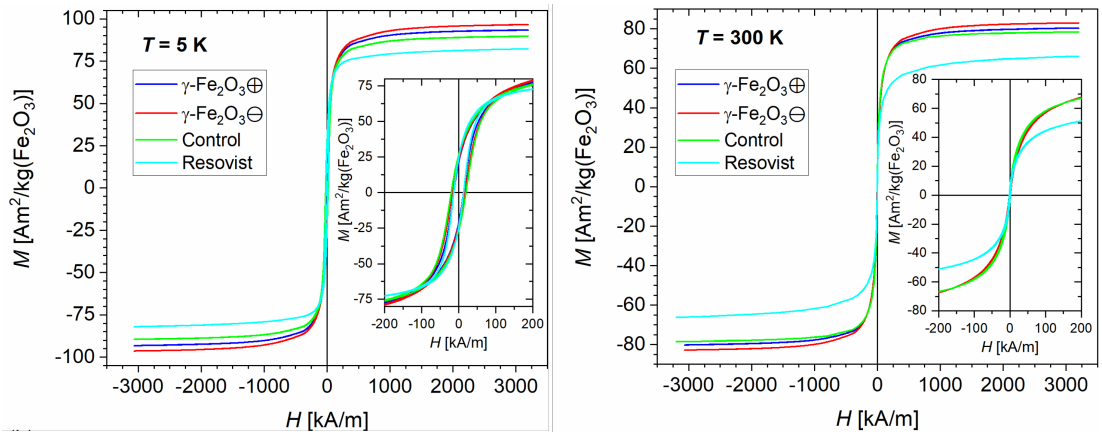

Figure 3.6: Hysteresis loops of the uncoated γ-Fe_2O_3 magnetic nanoparticles at 5 K (left) and 300 K (right), the insets show low-field details of the loops. Adapted from [P2].

accuracy of the measurement, which is 1–2 at%. The hyperfine parameters and other characteristics of the spectra are summarized in table 3.2.

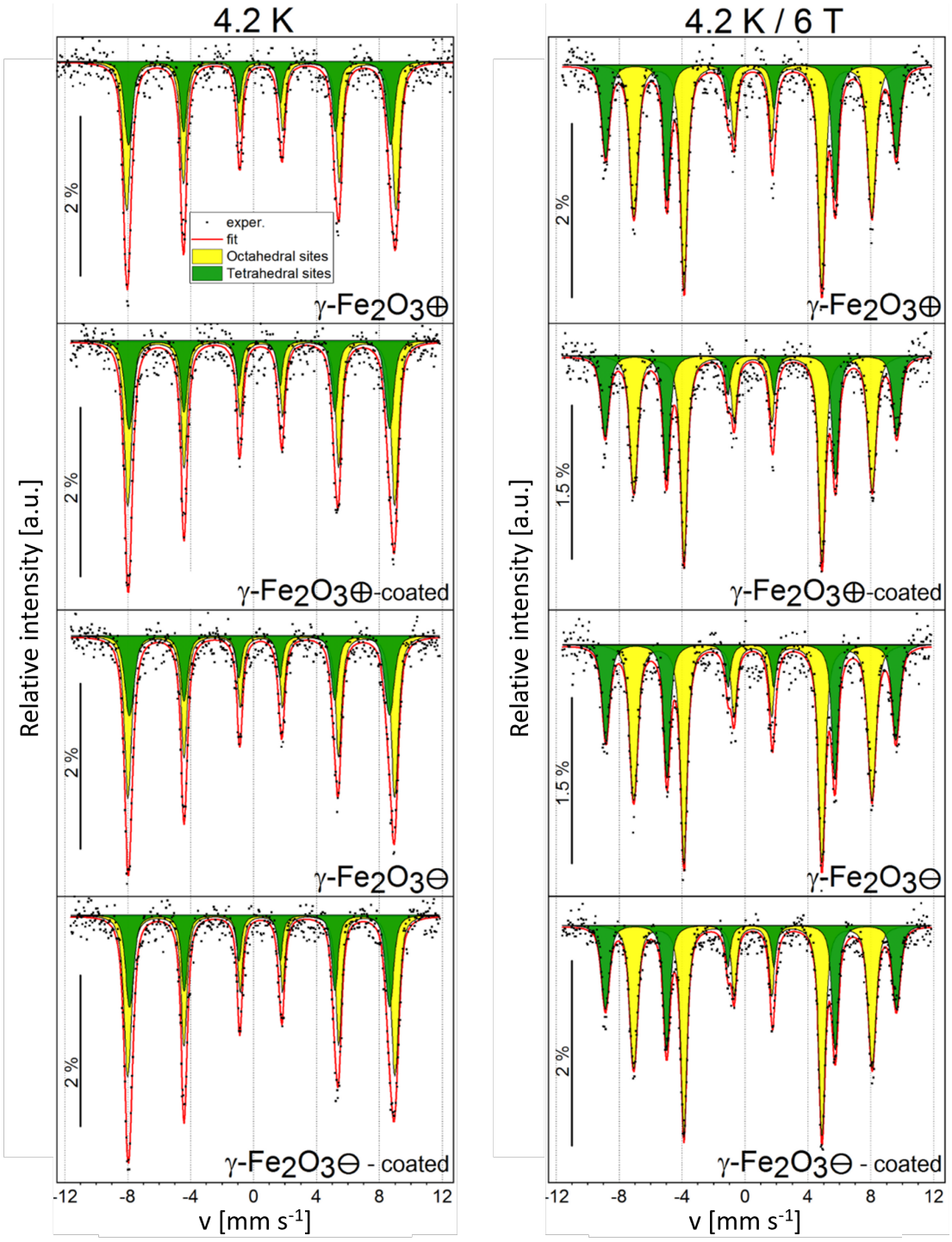

Figure 3.7: Mössbauer spectra of the γ-Fe_2O_3 nanoparticles acquired at liquid helium temperature (4.2 K) without (left) and in external magnetic field of 6 T (right). The green component represents Fe^{3+} in the tetrahedral sublattice and the yellow component Fe^{3+} in the octahedral sublattice. Adapted from [P2].

The acquired Mössbauer spectra can be interpreted in terms of the core-shell model described in Section 2.4. The parameter b that is related to the intensities of the second and fifth lines $I_{2,5}$ and the mean angle between the γ-beam and the

$\vec{B}_{\text{eff}}$ vector (see equation 2.8) can be used to calculate the magnetic shell proportion according to the relation given by $S = 3(4-b)/(b+4)$. The relative decrease of S of coated nanoparticles ($\sim$ 7 % for γ-$Fe_2O_3^{\oplus}$ and $\sim$ 11 % for γ-$Fe_2O_3^{\ominus}$) compared to their uncoated counterparts ($\sim$ 2 % and $\sim$ 7 %, respectively) suggests that the coating polymer affects the ordering of the magnetic moments in the surface layer of particles.

In addition to basic characterization, the particles were tested in vitro in a field-free point MPI scanner (signal-to-noise ratios (SNR) and signal displacement according to the protocol described in [54]) and their performance was compared to the commercially available Resovist® [55] (suspension of Fe_2O_3/Fe_3O_4 superparamagnetic nanoparticles by Bayer Healthcare, for structural and magnetic characteristics, see table 6.1). The cationic γ-$Fe_2O_3^{\oplus}$ (coated and uncoated) particles provided a signal insignificantly lower to that of Resovist®. The uncoated anionic γ-$Fe_2O_3^{\ominus}$ particles provided a slightly higher SNR, while the coated ones have a SNR identical to Resovist [P2].

Table 3.2: Spectral characteristics determined from the Mössbauer spectra of the maghemite samples acquired at liquid helium temperature (4.2 K). Individual components are designated by parentheses ( ) or [ ] to indicate the tetrahedral or octahedral sites, respectively. Parameter designations: B_{ext} - applied external magnetic field, IS - isomer shift, QS - quadrupole shift, B_{eff} - the effective hyperfine magnetic field on ^{57}Fe nuclei $B_{\text{eff}} = |\vec{B}_{\text{hf}} - \vec{B}_{\text{ext}}|$ (where $\vec{B}_{\text{hf}}$ is the hyperfine magnetic field), b - ratio of line intensities $I_{2,5}/I_{3,4}$, A - area fraction of the given component.

Sample	B_{ext} [T]	Component	IS [mm/s]	QS [mm/s]	B_{hf} [T]	B_{eff} [T]	b	A [%]
γ-$Fe_2O_3^{\oplus}$	0	(Fe^{3+})	0.39(3)	-0.07(5)	51.8(3)	-	2.05(5)	37.5*
		[Fe^{3+}]	0.50*	0.03(4)	53.1(3)	-	2.05(5)	62.5*
	6	(Fe^{3+})	0.38(3)	-0.02(2)	51.4(3)†	57.4(3)	3.82(8)	37.7(7)
		[Fe^{3+}]	0.50(2)	0.01(2)	53.0(3)†	47.0(3)	3.82(8)	62.3(7)
γ-$Fe_2O_3^{\ominus}$	0	(Fe^{3+})	0.38(3)	-0.01(3)	51.3(3)	-	2.00(3)	37.5*
		[Fe^{3+}]	0.50*	0.00(4)	52.7(3)	-	2.00(3)	62.5*
	6	(Fe^{3+})	0.37(3)	-0.01(2)	51.3(3)†	57.3(3)	3.71(8)	36.2(7)
		[Fe^{3+}]	0.50(2)	0.01(2)	53.0(3)†	47.0(3)	3.71(8)	63.8(7)
γ-$Fe_2O_3^{\oplus}$ coated	0	(Fe^{3+})	0.37(3)	-0.02(4)	51.4(3)	-	2.04(5)	37.5*
		[Fe^{3+}]	0.50*	0.00(3)	52.7(3)	-	2.04(5)	62.5*
	6	(Fe^{3+})	0.38(3)	-0.01(3)	51.6(3)†	57.6(3)	3.95(9)	34.9(7)
		[Fe^{3+}]	0.51(2)	0.01(3)	53.1(3)†	47.1(3)	3.95(9)	65.1(7)
γ-$Fe_2O_3^{\ominus}$ coated	0	(Fe^{3+})	0.39(3)	-0.04(4)	51.3(3)	-	2.04(4)	37.5*
		[Fe^{3+}]	0.50*	0.02(3)	52.7(3)	-	2.04(4)	62.5*
	6	(Fe^{3+})	0.38(2)	0.01(3)	51.4(2)†	57.4(2)	3.81(4)	36.3(4)
		[Fe^{3+}]	0.50(2)	0.00(3)	53.1(2)†	47.1(2)	3.81(4)	63.7(4)

* denotes fixed parameter
† B_{hf} = (B_{eff} - B_{ext}) assuming that the magnetic moments of Fe^{3+} are oriented in the direction of the external magnetic field

3.3 ε-phase nanoparticles

Spatial restriction during particle growth is a decisive factor for the successful formation of ε-Fe_2O_3 nanoparticles. Based on the identification of the polymorphs of iron oxide nanoparticles, formed in the pores of the amorphous silica matrix, the synthesis conditions were optimized to maximize the yield of the ε-phase in the sample. As a result, high purity ε-Fe_2O_3 nanoparticles were prepared in a mesoporous amorphous silica matrix with defined 5-nanometer pores that was impregnated with an aqueous solution of ^{57}Fe-enriched precursors and subsequently annealed at 1050 °C [P9]. The matrix in the final product was leached off by NaOH to release the particles that were characterized by TEM (characteristic micrograph shown in figure 3.8(right)), XRPD and studied in detail by Mössbauer spectroscopy.

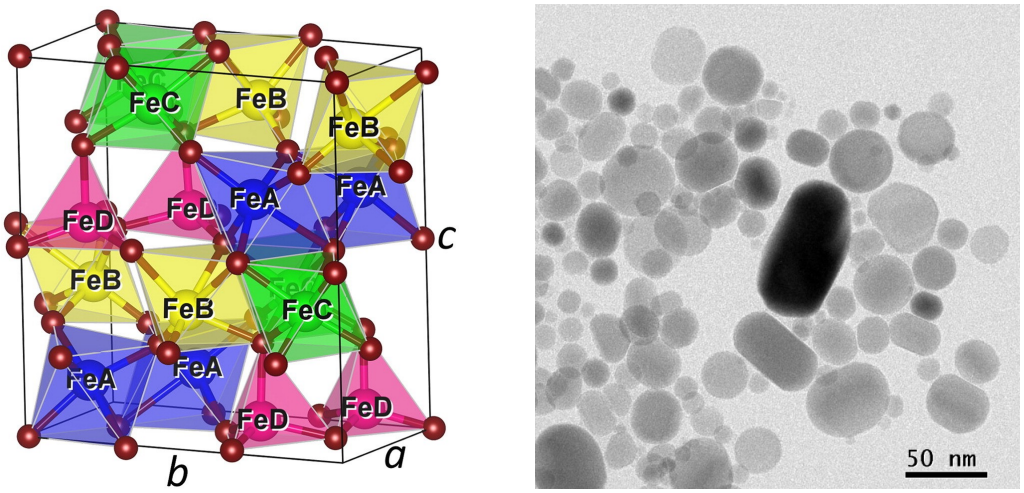

Figure 3.8: (Left) ε-Fe_2O_3 unit cell consisting of three octahedrally coordinated non-equivalent iron sites (FeA, FeB, FeC) and one tetrahedrally coordinated iron site (FeD) [56]. Reproduced with permissions from Elsevier B.V. (Right) bright-field TEM micrograph of ^{57}Fe-enriched ε-Fe_2O_3 nanoparticles collected after silica matrix dissolution.

The crystal structure of ε-Fe_2O_3 is orthorhombic noncentrosymmetric with the space group of $Pna2_1$ (see figure 3.8(left)) and the lattice parameters at room temperature are a = 5.1019(3) Å, b = 8.7807(6) Å, c = 9.4661(5) Å [57], and the unit cell comprises eight formula units. Iron cations occupy three different octahedral sites (FeA, FeB, FeC) and one tetrahedral site (FeD) with various degrees of distortion [58]. Below the Curie (Néel) temperature T_C, ∼ 500 K, ε-Fe_2O_3 is a collinear ferrimagnet with the four sublattice magnetizations parallel to a-axis, and large magnetocrystalline anisotropy [59]. Upon further decrease in the temperature, multiple magnetic transitions occur. At room temperature, a rather large coercive field of ∼ 2.1 T is observed for randomly oriented particles (see figure 3.9(left)). The magnetization does not reach saturation even at fields as high as 14 T, which may be a result of noncollinear magnetic ordering in the surface layers of the particles.

ε-Fe_2O_3 nanoparticles undergo a structural and magnetic transition in the ∼ 80-150 K temperature range [58] (see figure 3.9(left)). In a previous study [P10], the temperature and external magnetic field dependence of Mössbauer spectra

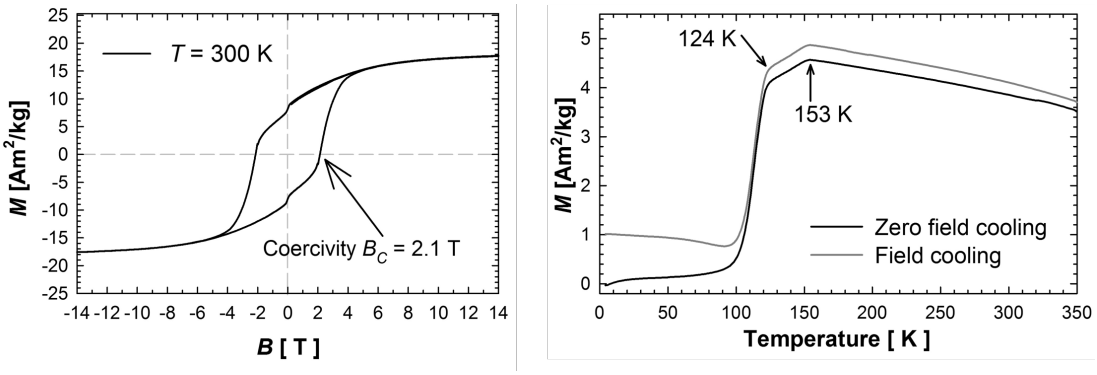

Figure 3.9: (Left) field dependence at 300 K and (right) temperature dependence of the zero-field-cooled and field-cooled magnetization at 10 mT of the powdered Fe_2O_3 nanoparticles, embedded in silica matrix. Data has been corrected for the diamagnetic contribution of the silica matrix. Adapted from [P10].

of ^{57}Fe-enriched sample with 85(2) % purity (according to MS) suggested that the first step in the temperature range of 153 – 130 K is related to the spin reorientation of the local magnetic moments in the magnetic sublattices and the second step in temperature interval of 130 – 100 K may be associated with the intermediate spin - high spin state transition of Fe^{3+} cations in the tetrahedral sublattice expressed in the change of the hyperfine magnetic field [P10].

The Mössbauer spectra of the high-purity sample, acquired in a broad temperature range of 4.2 - 540 K, were fitted assuming the core-shell model (see Sections 2.4 and 3.1). In addition to the spectral intensity ascribed to the ε-phase, the outermost minor sextet in the Mössbauer spectra with an intensity below 2 % was attributed to the impurity, most probably of α-Fe_2O_3 nature (hematite, see section 3.4). Typical spectra, observed below and above the Curie temperature T_C, are shown in figure 3.10 and the temperature dependencies of the hyperfine parameters are summarized in figure 3.11. In contradiction to [60], the magnetic order is lost at $T_C \sim 505$ K where only doublets, corresponding to four positions of the ε-Fe_2O_3 crystal structure, are observed in the spectrum, and no other high-temperature ε-phase is observed.

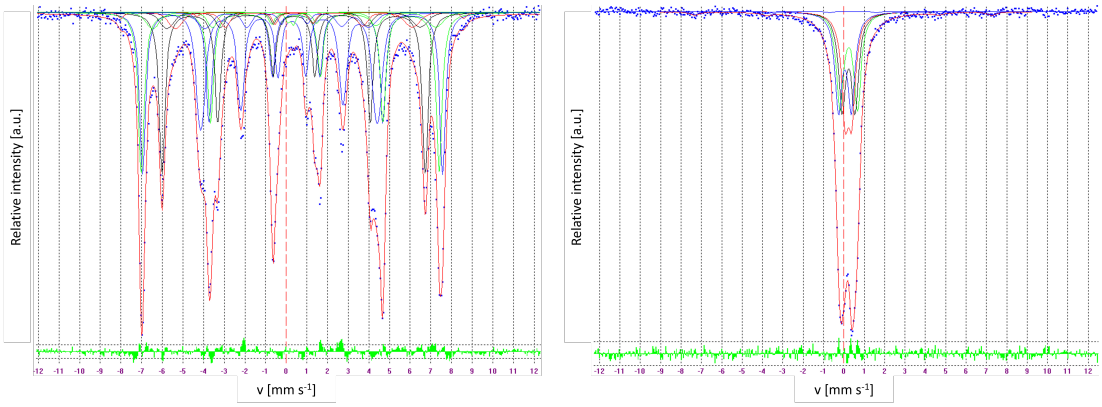

Figure 3.10: Decomposition of the Mössbauer spectra of the ε-Fe_2O_3 nanoparticles acquired at 300 K (left) and 510 K (right) assuming core-shell model.

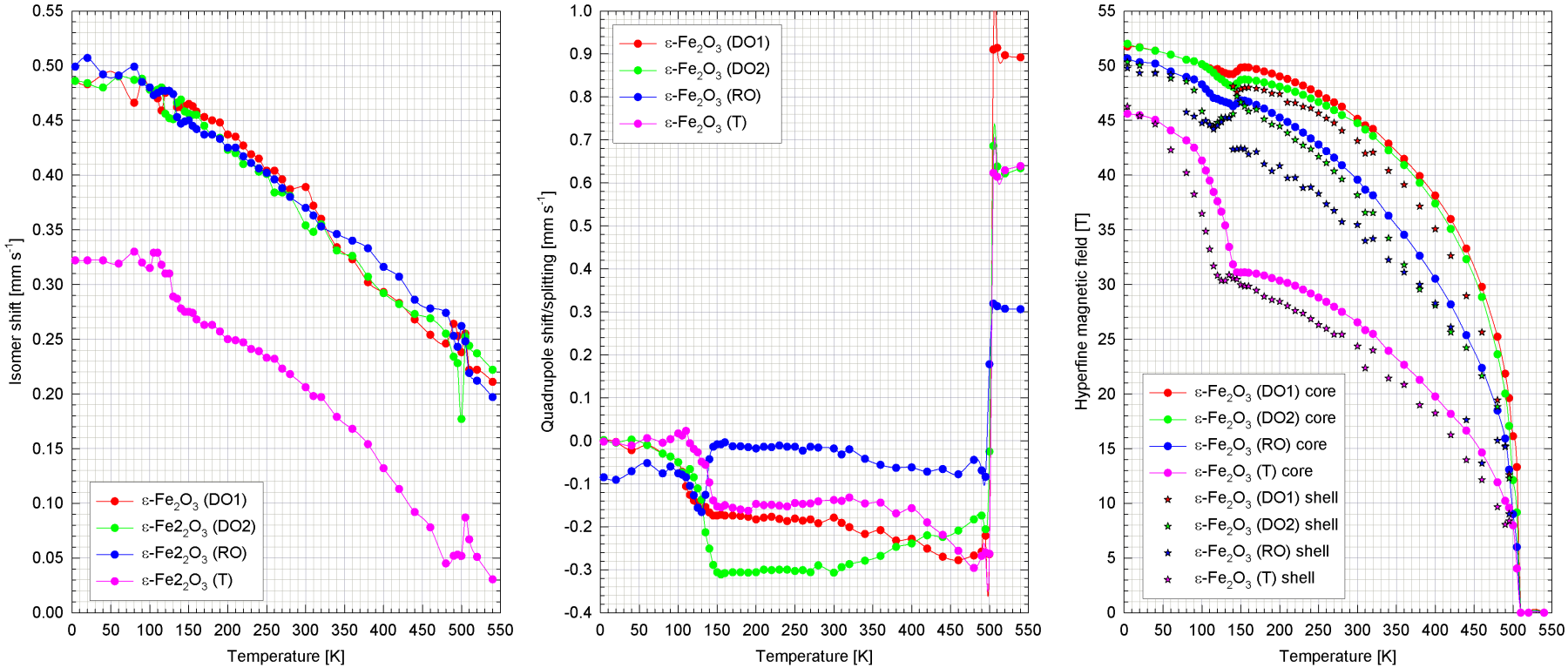

Figure 3.11: Temperature dependence of the hyperfine parameters - (left) isomer shift *IS*, (center) quadrupole shift/splitting *QS*, and (right) hyperfine magnetic field B_{hf} for both core and shell components. The iron site designations in the legends match with the unit cell shown in figure 3.8(left), by the key: FeA - DO1, FeB - DO2, FeC - RO, FeD - T.

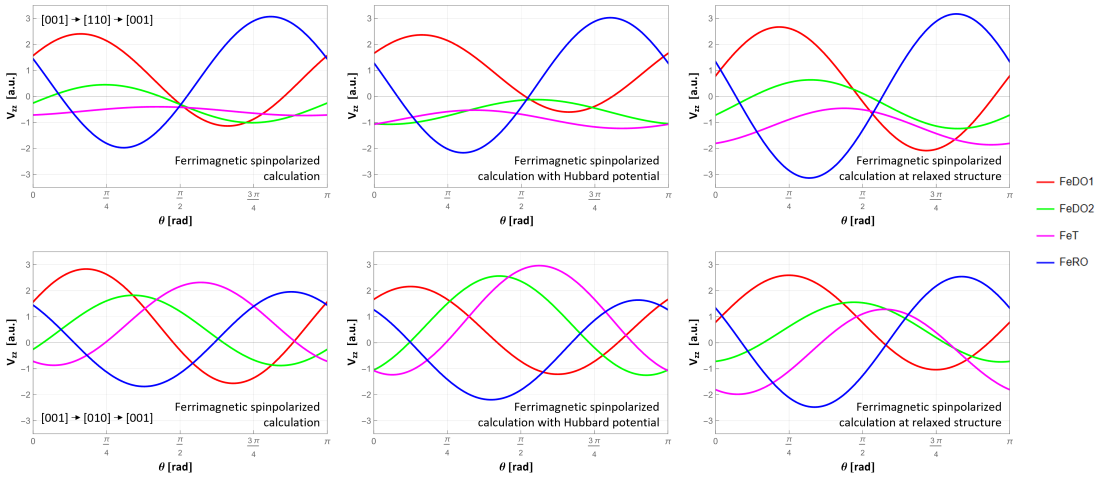

Figure 3.12: Dependence of the magnitude of V_{B} on the direction of the $\vec{B}_{\mathrm{hf}}$ vector during magnetic moment rotation from the [001] crystallographic direction through [110] to [001] (top row) and [001] through [010] to [001] (bottom row), based on DFT calculations of the EFG tensor under various conditions. The coloring of the V_{B} angular dependencies match the iron sites as presented in figure 3.11.

With decreasing temperature, the quadrupole shifts (shown in figure 3.11) approach zero below the spin-reorientation transition, except for the FeC site. To determine the respective rotation of the magnetic moments within the unit cell, EFG tensors (see Section 2.1) were calculated using DFT [61], starting from ε-Fe_2O_3 structural parameters determined at 200 K according to [58]. Spin polarized electronic calculation was performed with the LAPW method, implemented in the WIEN2k code using PBE-GGA functional, assuming ferrimagnetic ordering of the iron magnetic moments. Another calculations were performed also considering the Hubbard U potential of 4.55 eV applied for Fe 3d states, and after the initial structure was relaxed using VASP code package. Based on these EFG tensors, the angular dependencies of their projection V_{B} to the direction of the $\vec{B}_{\mathrm{hf}}$ vector during magnetic moment rotations in ε-Fe_2O_3 crystal lattice were calculated (i.e., normalized quadrupole shift QS). Some specific cases of [001] → [110] → [001] and [001] → [010] → [001] rotation are shown in figure 3.12. The V_{B} magnitudes tend to approach zero if the $\vec{B}_{\mathrm{hf}}$ vector points in between the a and b axes, suggesting that the magnetic moments originally lying along the a axis at higher temperatures, rotate to this direction upon cooling.

In a specific geometric configuration of in-field Mössbauer spectroscopy, when an external magnetic field is applied in parallel direction with the incident γ-beam and the magnetic moments in the sample are collinearly aligned with this orientation, the second and fifth lines of a spectrum are supposed to diminish completely (line intensities I_2,$I_5 \to 0$, see equation 2.8) [13]. However, the in-field Mössbauer spectra acquired at 260 K show nonzero intensities of these lines even at an external magnetic field as high as 7 T, as can be seen from figure 3.13, which is in accordance with the core-shell model described in Section 2.4. Given by the equation 2.8, the ratio of spectral line intensities $b = 0.64$. The presented preliminary results together with other complementary analyses are to be published.

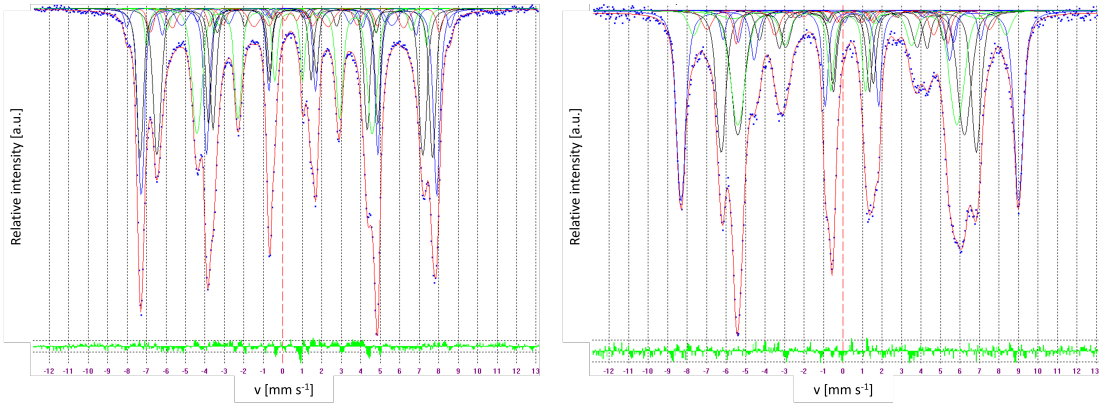

Figure 3.13: Mössbauer spectra of the ε-Fe_2O_3 nanoparticles, acquired at a temperature of 260 K without (left) and in (right) an external magnetic field of 7 T.

Another system of nanoparticles, based on the substituted 21-nanometer ε-Fe_2O_3, coated by citrate or silica layer of various thicknesses, was investigated as a potential MRI contrast agent. The aluminum cation preferentially occupies tetrahedral sites and leads to an increased magnetization. Moreover, it suppresses the spin-reorientation transition. The ε-$Al_{0.23}Fe_{1.77}O_3$ nanoparticles show a low toxicity and their performance in ultra-high-field MRI at 11.75 T is comparable to that of Resovist® [P5].

3.4 Hematite nanoparticles

Nanoparticle characterization

Samples of pure α-Fe_2O_3 phase, differing in the mean size of the nanoparticles, were prepared by two distinct chemical techniques - relatively smaller magnetic cores by the hydrothermal method (samples of nanoparticles with mean size below 100 nm), and larger by the sol-gel approach (sample of nanoparticles with mean size above 100 nm), starting from ^{57}Fe-enriched precursors. The nanoparticles were studied by means of TEM, XRPD, SQUID magnetometry and Mössbauer spectroscopy, all described in detail in [P7].

Analysis of TEM micrographs shown in figure 3.14, obtained on a JEOL JEM 3010 microscope with 300 kV accelerating voltage and samples deposited on a polymer film supported by a perforated copper disk, suggests a lognormal distribution of particle sizes, which is typical for nanoparticles prepared by chemical routes. The preparation by the hydrothermal technique led to small spherical nanoparticles (SM5.6), mixed spherical/rhombus ones (RH26) and spindle-shaped ones (SP42). A bimodal distribution of RH26 may indicate the presence of two parallel mechanisms of nanoparticle formation that take place during hydrothermal preparation. The sol-gel approach resulted in nanocomposite containing homogeneously dispersed globular to rod-like shaped particles embedded in amorphous SiO_2 matrix. Due to the inhomogeneity of local conditions in the reaction mixture and taking into account the energetically favorable structural phase for the given diameter, relatively smaller, disk-like-shaped particles of ε-Fe_2O_3 can be generally observed as a minor intermediate phase together with termodynamically stable α-Fe_2O_3 [P6], as suggested by both magnetic properties measurements

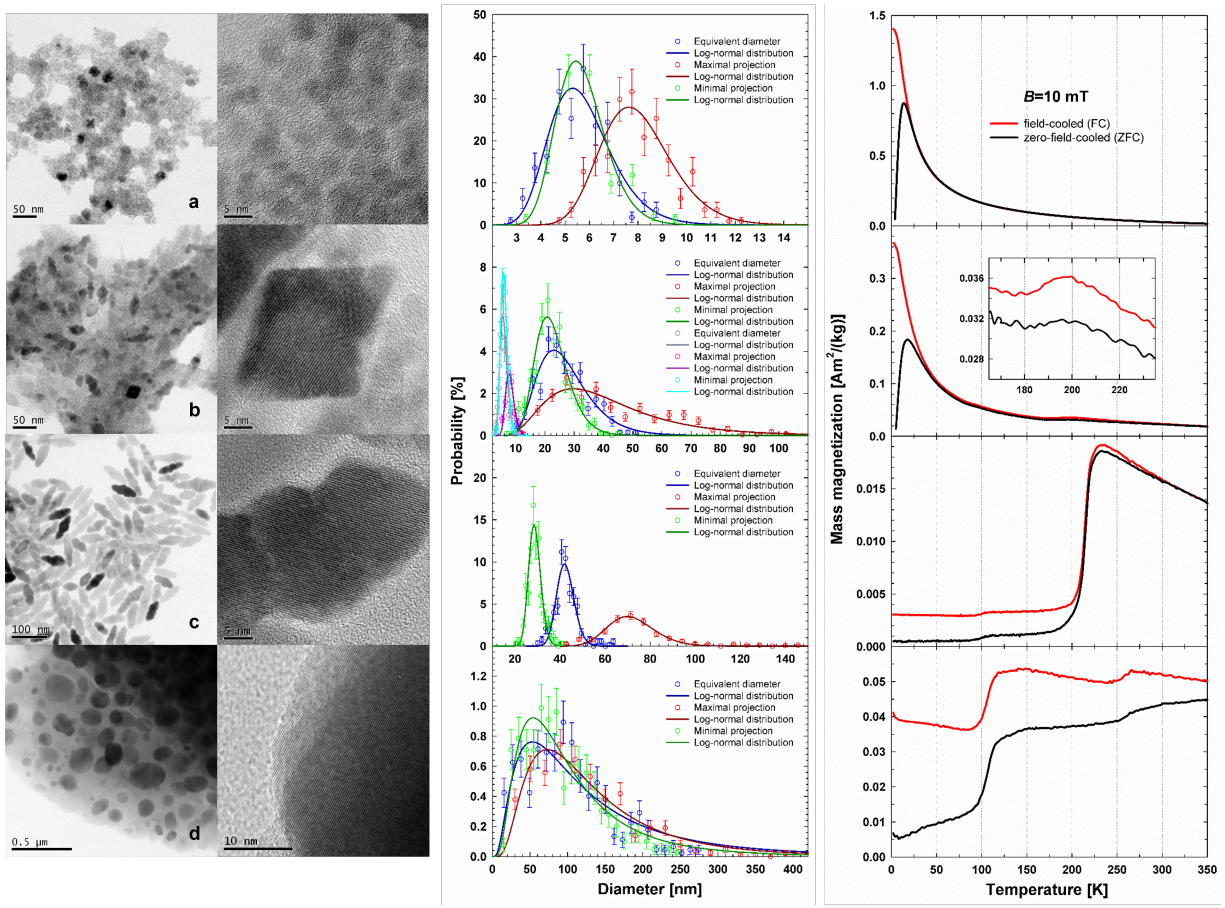

Figure 3.14: (Left) TEM and high resolution TEM micrographs of the hematite nanoparticles presented in the order of increasing mean diameter (a - SM5.6, b - RH26, c - SP42, d - RS103), (center) respective size distributions of equivalent diameters, minimal and maximal projections determined from TEM micrographs, fitted under the assumption of the lognormal distribution profile, (right) respective ZFC and FC magnetizations measured in an external magnetic field of 10 mT. Adapted from [P7].

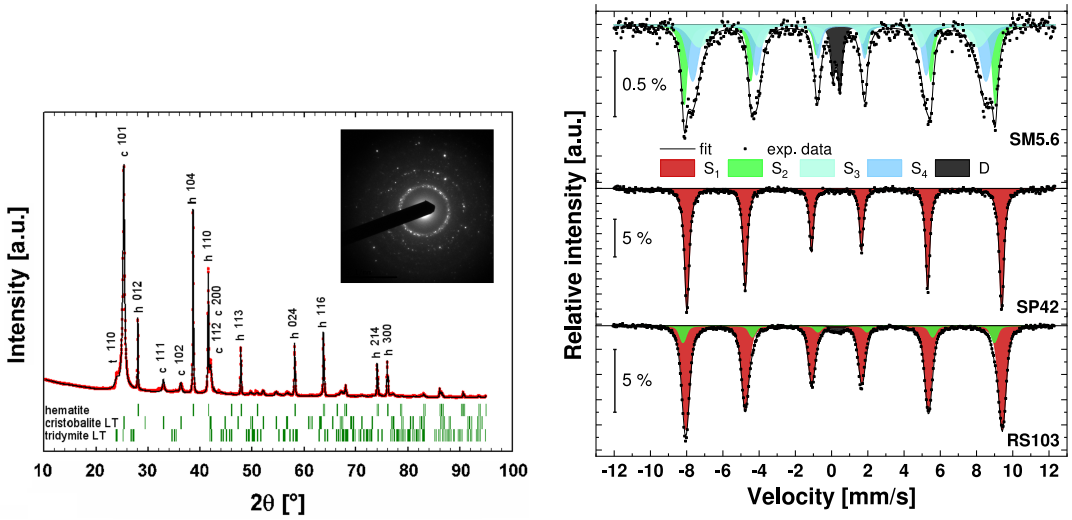

Figure 3.15: (Left) XRPD patterns of the RS103 sample with indicated reflections obtained by the Rietveld analysis, (right) Mössbauer spectra of the hematite nanoparticles acquired at liquid helium temperature (4.2 K); assignment of the spectral components provided in table 3.3.

as well as Mössbauer spectroscopy. In all samples, XRPD confirmed hematite as the major phase of a hexagonal crystal structure with the space group of $R\text{-}3c$ (corundum) with a possible concentration of other polymorphs of iron oxide below or comparable to the detection limit of the XRPD measurements ($\sim$ 2 wt%). The lattice parameters a = 5.038(2) Å and c = 13.772(12) Å were obtained by Rietveld refinement of the diffraction patterns of the RS103 sample shown in figure 3.15(left).

At room temperature, the Mössbauer spectra of nanoparticles with a mean diameter below 100 nm are strongly influenced by superparamagnetic relaxation (see Supplementary information of [P7]). In a similar manner, the SPM features can also be observed in the temperature dependence of magnetization (see figure 3.14(right)), even though the time windows of the methods are different (about 8 orders of magnitude higher than MS). The Mössbauer spectra acquired at 4.2 K, provided in figure 3.15(right), features magnetically-ordered components specific

Table 3.3: Spectral characteristics determined from the Mössbauer spectra of the hematite samples acquired at 4.2 K. Parameter designations: IS - isomer shift, QS - quadrupole shift, B_{hf} - hyperfine magnetic field, A - area fraction of the given component.

Sample	Component	Assignment	IS [mm/s]	QS [mm/s]	B_{hf} [T]	A [%]
SM5.6	S_2	WF of α-Fe_2O_3	0.48(2)	-0.06(3)	53.3(3)	36
	S_3	A-site of γ-Fe_2O_3	0.44(4)	-0.08(6)	47.8(6)	24
	S_4	B-site of γ-Fe_2O_3	0.49(3)	-0.11(4)	50.3(4)	40
SP42	S_1	AF of α-Fe_2O_3	0.49(2)	0.43(2)	54.0(2)	100
RS103	S_1	AF of α-Fe_2O_3	0.49(2)	0.42(2)	54.3(2)	92
	S_2	WF of α-Fe_2O_3	0.49(2)	-0.16(4)	53.4(3)	8

to the sample and a doublet D originating from the experimental setup. The S1 and S2 sextets were ascribed to iron cations with antiferromagnetic (AF), observed below the Morin temperature T_{M}, and weakly ferromagnetic (WF) spin ordering, observed above T_{M}, respectively, or in case of suppression of the Morin transition in a fraction of small nanoparticles. In addition to these, the spectrum of the sample SM5.6 revealed γ-Fe_2O_3 impurity modeled by two sextets S3 and S4 with a 3:5 intensity ratio.

In the first-order approximation, the magnitude of the quadrupole shift depends on the polar θ and azimuthal φ angles between the EFG tensor principal axis and the direction of the hyperfine magnetic field [13], i.e.,

$$QS = \frac{eQV_{\mathrm{zz}}}{4}(3\cos^2\theta - 1 + \eta\sin^2\theta\cos 2\varphi), \tag{3.1}$$

where e is the electron charge, Q is the quadrupole moment of ^{57}Fe nuclei in the excited state with spin $I = 3/2$, V_{zz} is the main component of EFG tensor and η is the asymmetry parameter. In case of AF spin arrangement, observed at low temperatures, the direction of the magnetic moments lies in parallel with the crystallographic c-axis since the electronic magnetic moments of Fe^{3+} ions are antiparallel to the hyperfine magnetic field on ^{57}Fe nuclei. Assuming that the symmetry axis of the EFG tensor is parallel to the crystallographic c-axis, which is perpendicular to the basal plane of the hexagonal structure, the asymmetry parameter is zero, and after redefinition $\theta = \pi/2 - \alpha$, relation 3.1 simplifies to

$$\alpha = \sin^{-1}\left(\pm\sqrt{\frac{QS/C + 1}{3}}\right). \tag{3.2}$$

Here α is the angle between the basal plane and the magnetic moment of the WF phase, which is observed for small nanoparticles even at helium temperature in case the Morin transition is suppressed. The sextets S1 (shown red in the figure 3.16), with quadrupole shift $QS \sim 0.42$ mm/s and hyperfine field B_{hf} approaching to ~ 54.3 T with decreasing temperature, correspond to the AF ordering under T_{M} and their hyperfine parameters lead to $C = 0.21$ mm/s in relation 3.2. If we assumed that the EFG components do not change with decreasing dimension of the nanoparticles, the mean deviation angles α for the WF arrangement of magnetic moments of RS103 and SM5.6 samples are $\sim 16\,^\circ$ and $\sim 29\,^\circ$, respectively, pointing to an anticipated influence of particle dimensions (i.e., surface-to-volume ratio) on spin canting within the nanoparticles [62].

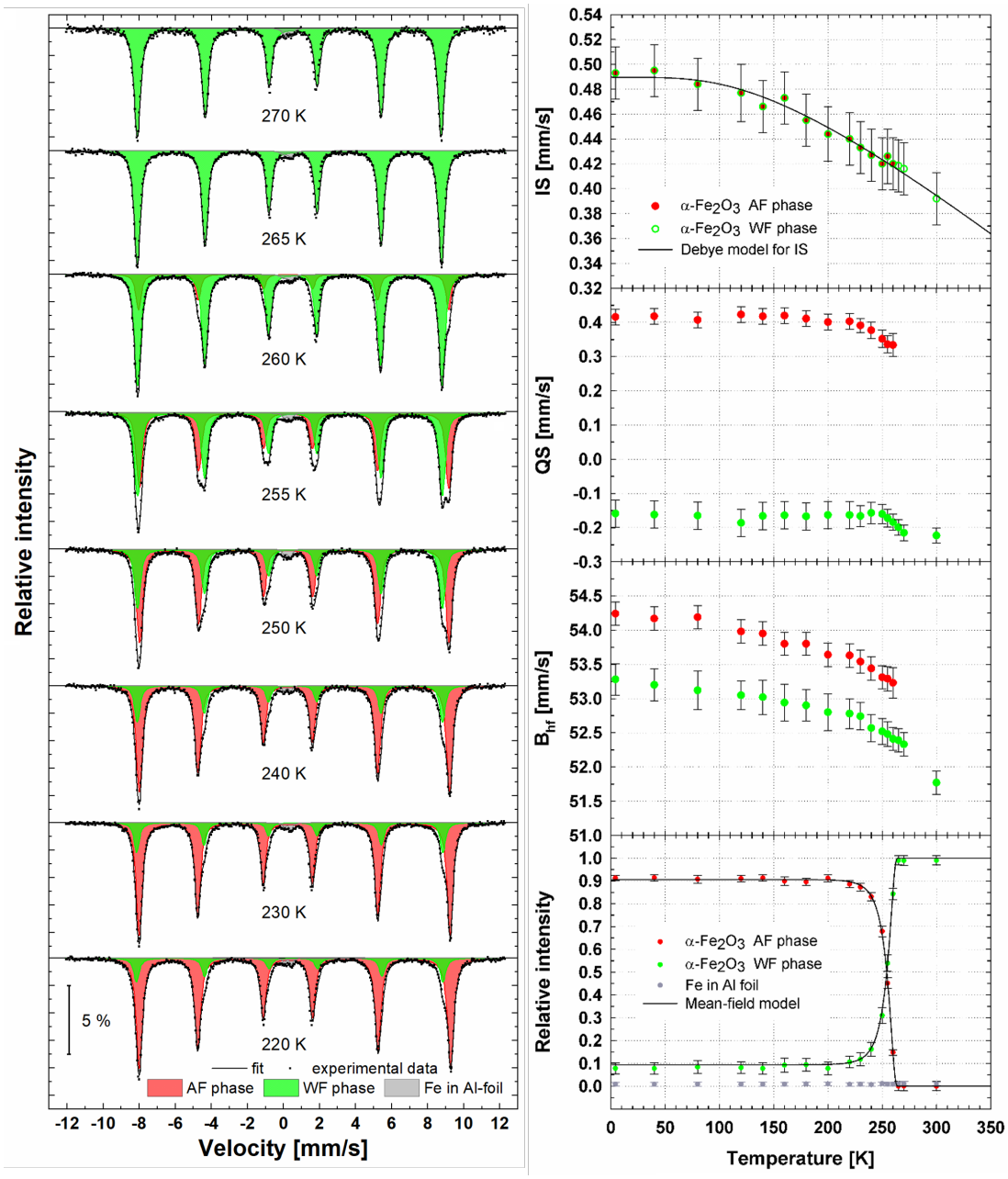

Figure 3.16: (Left) temperature dependence of Mössbauer spectra of RS103 sample around the Morin transition, (right) temperature dependence of hyperfine parameters - isomer shift *IS*, fitted by the Debye model (see equation 2.5 with *IS* = 0.54(1) mm/s, and $\theta_{\mathrm{D}} = 610(20)$ K), quadrupole shift *QS*, hyperfine magnetic field B_{hf}, and relative intensities of the AF and WF phases fitted by equation 3.5. Adapted from [P7].

Theoretical model of the Morin transition for particles with size and shape distribution

In bulk hematite, a spin reorientation transition from AF to WF spin ordering occurs upon heating at the so-called Morin temperature T_{M}, which was observed to change with magnetic field, pressure, particle size, and lattice strain originating in crystal defects [63]. A distribution of these parameters in the systems of real nanoparticles manifests itself in the distribution of Morin temperatures, broadening the transition as observed by various physical methods. In general, T_{M} decreases with decreasing particle volume of particles with a bulk limit of $\sim$ 264 K. For particles smaller than approximately $\sim$ 20 nm, the Morin transition may even be suppressed and disappears entirely due to the strong deviation of near-surface spins from the AF easy axis (i.e., surface effects) [64].

By means of Mössbauer spectra acquired between 4.2 and 300 K, we determined the relative ratio of the coexisting AF and WF phases in the transition region for the ^{57}Fe-enriched RS103 sample from the temperature dependence of the intensities of the respective sextets, assuming the same f-factor for both magnetic phases, and searched for the best finite-scaling theoretical model to describe the data presented in figure 3.16(right). The size dependence of the Morin temperature of unimodal particles of diameter d can be written as [65–67]

$$\frac{T_{\mathrm{M}}(\infty) - T_{\mathrm{M}}(d)}{T_{\mathrm{M}}(\infty)} = \left(\frac{\xi_\infty}{d}\right)^{\lambda}. \tag{3.3}$$

Here, the scaling factor λ results from the idealized spin system model - 1 for the mean-field theory model, 1.4 for the Heisenberg 3D model, and 1.6 for the Ising spin system, $T_{\mathrm{M}}(\infty)$ is the Morin temperature of the bulk material, and ξ_∞ is the correlation length in the bulk material at temperature T away from the ordering temperature. We proposed the introduction of a lognormal distribution of particle size [52], supported by the experiment, into the model. Putting

$$f(d) = \frac{1}{\sqrt{2\pi}\sigma d} \exp\left(-\frac{\ln^2(d/d_0)}{2\sigma^2}\right), \tag{3.4}$$

where $d_0.\exp(\sigma^2/2)$ is the mean particle diameter, ${d_0}^2(\exp(2\sigma^2) - \exp(\sigma^2))$ the variance and pdi=$(\exp(\sigma^2)$-$1)^{1/2}$ is the polydispersity index, into the equation 3.3 leads (after some exhausting derivation) to the integral formula for the normalized probability/relative frequency of the cumulative volume of particles that were already subject to the Morin transition at any given temperature

$$P(T,\,\text{parameters}) = \begin{cases} C\,\dfrac{\int_{\Delta}^{\infty}\left(1-\left(\frac{\xi_\infty}{\delta}\right)^{\lambda}\right) f(\delta)\,\theta(\delta-\xi_\infty)\,\mathrm{d}\delta}{\int_{0}^{\infty}\left(1-\left(\frac{\xi_\infty}{\delta}\right)^{\lambda}\right) f(\delta)\,\mathrm{d}\delta} & \text{for } T < T_{\mathrm{M}}(\infty), \\ 0 & \text{for } T \geq T_{\mathrm{M}}(\infty), \end{cases} \tag{3.5}$$

with a lower boundary of the integral over diameters δ in the numerator given as

$$\Delta\Big(T_{\mathrm{M}}(\infty),\lambda,T\Big)=\xi_{\infty}\left(\sqrt[\lambda]{1-\frac{T}{T_{\mathrm{M}}(\infty)}}\right)^{-1}, \tag{3.6}$$

where θ is Heaviside jump function.

To clarify the dependence of the Morin temperature on particle size, we synthesized hematite nanoparticles of various mean diameters and overall shapes of crystallites (see micrographs in figure 3.14). To accelerate the experiment, a sample enriched in ^{57}Fe with a broad particle size distribution was chosen for a detailed Mössbauer analysis in the whole temperature range. The models described above were calibrated using these data employing a script that is presented in the Attachments. The comparison of the relevant parameters derived from the fit of the experimental data by the theoretical models is provided in table 3.4, and the curves evolving with varying diameter are shown in figure 3.18. Both the Heisenberg 3D model and the Ising model are compatible with the experimental values of the Morin temperature of bulk material, i.e., $T_{\mathrm{M}}(\infty)$ = 265 (1) K, and the correlation lengths ξ_{∞} = 8.1(2) nm and 9.4(2) nm, respectively.

Table 3.4: Comparison of the fitted parameters of the finite-scaling theoretical models describing the temperature dependence of the relative intensity of AF and WF ordered phase in the ^{57}Fe-enriched RS103 sample and experimentally obtained values.

Parameter	Mean-field theory	Heisenberg 3D model	Ising model	Experiment
λ	1*	1.4*	1.6*	1 [68]
$T_{\mathrm{M}}(\infty)$ [K]	265(1)	265(1)	265(1)	264(2) [68]
ξ_{∞} [nm]	4.1(2)	8.1(2)	9.4(2)	8.3(5) [68]
d_0 [nm]	107(9)	83(9)	72(9)	103 (TEM)
σ	0.7(1)	0.5(1)	0.4(1)	0.8 (TEM)

* denotes fixed parameter

For a generic non-spherical particle, its 2D projection observed by TEM could be described by multiple parameters, some of which are illustrated in figure 3.17. One of the research questions was whether a correlation of any of these (see table 3.5) with the Morin temperature could be found. Based on figure 3.18, subject

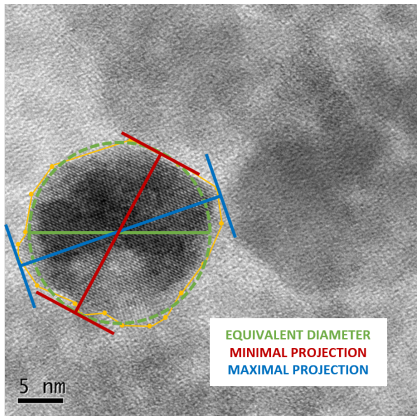

Figure 3.17: Illustration of the equivalent diameter, minimal, maximal projections of a nanoparticle as seen by TEM, processed by the NIS-Elements software by Nikon.

to the limitations described above, we can conclude that all models correlate relatively well with the equivalent diameter of the particles, while the mean-field approach is better suited for the minimal projection. It suggests that the characteristic shape of the particles has only limited effect on the Morin temperature as long as the particles have axial symmetry that, to some extent, defines the magnetic properties of small particles.

Table 3.5: Nanoparticle characteristics determined by statistical processing of TEM micrographs - mean particle sizes and standard deviation as defined by the equation 3.4, and the corresponding mean T_M derived from the temperature dependencies of magnetization (M_{ZFC} and M_{FC} curves) in [P7].

Designation	Minimal projection [nm]	Maximal projection [nm]	Equivalent diameter [nm]	T_M [K]
SM5.6	5.7(1.0)	8(1.5)	5.7(1.3)	NA
RH26	23(6)	43(22)	27(10)	186(10)
SP42	29(3)	72(11)	43(4)	215(7)
RS103	110(86)	140(103)	144(140)	254(10)

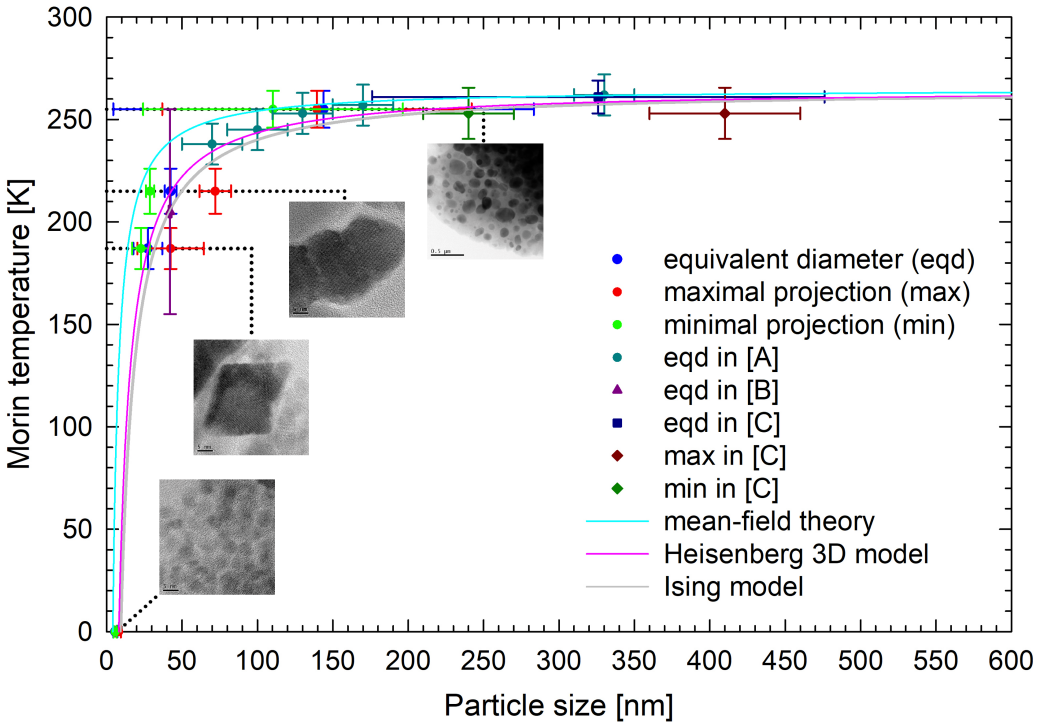

Figure 3.18: Theoretical models for the Morin transition of real systems of nanoparticles with a size distribution and their comparison with experimentally determined hematite nanoparticles dimensions and data from referenced sources. The key for the references in the legend: [A] - [68], [B] - [69], and [C] - [70]. Adapted from [P7].

Theoretical model for the transition of particles with size distribution from a blocked superspin to superparamagnetic state

Due to the fact that the blocking temperature strongly depends on the particle size, under some simplifying assumptions, it is possible to determine the mean particle size based on the temperature dependence of the Mössbauer spectra. It turns out that the developed theoretical model (formula 3.5) that describes the AF→WF spin-reorientation transition proved to be applicable for other systems of nanoparticles with a size distribution that pass from a magnetically blocked state to a superparamagnetic (SPM) state (see Section 2.4), and was further developed to determine the volume-weighted distribution of blocking temperatures as presented in figure 3.19). This was advantageously used for the Mössbauer analyzes of suspensions of ultrafine iron (oxyhydro)oxide nanoparticles for commercial parties on the market of intravenous drug products for the treatment of anemia (in the form of contract research) since their structural properties are hardly accessible by other characterization methods.

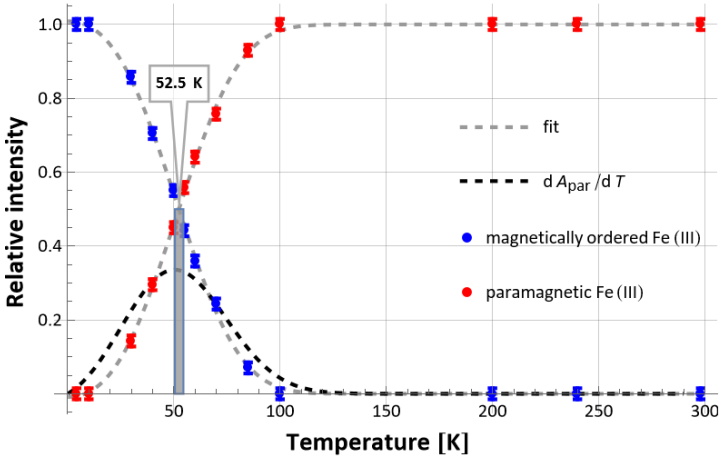

Figure 3.19: Temperature dependence of the relative intensities of the Mössbauer spectra components modelling the contribution of paramagnetic and magnetically ordered ferric iron in iron complex Venofer® samples (multiple lots) [71]. $\mathrm{d}A_{\mathrm{par}}/\mathrm{d}T$ curve is the probability distribution function of particle volume that undergoes transition from paramagnetic to magnetically ordered state at given temperature (i.e., the volume-weighted distribution of blocking temperatures).

As the real systems of particles are characteristic by distributions of chemical composition, degree of crystallinity, magnetocrystalline anisotropy constants, particle volumes and shapes; these all are reflected in the distribution of the blocking temperatures (the onset of magnetic order) as well. In the Mössbauer spectra, this is manifested in the temperature dependence of the relative contribution from paramagnetic ME active atoms in SPM particles (doublets) and magnetically ordered atoms in blocked particles (sextets) that coexist over a wide temperature range. The blocking temperature of an ensemble of particles is defined as the temperature at which 50 % of the ME active atoms contained in the sample are (super)paramagnetic and 50 % magnetically ordered (i.e., a median). In the first approximation, the effective anisotropy constant K_{eff} inversely depends on

the particle size according to the law [72] given by

$$K_{\mathrm{eff}}(d,T) = K_{\mathrm{V}}(T) + \frac{6K_{\mathrm{s}}(T)}{d}. \tag{3.7}$$

However for obvious reasons, the respective volume and surface anisotropy constants K_{v} and K_{s}, respectively, are hardly found in the literature. By analysis of series of the Mössbauer spectra collected at various temperatures, the $K_{\mathrm{eff}}V$ product (magnetocrystalline anisotropy energy) can be determined from the decrease in the observed hyperfine magnetic field of magnetically ordered ME active atoms at low temperatures (given for $K_{\mathrm{eff}}V \gg k_{\mathrm{B}}T$, usually below 10 K), where there is no relaxation present yet. If the collective magnetic excitations (CME) model [73] is adopted, then

$$B_{\mathrm{obs}}(T) = B_0\left(1 - \frac{k_{\mathrm{B}}T}{2K_{\mathrm{eff}}V}\right), \tag{3.8}$$

where B_0 is the hyperfine magnetic field in macroscopic crystals (bulk) [74], k_{B} is the Boltzmann constant, T is the temperature, and V is the volume of particles. Assuming the same effective anisotropy constant for all the particles, the median core volume V_0 (or diameter d_0, under assumption of spherical particles) of the particle ensemble can be further deduced after determination of K_{eff}. Furthermore, to determine the $K_{\mathrm{eff}}V$ product, there are multiple approaches based on magnetic field dependence of high-temperature spectra or spin-flip models that are impractical or their field of use is very limited.

Mean particle sizes determined by MS and XRPD methods are intrinsically volume-averaged. When comparing them with those determined by TEM, it must be kept in mind that the TEM results need to be transformed to volume-weighted values first ($d_{\mathrm{TEM}} \rightarrow d_{\mathrm{TEM,V}}$). The mean apparent crystallite size of nanoparticles d_{XRPD} determined by the analysis of the diffraction profiles needs to be multiplied by a Scherrer constant, which is of the order of unity and depends on the crystallite shape, to calculate the real size of particles [P6, 75]. In the case of nonmonodisperse particles, the effect of the actual size distribution of the crystallites must be included by the effective Scherrer constant.

4. Substituted magnetite and ferrite nanoparticles

Magnetic cubic ferrites with the formula $MeFe_2O_4$ (where Me stands for a divalent metal cation such as Fe^{2+}, Co^{2+}, Mn^{2+}, and others) crystallize in the spinel structure, which is described by a unit cell of 32 cubic close-packed oxide anions O^{2-} in which the metal cations occupy 8 tetrahedral (A) and 16 octahedral [B] sites (see figure 4.1). The stoichiometry, nature of the divalent cations, and their distribution among these two types of interstitial site (the so-called inversion degree) are key features to modulate the magnetic properties (e.g., saturation magnetization and magnetocrystalline anisotropy) of cubic ferrite, beyond size, shape [76], and coating-tuning approaches [P4]. For the preparation of nanoparticles with a narrow distribution of sizes, surfactants are widely used to prevent crystal formation from degradation products of precursors and to reduce agglomeration. Because of various thermodynamical stability of the precursors and kinetics of their decomposition, the prepared nanoparticles do not exactly reproduce the molar ratio of metals in an initial reaction mixture, and their actual chemical composition must be verified by physical or chemical characterization methods.

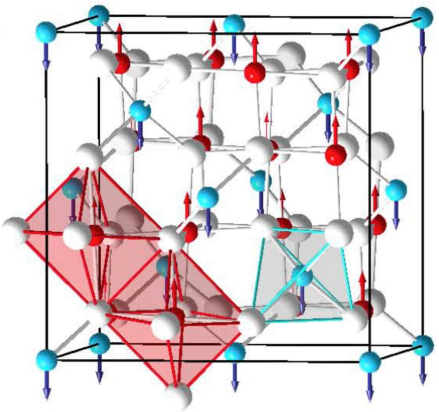

Figure 4.1: The spinel unit cell with outlined ferrimagnetic spin arrangement (antiparallel arrangement of the sublattices (A) and [B]): white spheres represent oxide anions that form the close-packed backbone in which the metal cations occupy tetrahedral (blue spheres) and octahedral (red spheres) sites [77]. Reproduced with permissions from Elsevier B.V.

The inversion degree γ of ferrite is the fraction of divalent Me^{2+} cations in the octahedral sites [78]. The limit case of $\gamma = 0$ means that no Me^{2+} cation occupies the octahedral sites, while the other limit case of $\gamma = 1$ means that all Me^{2+} cations are located within the octahedral sites. The bulk $ZnFe_2O_4$ is a system of almost normal spinel structure ($\gamma = 0.2$) due to the strong preference for Zn^{2+} cations for tetrahedral coordination. Among the studied materials, bulk cobalt ferrite ($CoFe_2O_4$) with totally inversed spinel structure ($\gamma = 1$) features the highest magnetocrystalline anisotropy constant (2.9×10^5 J.m^{-3}), which makes it a magnetically hard phase, but the higher Co toxicity compared to others may be undesirable for some applications (e.g., in medicine). Bulk manganese ferrite, with $\gamma \sim 0.2$ [79], differs by two orders of magnitude in terms of magnetocrys-

talline anisotropy, i.e., 3×10^3 J.m^{-3}, but shows higher saturation magnetization with respect to cobalt ferrite [80].

Synthesis conditions play a significant role in the cation distribution and consequent magnetic properties. Related nanosized ferrites synthetised at comparatively lower temperatures, for example, under hydrothermal conditions, by coprecipitation method or mechanochemical processing, may show a metastable cation distribution of Me^{2+} cations in the tetrahedral and octahedral sites. While in zinc ferrite prepared by wet chemistry Zn^{2+} cations still preferentially occupy tetrahedral over octahedral sites, the inversion degree of cobalt ferrite nanoparticles is usually around 0.7 [81], and considering that the octahedral sites double the number of the tetrahedral sites, the site occupancy of Co^{2+} can be considered random. Nanosized manganese ferrite shows an inversion degree of around 0.5, which means that Mn^{2+} cations also have preference for the tetrahedral sites [82].

The co-presence of more substituting divalent cations in the structure imprints different chemical and physical properties with respect to the simple combination of the single phases and allows for further tuning of properties exploitable for different applications. Mn-Zn ferrites have attracted attention because of their high saturation magnetization, high initial permeability, and low core losses. According to the previous study [P8], Mn-Zn ferrite nanoparticles synthesized under hydrothermal conditions and coated with silica exhibited negligible toxicity, superior properties in comparative studies on cytotoxicity, and transverse relaxivity. Sufficiently high values of specific absorption rate (SAR) drew attention to the use of the system in hyperthermia studies and magnetothermal release of drugs. The higher toxicity of mixed Co–Mn ferrites does not make the system a good candidate for human medicinal use; however, they are widely studied for magnetic recording or catalysis.

Magnetite is a fully inversed member of the ferrite family, Me^{2+} being Fe^{2+}, which exhibits ferrimagnetic behavior. The temperature of the Verwey transition T_V, the first-order transition associated with the change of the magnetite crystal lattice from a monoclinic structure insulator to a metallic cubic inverse spinel structure upon heating, is characteristic of the stoichiometry of the magnetite structure and the absence of impurities, as it strongly depends on the vacancies and substitutions present [83]. For nanoparticles, the observed T_V is always lower than that of the bulk material, i.e., $\sim$ 120 K [84, 85]. Importantly, both the magnitude of monoclinic distortion of the lattice and the transition temperature decrease rapidly with increasing Zn^{2+} or Co^{2+} content. For Me^{2+} concentration in the iron sites as low as $\sim$ 1.5 %, the distortion vanishes [83]. The preserved monoclinic symmetry down to low temperatures and charge localization in the octahedral sites result in distinguished Fe^{2+} and Fe^{3+} positions in the structure that greatly facilitate the interpretation of the Mössbauer spectra, which are highly sensitive to small changes in stoichiometry. The Me^{2+} substitution in the spinel structure affects the hyperfine parameters; the hyperfine field varies significantly due to the differences in the single-ion anisotropy of cations in the interstitial sites [86]. Since the A-B exchange interactions (J_{AB}) are stronger than A-A (J_{AA}) or B-B (J_{BB}), Me^{2+} present in the tetrahedral sites manifests itself in a greater relative decrease in the hyperfine field values acting on the iron nuclei occupying the octahedral sites with respect to the tetrahedral sublattice.

The general formula for the cation distribution in the magnetic cores of the

spinel structure is expected to be $(Fe^{3+}_{1-x}Me^{2+}_{x})[Fe^{3+}_{1+x+2\delta}Fe^{2+}_{1-x-y-3\delta}Me^{2+}_{y}\square_{\delta}]O_4$, where δ denotes the effective number of cation vacancies □ in the octahedral sites. The presence of vacancies in the formula reflects the overall degree of oxidation of the sample and thereby its location in the continuum between magnetite ($\delta = 0$) and maghemite phases ($\delta = 1/3$). Considering the same Lamb-Mössbauer factor for all iron atoms specifically at 4.2 K, the integral intensity of the spectral components A corresponding to the different iron sites is representative of their relative abundance in the structure, and the stoichiometric parameters can be bound into two equations for the ratios of ferric irons and all irons in tetrahedral and octahedral sites, respectively:

$$\begin{aligned} \frac{A_{(Fe^{3+})}}{A_{[Fe^{3+}]}} &= \frac{(1-x)}{(1+x+2\delta)} \\ \frac{A_{(Fe)}}{A_{[Fe]}} &= \frac{(1-x)}{(2-y-\delta)}. \end{aligned} \tag{4.1}$$

The molar ratio of Me and Fe atoms in magnetic cores determined by XRF analysis of the prepared samples (or any other relevant technique in general) supplements another binding equation $n(\mathrm{Me})/n(\mathrm{Fe}) = (x+y)/(3-x-y-\delta)$ that in combination with 4.1 provides the values of x, y and δ [P1].

4.1 Zn and Co substituted magnetite nanoparticles

Because the magnetic moments in the tetrahedral and octahedral sites are coupled antiferromagnetically, substitution of the iron cations with a nonzero magnetic moment in the tetrahedral site by zinc cations with a zero magnetic moment leads to an increase in magnetization. However, substitution is possible only up to a certain concentration of zinc, as it also disrupts the exchange interactions up to the point that the sample loses magnetic order completely. Samples with an approximate composition $Zn_cFe_{3-c}O_4$ that differ in Zn concentration ($c = 0$, 0.05, 0.36) were prepared by two-step thermal decomposition [87] in the presence of surfactants at temperatures lower than 300 °C followed by rapid cooling. The phase composition, crystal structure, and mean size of the crystallites were determined by XRPD and the actual size and morphology of the particles by TEM, see figure 4.2. The Zn:Fe molar ratios in the zinc-containing samples are based on XRF spectra, while the concentration of silica-coated particles in aqueous suspensions was accurately determined by chemical analysis of iron by atomic absorption spectroscopy with flame atomization (AAS). The Zn content derived by XRF is in good agreement with that found by AAS for nanoparticles with $c = 0.36$. The basic characterization is augmented by magnetic measurements of hysteresis curves and zero-field-cooled/field-cooled susceptibilities in low magnetic fields carried out by using SQUID magnetometry and Mössbauer spectroscopy in a wide temperature range. The nanoparticles prepared by thermal decomposition rapidly oxidize during the purification process as a result of exposure to oxygen in air. If we assume that the oxidation progresses from the surface area inward, the interface (capping) layer of a maghemite-type structure might be formed. In

most cases of nanoparticle systems, Mössbauer spectroscopy cannot distinguish whether the acquired spectra represent a mixture of magnetite and maghemite, or a non-stoichiometric compound, where missing iron cations are quantified by vacancies □ due to partial oxidation of the substituted magnetite.

Table 4.1: Structural and magnetic characteristics of the F and ZF magnetic nanoparticles. Parameter designations: a - lattice constant, d_{X} - mean apparent size determined by XRPD and derived mean crystallite size, or mean particle size determined by TEM and derived volume-averaged equivalent, pdi_{TEM} - respective polydispersity index, M - magnetization.

Designation	Composition	a [Å]	d_{XRPD} [nm]	d_{cryst} [nm]	d_{TEM} [nm]	pdi_{TEM}	$d_{\mathrm{TEM,V}}$ [nm]	M @ 300 K, 3 T [Am^2/kg]	Cation distribution
F	$Fe_{2.8}\square_{0.2}O_4$	8.3797(4)	14	18.7	11.2	0.39	11.1	68	$(Fe^{3+})[Fe^{3+}_{1.40}Fe^{2+}_{0.40}0\square_{0.20}]O_4$
ZF(0.05)	$Zn_{0.05}Fe_{2.65}\square_{0.30}O_4$	8.3845(15)[1]	9	12	10.6	0.19	9.3	65	$(Fe^{3+}_{0.97}Zn^{2+}_{0.03})$
		8.3495(9)[2]	20	26.7					$[Fe^{3+}_{1.63}Fe^{2+}_{0.05}Zn^{2+}_{0.02}\square_{0.30}]O_4$
ZF(0.36)	$Zn_{0.36}Fe_{2.54}\square_{0.10}O_4$	8.3903(4)	18	24	5.1	0.15	4.5	73	$(Fe^{3+}_{0.82}Zn^{2+}_{0.18})$
					14.4	0.06	11.1		$[Fe^{3+}_{1.37}Fe^{2+}_{0.35}Zn^{2+}_{0.18}\square_{0.10}]O_4$
ZF(0.36) @SiO_2 (8.8 nm)	$Zn_{0.36}Fe_{2.45}\square_{0.19}O_4$	-	-	-	-	-	-	10	$(Fe^{3+}_{0.86}Zn^{2+}_{0.14})$
									$[Fe^{3+}_{1.51}Fe^{2+}_{0.08}Zn^{2+}_{0.22}\square_{0.19}]O_4$

[1] for cubic magnetite
[2] for cubic maghemite

The Rietveld refinement of the XRPD patterns acquired at room temperature revealed a single phase cubic spinel structure of Fe_3O_4 with the $Fd\bar{3}m$ space group for all samples, except for nanoparticles with $c = 0.05$, where also a 35(2) % contribution of cubic γ-Fe_2O_3 phase with $P4_332$ space group was observed. Furthermore, the estimated residual content of the surfactant from the elemental analysis of CHNS was approximately 6 wt% (monomolecular layer on the surface). The selected characteristics of the samples are summarized in table 4.1.

For studies of the temperature and magnetic field dependencies of the magnetic resonance relaxivities, the magnetic cores with the highest zinc concentration were encapsulated into an amorphous silica shell of various thicknesses (4.9(8) nm, 6.9(8) nm, 7.4(6) nm and 8.8(8) nm) by the reverse microemulsion method to obtain suspensions with desired concentrations of magnetically active atoms for the experiments. The fraction of smaller particles was partially dissolved as a result of mild acid leaching during the coating, thus slightly changing the size distribution of the magnetic cores. Around 10 % of the product constitutes the chain clusters of the finest nanoparticles coated as a single whole body. The encapsulation process caused a partial oxidation of Fe^{2+} cations in the octahedral sites, however, did not alter significantly magnetic properties of the system.

The Mössbauer spectra acquired at room temperature show the presence of a magnetically ordered phase (manifested by a sextet) affected by the relaxation effects at the timescales probed by Mössbauer spectroscopy, thus representative of the nanoparticles in a superparamagnetic regime (spectra not presented here). The Mössbauer spectra acquired at 4.2 K and shown in figure 4.3, where thermal fluctuation of the direction of magnetic moments diminishes and the nanoparticles are in the so-called blocked state, closely resemble those recorded at temperatures well above the expected onset of the Verwey transition of magnetite nanoparticles (spectra acquired at 120 and 130 K not presented here), suggesting that the investigated nanoparticles do not undergo the Verwey transition. Together with

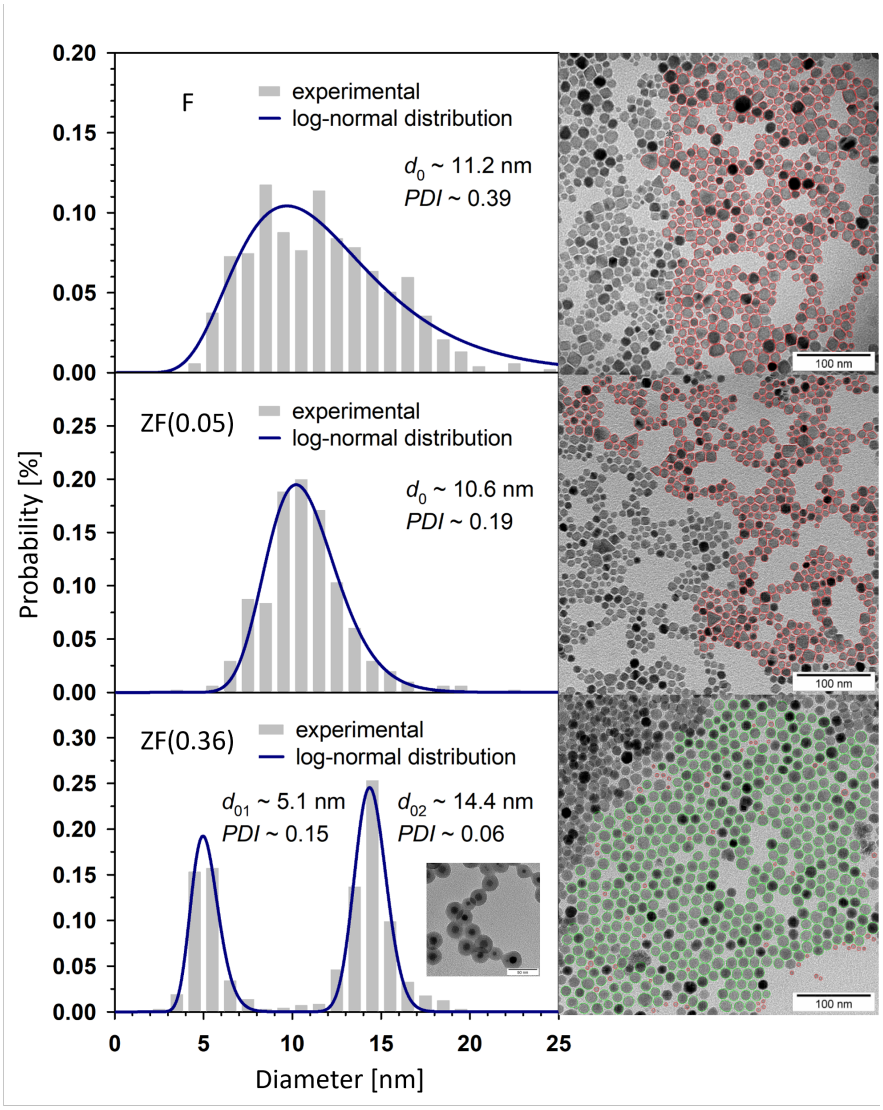

Figure 4.2: (Left) size distributions of equivalent diameters determined from bright-field TEM micrographs (right) of the synthesised nanoparticles presented in the order of increasing zinc concentration, fitted under the assumption of the lognormal distribution profile. Inset figure - TEM micrograph of ZF(0.36) encapsulated in 8.8-nanometer thick amorphous silica shell. Around 500 particles were statistically processed by the NIS-Elements software by Nikon using spheroidal approximation.

in-field spectra, they evidence for a long-range ferrimagnetic order, even though it was not possible to unambiguously resolve the spectra acquired in a zero field because of the large overlap of the components originating iron nuclei in tetrahedral and octahedral sites and strong correlation of the fitation parameters.

In the applied field, the vector of magnetization, given by the uncompensated magnetic moments of Fe^{3+} ions in octahedrally coordinated sites, is expected to turn into the direction of the external magnetic field due to the generally low magnetocrystalline anisotropy of the studied samples (as suggested by low coercivity). The application of an external magnetic field B_{ext} of 6 T enabled the separation of spectral components due to the shift of the effective magnetic field B_{eff} acting on the ^{57}Fe nuclei of the two magnetic sublattices in an opposite di-

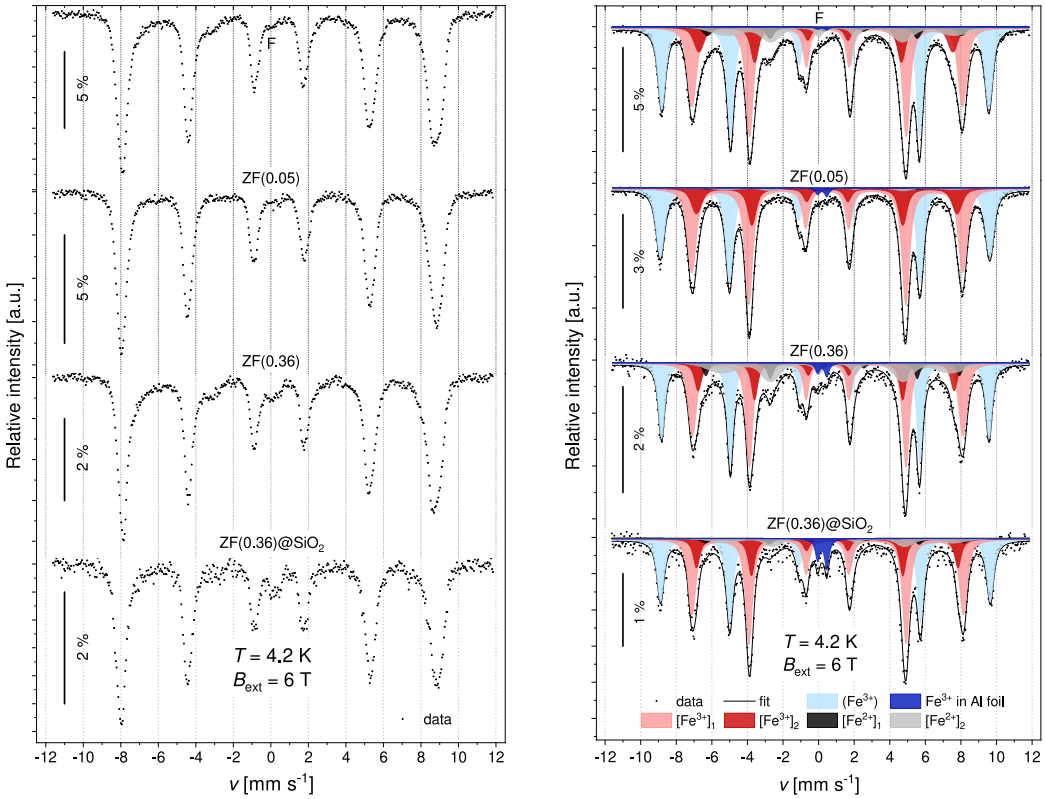

Figure 4.3: Mössbauer spectra of the F and ZF magnetic nanoparticles acquired at liquid helium temperature (4.2 K) without (left) and in external magnetic field of 6 T (right). The light blue component represents Fe^{3+} in the tetrahedral sublattice, the red components Fe^{3+} and the gray components Fe^{2+} in the octahedral sublattice. The minor doublet in dark blue represents a parasitic signal originating from the experimental setup.

rection according to equation $B_{\text{eff}} \approx B_{\text{hf}} \pm B_{\text{ext}}$, where the operators + and - are applied to the tetrahedral and octahedral sites, respectively. This happens as the hyperfine magnetic field acting on the ^{57}Fe nuclei is oriented antiparallel to the direction of the magnetic moments of iron ions as can be seen in figure 4.1. The fit of the in-field Mössbauer spectra clearly resolves three sextets with a distribution of the effective hyperfine magnetic field, one attributed to Fe^{3+} in the tetrahedral site and two others that most likely simulate a distribution of local environments of Fe^{3+} in the octahedral site, well distinguished by their characteristic isomer shifts. It is not possible to unambiguously ascribe the hyperfine parameters of Fe^{2+} in the octahedral sites as they strongly correlate with the fit parameters of the individual spectral components. Their contribution to the spectra was modeled by two sextets with a distribution of the effective hyperfine magnetic field. The hyperfine parameters and other characteristics of the spectra are summarized in table 4.2.

Knowing the exact relative Zn content from XRF and iron site occupancies from Mössbauer spectroscopy, the actual stoichiometry and Zn^{2+} cation distribution in the tetrahedral and octahedral sites of the crystal lattice were suggested for all the samples and are listed in table 4.2. The accuracy of the nominal composition is in the order of 1 % except for the last sample with worse Mössbauer data statistics, where we estimate the error of 3-4%. In contrast to the bulk,

Table 4.2: Spectral characteristics determined from the Mössbauer spectra of the F and ZF samples acquired at liquid helium temperature (4.2 K) in external magnetic field of 6 T. Individual components are designated by parentheses ( ) or [ ] to indicate tetrahedral or octahedral sites, respectively. Parameter designations: B_{ext} - applied external magnetic field, IS - isomer shift, QS - quadrupole shift, $\bar{B}_{\mathrm{eff}}$ - mean effective hyperfine magnetic field on ^{57}Fe nuclei $B_{\mathrm{eff}} = |\vec{B}_{\mathrm{hf}} - \vec{B}_{\mathrm{ext}}|$ (where $\vec{B}_{\mathrm{hf}}$ is a hyperfine magnetic field) and its distribution width ΔB_{eff}, Γ - Lorentz linewidth, A - area fraction of the given component.

Sample	Component	IS [mm/s]	QS [mm/s]	$\bar{B}_{\mathrm{eff}}$ [T]	ΔB_{eff} [T]	Γ [mm/s]	A
F	(Fe^{3+})	0.37(2)	0.00(2)	57.1(2)	1.4(2)	0.42(2)	0.35(1)
	$[Fe^{3+}]_1$	0.50(2)	-0.03(2)	47.3(2)	2.0(2)	0.42(2)	0.38(1)
	$[Fe^{3+}]_2$	0.47(2)	-0.12(3)	44.2(3)	2.4(5)	0.42(2)	0.12(1)
	$[Fe^{2+}]_1$	1.14(3)	0.21(7)	39.9(3)	10(1)	0.42(2)	0.11(1)
	$[Fe^{2+}]_2$	1.15(3)	-0.53(9)	44.4(6)	2.8(8)	0.42(2)	0.04(1)
ZF(0.05)	(Fe^{3+})	0.36(2)	0.01(2)	57.5(2)	1.7(2)	0.45(2)	0.36(1)
	$[Fe^{3+}]_1$	0.49(2)	0.01(2)	47.4(2)	1.8(3)	0.45(2)	0.46(2)
	$[Fe^{3+}]_2$	0.49(2)	-0.01(3)	45.7(2)	2.4(6)	0.45(2)	0.15(2)
	$[Fe^{2+}]_1$	1.14*	0.21*	39.9*	10*	0.45(2)	0.018(4)
	$[Fe^{2+}]_2$	1.15*	-0.53*	44.4*	2.8*	0.45(2)	0.006(5)
ZF(0.36)	(Fe^{3+})	0.37(2)	0.01(2)	57.2(2)	1.0(3)	0.38(2)	0.32(1)
	$[Fe^{3+}]_1$	0.51(2)	0.04(3)	46.7(2)	2.4(3)	0.38(2)	0.38(2)
	$[Fe^{3+}]_2$	0.51(3)	-0.39(7)	45.3(3)	4.8(5)	0.38(2)	0.13(2)
	$[Fe^{2+}]_1$	1.20(4)	0.03(2)	39.6(5)	10(1)	0.38(2)	0.13(3)
	$[Fe^{2+}]_2$	1.20(6)	-0.47(7)	44.7(6)	0.6(2)	0.38(2)	0.04(3)
ZF(0.36)@SiO_2	(Fe^{3+})	0.37(2)	0.02(2)	57.6(2)	1.0(3)	0.43(2)	0.34(3)
	$[Fe^{3+}]_1$	0.51(2)	0.01(2)	47.4(3)	1.3(5)	0.43(2)	0.43(4)
	$[Fe^{3+}]_2$	0.49(3)	0.00(2)	45.6(5)	0.4(2)	0.43(2)	0.15(5)
	$[Fe^{2+}]_1$	1.23(4)	0.10(7)	39.9(5)	9.0(9)	0.43(2)	0.06(1)
	$[Fe^{2+}]_2$	1.22(5)	-0.50(7)	45.1(7)	9.0*	0.43(2)	0.02(1)

* denotes fixed parameter

regardless of the strong Zn^{2+} preference to occupy tetrahedral site, nearly half of the cations occupy the octahedral sites in the same manner as in nanoparticles of zinc ferrite prepared by ball-milling [77, 88].

Magnetic nanoparticles are promising candidates as contrast agents for magnetic resonance imaging (MRI), which itself belongs to the most widely used non-invasive and non-ionizing tools of clinical diagnostics. Since magnetization M is together with the particle radius r and water diffusion coefficient D the leading parameter in transversal relaxivity for particles under the motional averaging regime (MAR) [89] (i.e., $r_{2,\mathrm{MAR}} \propto r^2 M^2(t)/D_{\mathrm{H_2O}}(t)$) and the presence of zinc atoms in the spinel ferrite structure lead to the increase in net magnetization, silica-coated particles were used for relaxometric studies in a manner similar to [P8, P5]. Transversal relaxivities r_2 are given by the slopes of linear regression functions that fit the reciprocal proton relaxation time $1/T_2$ versus the iron concentration in a suspension in a linear region. The highest observed

value of the transverse relaxivity r_2 is $\sim$ 324 mM(Fe)$^{-1}$s^{-1} at 3 T for the silica coating thickness of 6.9(8) nm (see figure 4.4). This is slightly higher than that reported for iron oxide nanoparticles and commercial (SuperParamagnetic Iron Oxide Nanoparticles) SPION-based contrast agents. The temperature dependence of r_2 in magnetic fields 0.47 and 11.75 T follows the thermal evolution of magnetization and self-diffusion coefficient of water, while the magnetic field dependence shows an atypical nonmonotonous character (data not presented here). The results of the presented analyses together with the relaxivity study are to be published.

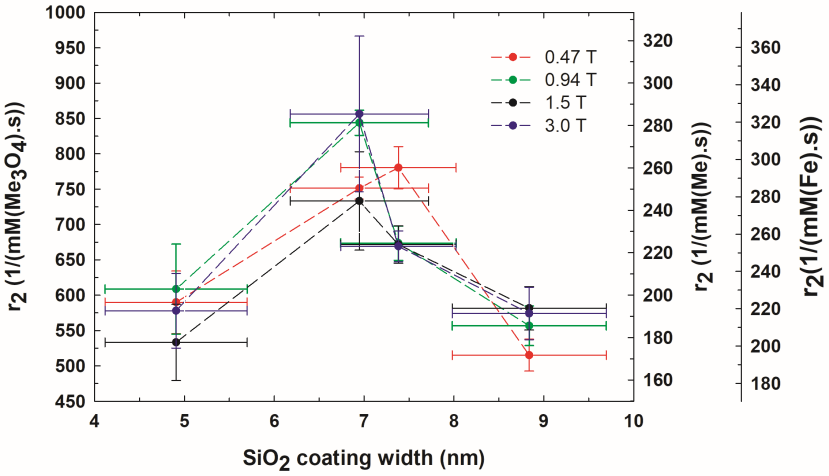

Figure 4.4: Transversal relaxivity r_2 of ZF(0.36)@SiO_2 nanoparticles in dependence on silica coating thickness and applied external magnetic field. The three scales for r_2 correspond to various expressions for the concentration of the active component (taken per concentration of Me_3O_4, concentration of all metallic atoms Me and concentration of Fe only). Connecting lines are just a guide for the eye.

Co and Zn ferrite nanoparticles

In a follow-up study that aimed to study the relaxation mechanisms by custom-made magnetic particle spectrometer (MPS) (see Chapters 5 and 6), magnetic nanoparticles of two different compositions based on cobalt and zinc ferrites were chosen due to their different magnetic behavior at room temperature. While cobalt ferrites possess higher magnetocrystalline anisotropy, ensuring that the nanoparticles are in a blocked state, zinc ferrites are distinguished by high magnetization and superparamagnetic behavior. The nanoparticles of $Co_{0.68}Fe_{2.30}O_4$ and $Zn_{0.34}Fe_{2.51}O_4$ (denoted as CF-td and ZF-td) were prepared using a two-step thermal decomposition method similar to that mentioned previously [87]. Because of the specifics of the method, the particles possess a capping layer of oleic acid and oleylamine and are thus hydrophobic, forming colloidally stable suspensions in nonpolar organic solvents. Two more samples with compositions of $Co_{1.06}Fe_{1.94}O_4$ and $Zn_{0.32}Fe_{2.52}O_4$ (denoted as CF-h and ZF-s) were synthesized under solvothermal and hydrothermal conditions, respectively. All the samples

were synthetized at relatively low temperatures below 300 °C. The solvothermally prepared ZF-s were stabilized with citrate. The synthesized nanoparticles were characterized by XRPD, TEM, and the citrate-stabilized sample ZF-s also by XRF. The magnetic properties of the bare particles thoroughly purified to remove residual surfactants were studied by SQUID magnetometry in DC fields [P1]. The selected parameters of the samples can be found in table 6.1.

Mössbauer spectra acquired at 4.2 K and shown in figure 4.5 evidence for a long-range ferrimagnetic order for all CF and ZF samples based on change of in-field spectra from those without; the rationale for the application of in-field Mössbauer spectroscopy and the processing of the acquired spectra follow the procedures described in the previous section. Each of the individual Fe sites in the in-field spectra was fitted by several magnetically split sextets, which account for the Co or Zn cation distribution and vacancies in their second coordination sphere. Although the areas of these subcomponents are subject to some uncertainty, the total area fraction of all Fe in the tetrahedral or octahedral sites is a reliable parameter. The hyperfine parameters are summarized in tables 4.3 and 4.5 and respective cation distributions in table 4.4.

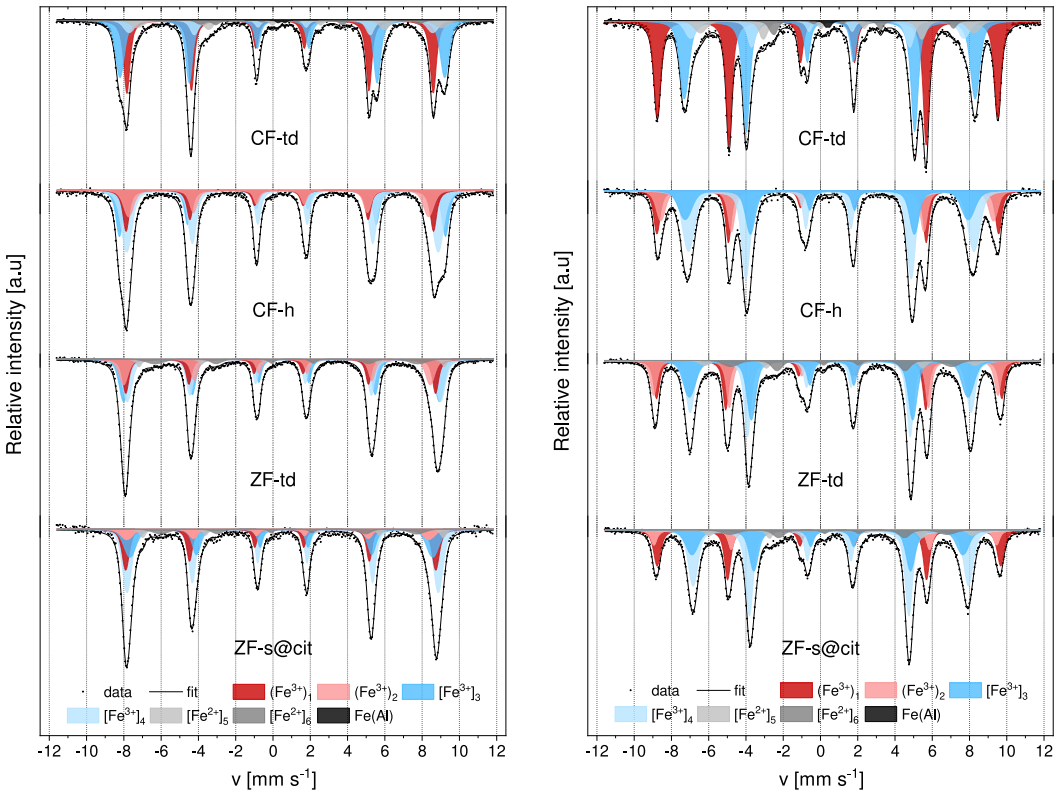

Figure 4.5: Mössbauer spectra of the CF and ZF magnetic nanoparticles acquired at liquid helium temperature (4.2 K) without (left) and in external magnetic field of 6 T (right). The red components represent Fe^{3+} in the tetrahedral sublattice, the blue components Fe^{3+} and the gray components Fe^{2+} in the octahedral sublattice. The minor doublet given in black represents a parasitic signal originating from the experimental setup.

Table 4.3: Spectral characteristics determined from the Mössbauer spectra of the CF samples acquired at liquid helium temperature (4.2 K). Individual components are designated by parentheses ( ) or [ ] to indicate tetrahedral or octahedral sites, respectively. Parameter designations: B_{ext} - applied external magnetic field, IS - isomer shift, QS - quadrupole shift, $\bar{B}_{\text{eff}}$ - mean effective hyperfine magnetic field on ^{57}Fe nuclei $B_{\text{eff}} = |\vec{B}_{\text{hf}} - \vec{B}_{\text{ext}}|$ (where $\vec{B}_{\text{hf}}$ is the hyperfine magnetic field) and its distribution width ΔB_{eff}, Γ - Lorentz linewidth, A - area fraction of the given component.

Designation	B_{ext} [T]	Component	IS [mm/s]	QS [mm/s]	$\bar{B}_{\text{eff}}$ [T]	ΔB_{eff} [T]	Γ [mm/s]	A
CF-td	0	$(Fe^{3+})_1$	0.38(2)	-0.01(2)	51.1(2)	0.8(2)	0.35(2)	0.392*
		$[Fe^{3+}]_2$	0.53(2)	-0.05(2)	54.1(2)	2.1(2)	0.35(2)	0.40*
		$[Fe^{3+}]_3$	0.46(2)	-0.07(4)	50.6(2)	3.1(5)	0.35(2)	0.11*
		$[Fe^{2+}]_4$	1.07(3)	-0.39(6)	50.7(3)	4.2(6)	0.35(2)	0.077*
		$[Fe^{2+}]_5$	1.16(4)	1.63(7)	36.5(4)	2.3(9)	0.35(2)	0.030*
	6	$(Fe^{3+})_1$	0.38(2)	-0.01(2)	56.8(2)	1.3(2)	0.34(2)	0.392(8)
		$[Fe^{3+}]_2$	0.52(2)	-0.03(2)	48.5(2)	2.4(2)	0.34(2)	0.40(1)
		$[Fe^{3+}]_3$	0.46(2)	-0.17(3)	45.6(3)	3.3(5)	0.34(2)	0.11(1)
		$[Fe^{2+}]_4$	1.05(3)	-0.29(4)	45.7(2)	3.6(5)	0.34(2)	0.077(5)
		$[Fe^{2+}]_5$	1.32(3)	1.85(5)	30.4(3)	1.1(9)	0.34(2)	0.030(3)
CF-h	0	$(Fe^{3+})_1$	0.34(2)	0.04(2)	51.3(2)	0.7(3)	0.36(2)	0.186*
		$(Fe^{3+})_2$	0.35(2)	-0.09(3)	50.0(2)	2.7(3)	0.36(2)	0.172*
		$[Fe^{3+}]_3$	0.50(2)	0.02(2)	54.3(2)	1.1(2)	0.36(2)	0.22*
		$[Fe^{3+}]_4$	0.51(2)	-0.01(2)	52.0(2)	2.9(2)	0.36(2)	0.42*
	6	$(Fe^{3+})_1$	0.38(2)	0.02(2)	57.0(2)	1.0(3)	0.34(2)	0.187(8)
		$(Fe^{3+})_2$	0.37(2)	-0.04(2)	55.5(2)	2.3(3)	0.34(2)	0.171(9)
		$[Fe^{3+}]_3$	0.49(2)	-0.30(5)	47.2(2)	4.2(3)	0.34(2)	0.22(3)
		$[Fe^{3+}]_4$	0.51(2)	0.15(3)	47.6(2)	3.5(2)	0.34(2)	0.42(2)

* denotes fixed parameter

Table 4.4: Cation distribution determined by a combination of XRF and Mössbauer spectroscopy, $n_{\text{Me}}/n_{\text{Fe}}$ gives the Zn (or Co, respectively) to Fe ratio according to XRF analysis.

Sample	$n_{\text{Me}}/n_{\text{Fe}}$	Cation distribution
CF-td	0.300(4)	$(Fe^{3+}_{0.89}Co^{2+}_{0.11})[Fe^{3+}_{1.15}Fe^{2+}_{0.26}Co^{2+}_{0.57}\square_{0.02}]O_4$
CF-h	0.548(13)	$(Fe^{3+}_{0.70}Co^{2+}_{0.30})[Fe^{3+}_{1.24}Co^{2+}_{0.76}]O_4$
ZF-td	0.134(2)	$(Fe^{3+}_{0.85}Zn^{2+}_{0.15})[Fe^{3+}_{1.45}Fe^{2+}_{0.21}Zn^{2+}_{0.19}\square_{0.15}]O_4$
ZF-s@cit	0.122(10)	$(Fe^{3+}_{0.73}Zn^{2+}_{0.27})[Fe^{3+}_{1.59}Fe^{2+}_{0.20}Zn^{2+}_{0.05}\square_{0.16}]O_4$

Table 4.5: Spectral characteristics determined from the Mössbauer spectra of the ZF samples acquired at liquid helium temperature (4.2 K). Individual components are designated by parentheses ( ) or [ ] to indicate tetrahedral or octahedral sites, respectively. Parameter designations: B_{ext} - applied external magnetic field, IS - isomer shift, QS - quadrupole shift, $\bar{B}_{\text{eff}}$ - mean effective hyperfine magnetic field on ^{57}Fe nuclei $B_{\text{eff}} = |\vec{B}_{\text{hf}} - \vec{B}_{\text{ext}}|$ (where $\vec{B}_{\text{hf}}$ is the hyperfine magnetic field) and its distribution width ΔB_{eff}, Γ - Lorentz linewidth, A - area fraction of the given component.

Designation	B_{ext} [T]	Component	IS [mm/s]	QS [mm/s]	$\bar{B}_{\text{eff}}$ [T]	ΔB_{eff} [T]	Γ [mm/s]	A
ZF-td	0	$(Fe^{3+})_1$	0.36(2)	0.11(2)	51.7(2)	1.0(3)	0.32(2)	0.17*
		$(Fe^{3+})_2$	0.37(2)	-0.33(5)	51.1(3)	2.3(3)	0.32(2)	0.17*
		$[Fe^{3+}]_3$	0.52(3)	-0.13(7)	52.7(2)	2.3(3)	0.32(2)	0.28*
		$[Fe^{3+}]_4$	0.50(3)	0.17(5)	52.2(2)	2.6(3)	0.32(2)	0.30*
		$[Fe^{2+}]_5$	0.96(3)	0.11(4)	50.8(2)	0.0(2)	0.32(2)	0.034*
		$[Fe^{2+}]_6$	0.88(3)	-0.32(6)	43.8(3)	5.9(6)	0.32(2)	0.054*
	6	$(Fe^{3+})_1$	0.38(2)	0.18(3)	57.6(2)	0.8(3)	0.34(2)	0.17(1)
		$(Fe^{3+})_2$	0.37(2)	-0.18(3)	57.4(2)	1.2(3)	0.34(2)	0.17(3)
		$[Fe^{3+}]_3$	0.53(2)	-0.17(3)	46.5(2)	3.6(2)	0.34(2)	0.28(3)
		$[Fe^{3+}]_4$	0.50(2)	0.10(2)	46.9(2)	2.0(2)	0.34(2)	0.30(3)
		$[Fe^{2+}]_5$	1.17(3)	-0.26(6)	45.1(3)	2.6(8)	0.34(2)	0.033(5)
		$[Fe^{2+}]_6$	1.11(3)	0.01(5)	36.9(3)	4.7(7)	0.34(2)	0.055(8)
ZF-s@cit	0	$(Fe^{3+})_1$	0.38(2)	0.07(3)	51.7(2)	1.6(3)	0.30(2)	0.21*
		$(Fe^{3+})_2$	0.34(7)	-0.16(11)	50.4(5)	3.5(3)	0.30(2)	0.08*
		$[Fe^{3+}]_3$	0.52(3)	-0.15(4)	50.5(3)	3.8(5)	0.30(2)	0.22*
		$[Fe^{3+}]_4$	0.51(2)	0.01(3)	51.9(2)	2.6(3)	0.30(2)	0.40*
		$[Fe^{2+}]_5$	1.06(3)	0.02(4)	50.1(2)	1.0(6)	0.30(2)	0.038*
		$[Fe^{2+}]_6$	0.92(4)	-0.16(7)	42.7(4)	5.2(8)	0.30(2)	0.048*
	6	$(Fe^{3+})_1$	0.40(2)	0.10(2)	57.3(2)	1.2(3)	0.36(2)	0.21(1)
		$(Fe^{3+})_2$	0.39(2)	-0.27(3)	57.1(2)	0.5(8)	0.36(2)	0.08(1)
		$[Fe^{3+}]_3$	0.50(2)	-0.26(5)	45.2(2)	3.6(3)	0.36(2)	0.22(3)
		$[Fe^{3+}]_4$	0.51(2)	0.08(2)	45.9(2)	2.4(2)	0.36(2)	0.40(2)
		$[Fe^{2+}]_5$	1.23(3)	-0.25(5)	43.9(3)	2.1(8)	0.36(2)	0.038(4)
		$[Fe^{2+}]_6$	1.05(4)	-0.17(7)	36.2(4)	5.0(9)	0.36(2)	0.049(6)

* denotes fixed parameter

4.2 Mn-Zn ferrite nanoparticles

The present study attempts to demonstrate that roughly 10 nm-sized Mn-Zn ferrite (denoted as MZF) particles, whose superparamagnetic state can be easily controlled by varying their chemical composition (Mn:Zn ratio), are suitable candidates for applications where careful adjustment of relaxation behavior and reasonably high magnetization are important. Five samples with an approximate composition of $Mn_{1-x}Zn_xFe_2O_4$ (x = 0.21–0.63) were prepared by a surfactant-free hydrothermal procedure at a rather low temperature of 180 °C. Besides basic characterizations by XRPD, XRF and TEM accompanied by chemical mapping, detailed magnetic measurements in DC fields by SQUID magnetometry and transmission Mössbauer spectroscopy were used, all described in detail in [P3]. Because the cation distribution should also be considered when developing magnetic nanoparticles with desired magnetic behavior, a neutron diffraction study at low temperatures and calculations based on DFT were carried out for the selected MZF composition. This particularly concerns the location of Zn^{2+} cations and their key role in magnetization and relaxation.

The structural and magnetic characteristics of the MZF samples are summarized in table 4.6. The refined values of the lattice parameter a from XRPD at room temperature show a systematic but weak decrease of the lattice constant with increasing zinc content caused by slightly smaller effective ionic radii of Zn^{2+} compared to high-spin Mn^{2+} [90]. Within the entire range of MZF composition under study, XRPD confirmed the single-phase character of the nanoparticles with the typical cubic spinel structure of the $Fd\bar{3}m$ symmetry. Analysis of the XRPD line broadening provided the mean size of crystallites that was gradually decreasing with increasing zinc content, in the same manner as volume-weighted TEM diameters of MZF samples of two limit compositions that confirmed also the unimodal size distribution of synthesized nanoparticles. On the timescale of magnetic measurements, the room-temperature loops were seemingly anhysteretic, which means that either the samples showed very low coercivity that was below the experimental limit (given by remnant fields in the SQUID superconducting solenoid) or the samples were already in the superparamagnetic regime.

The Mössbauer spectra acquired at room temperature and shown in figure 4.6 consist of two contributions - nanoparticles in a SPM regime, which manifest

Table 4.6: Structural and magnetic characteristics of the Mn-Zn ferrite magnetic nanoparticles. Parameter designations: a - lattice constant, d_X - mean apparent size determined by XRPD, or mean particle size determined by TEM and derived volume-averaged equivalent, SD - respective standard deviations, M - magnetization.

Designation	Composition	a [Å]	d_{XRPD} [nm]	d_{TEM} [nm]	SD_{TEM} [nm]	$d_{TEM,V}$ [nm]	$SD_{TEM,V}$ [nm]	M @ 300 K, 3 T [Am²/kg]
MZF(0.21)	$Mn_{0.82}Zn_{0.21}Fe_{1.97}O_4$	8.4684(1)	14	14	5	20	11	67
MZF(0.32)	$Mn_{0.69}Zn_{0.32}Fe_{1.99}O_4$	8.4540(1)	12	-	-	-	-	61
MZF(0.41)	$Mn_{0.62}Zn_{0.41}Fe_{1.97}O_4$	8.4498(1)	11	-	-	-	-	57
MZF(0.54)	$Mn_{0.52}Zn_{0.54}Fe_{1.94}O_4$	8.4416(1)	11	-	-	-	-	46
MZF(0.63)	$Mn_{0.42}Zn_{0.63}Fe_{1.95}O_4$	8.4345(1)	10	9	2.2	14	10	29

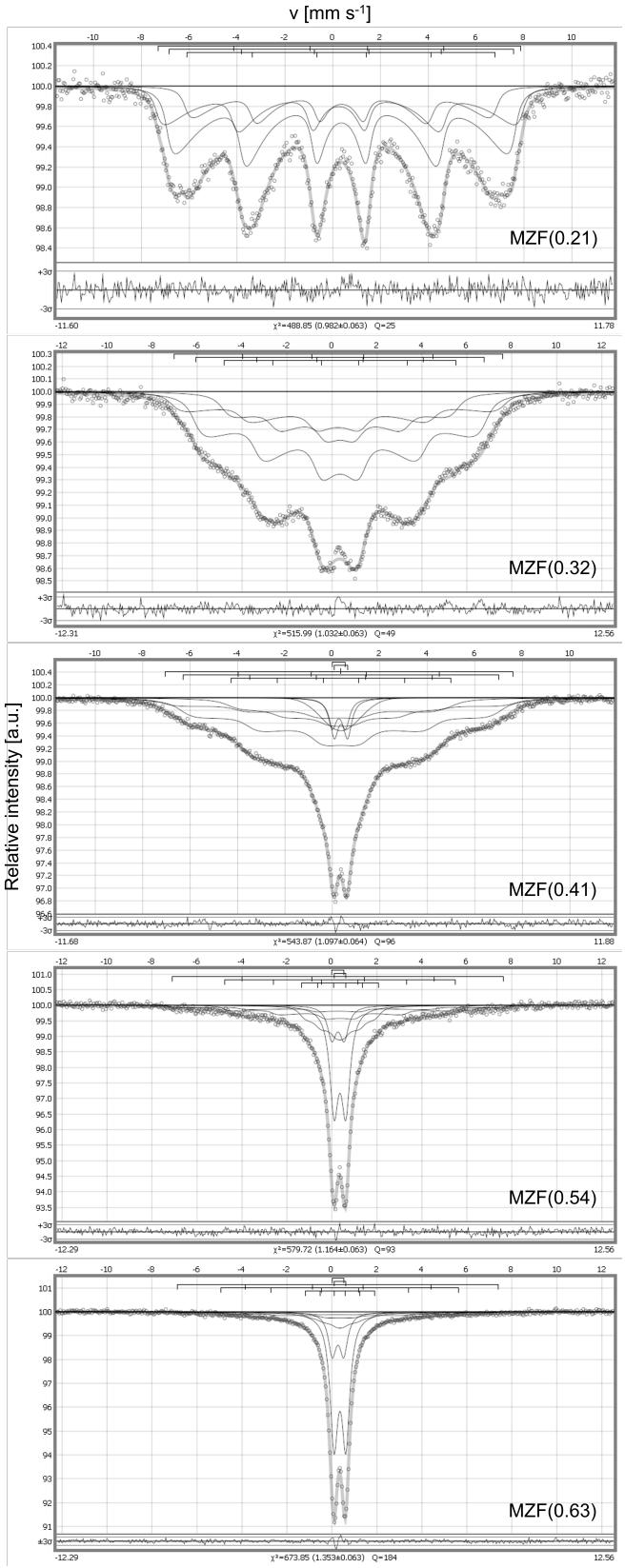

Figure 4.6: Room-temperature Mössbauer spectra of Mn-Zn ferrite nanoparticles of different compositions and mean sizes, decreasing from 14 nm to 10 nm with the increasing zinc content. The parameters of the fitted components can be found in table 4.7.

themselves by collapsed doublet components in the spectra modeled by pseudo-Voigt doublets, and nanoparticles in a transition state and a blocked state, modeled by many-state superparamagnetic relaxation components (see Section 2.4). The relative amounts of iron at the tetrahedral and octahedral sites were based on the Mössbauer spectra acquired at 4.2 K in an external magnetic field of 6 T (see figure 4.8(left) at the end of the Chapter and table 4.8), where it was possible to discern the respective spectral components. Based on the best χ^2 value within the series of samples, the isomer shifts were fixed during the fitting process; the quadrupole shifts of all magnetically split components converged close to zero value, typical for the random distribution of the angles between the principal axis of the EFG tensor and the direction of the hyperfine magnetic field. The line intensities ratio approached the typical values for powder samples, i.e., 3:2:1:1:2:3, and was therefore fixed.

Although room temperature Mössbauer spectra, shown in figure 4.6, are not suitable for the determination of the cation distribution, together with temperature-variable magnetic measurements presented in [P3] they provide valuable insight into the blocking behavior of particles on two distinct time scales and demonstrate that Néel relaxation can be enhanced by increasing the zinc content. Macroscopically, a higher concentration of diamagnetic Zn^{2+} ions also leads to a certain decrease in magnetocrystalline anisotropy [91]. The chosen relaxation model allows for a rough estimate of the magnetocrystalline anisotropy energy $K_{\text{eff}}V$, which approximates the height of the energy barrier the particle spin must overcome by Néel relaxation to minimize its energy (see figure 2.5). The zero-field Néel relaxation time is given by the relation 5.2. The refined parameters of the fits are provided in table 4.7.

The rationale for the application of in-field Mössbauer spectroscopy and the processing of the acquired spectra follow the procedures described in Section 4.1. Mössbauer spectra acquired at 4.2 K (see figure 4.8 at the end of the Chapter) evidence for a long-range ferrimagnetic order for all MZF samples based on change of in-field spectra from those without; however, it was not possible to unambiguously resolve the spectra acquired in a zero field. The in-field spectra shown in figure 4.8(left) resolved two sextets with a distribution of hyperfine fields - the one centered at a hyperfine magnetic field of 57 T with relatively smaller isomer shifts (both typical for spinel ferrites) is attributed to Fe^{3+} in the tetrahedral sites, while the other centered at a hyperfine magnetic field of 45 T to Fe^{3+} in the octahedral sites. The presence of diamagnetic Zn^{2+} in tetrahedral sites instead of magnetically active Fe^{3+}, apparent from the area fraction of the respective spectral component, leads to weakening of the superexchange interaction ($J_{\text{AB}} > J_{\text{AA}}$ or J_{BB}) with the ^{57}Fe resonating nuclei located in the octahedral sites and manifests itself in the asymmetric broadening of the distributions of effective hyperfine fields towards lower fields as can be seen in figure 4.8(left). In the case of a random distribution of zinc in these sites, its occurrence among the nearest neighbours of ^{57}Fe resonating nuclei located in the octahedral sites is given by the binomial distribution. The broadening of effective hyperfine field distribution in the tetrahedral sites can be well correlated with the zinc concentration in the structure. The hyperfine parameters and other characteristics of the spectra are summarized in table 4.8.

In this system of nanoparticles, a distinction between the core and shell con-

Table 4.7: Spectral characteristics determined from the Mössbauer spectra of the MZF samples acquired at room temperature (296 K). Individual components are designated by parentheses ( ) or [ ] to indicate the tetrahedral or octahedral sites, respectively. Parameter designations: IS - isomer shift, Δ - quadrupole splitting of doublet components, B_{hf} - the hyperfine magnetic field on ^{57}Fe nuclei of the sextet components, Γ - Lorentz linewidth, α - Gauss fraction, A - area fraction of the given component, product $K_{\mathrm{eff}}V$ - magnetocrystalline anisotropy energy (where V is the volume of nanoparticles and K_{eff} effective magnetocrystalline anisotropy constant).

Sample	Component	IS [mm/s]	Δ [mm/s]	B_{hf} [T]	Γ [mm/s]	α*	A	$K_{\mathrm{eff}}V$ [nm^3.kJ/m^3]
MZF(0.21)	(Fe^{3+})	0.30(2)	-	47.0(3)	0.48(3)	-	0.29(2)	11680(120)
	[Fe^{3+}]	0.36(2)	-	44.7(3)	0.48(3)	-	0.49(2)	
	[Fe^{3+}]	0.36(2)	-	40.0(4)	0.48(3)	-	0.22(2)	
MZF(0.32)	(Fe^{3+})	0.27(2)	-	45.4(4)	0.81(4)	-	0.25(1)	5410(80)
	[Fe^{3+}]	0.36(2)	-	39.8(3)	0.81(4)	-	0.51(1)	
	[Fe^{3+}]	0.36(2)	-	32.0(4)	0.81(4)	-	0.24(1)	
MZF(0.41)	(Fe^{3+})	0.27(2)	0.55(4)	-	0.44(4)	0.00(20)	0.04(1)	4536(fixed)†
	[Fe^{3+}]	0.36(2)	0.56(4)	-	0.44(4)	0.00(24)	0.05(1)	
	[Fe^{3+}]	0.36(2)	0.00(4)	-	2.07(16)	1.00(40)	0.08(1)	
	(Fe^{3+})	0.27(2)	-	45.4(4)	1.10(9)	-	0.20(1)	
	[Fe^{3+}]	0.36(2)	-	41.2(4)	1.10(9)	-	0.40(1)	
	[Fe^{3+}]	0.36(2)	-	28.7(5)	1.10(9)	-	0.23(1)	
MZF(0.54)	(Fe^{3+})	0.27(2)	0.55(3)	-	0.47(3)	0.00(16)	0.11(1)	3600(900)
	[Fe^{3+}]	0.36(2)	0.52(3)	-	0.47(3)	0.00(6)	0.33(2)	
	(Fe^{3+})	0.27(2)	-	45.7(9)	0.48(3)	-	0.14(1)	
	[Fe^{3+}]	0.36(2)	-	31.8(5)	0.48(3)	-	0.21(1)	
	[Fe^{3+}]	0.36(2)	-	10.6(3)	0.48(3)	-	0.21(2)	
MZF(0.63)	(Fe^{3+})	0.27(2)	0.51(3)	-	0.43(3)	0.00(6)	0.17(1)	2000(1100)
	[Fe^{3+}]	0.36(2)	0.52(2)	-	0.43(3)	0.01(3)	0.52(2)	
	(Fe^{3+})	0.27(2)	-	44.3(14)	0.48(3)	-	0.08(1)	
	[Fe^{3+}]	0.36(2)	-	32.8(8)	0.48(3)	-	0.12(1)	
	[Fe^{3+}]	0.36(2)	-	9.5(5)	0.48(3)	-	0.11(1)	

* pseudo-Voigt doublets defined as the sum of a Lorentzian and a Gaussian peak with α weighting parameter which shifts the profile more towards pure Gaussian or pure Lorentzian when approaching 1 or 0, respectively.
† Mössbauer spectrum of MZF(0.41) reaches the limit of the validity of the approximations introduced in development of the many-state superparamagnetic relaxation model.

tributions to the spectra is not possible due to the strong correlation of the fit parameters; nevertheless, the mean angle θ_{m} between the γ-beam and the $\vec{B}_{\mathrm{eff}}$ vector θ_{m}, defined in Section 2.4, determined from in-field Mössbauer spectra, monotonically decreases within the sequence of studied samples from MZF(0.21) to MZF(0.63), in parallel with the increase in zinc content and the decrease in the mean particle size. At the temperature of liquid helium, the cores of the nanoparticles are in a blocked state due to relatively low magnetocrystalline anisotropy and their superspins align along the direction of the applied field ($\theta_{\mathrm{m}} \approx 90°$) while the disordered magnetic moments in the surface layer, which manifests higher magnetocrystalline anisotropy, do not turn completely. With decreasing

Table 4.8: Spectral characteristics determined from the Mössbauer spectra of the MZF samples acquired at liquid helium temperature (4.2 K) in external magnetic field of 6 T. Individual components are designated by parentheses ( ) or [ ] to indicate the tetrahedral or octahedral sites, respectively. Parameter designations: B_{ext} - applied external magnetic field, IS - isomer shift, QS - quadrupole shift, $\bar{B}_{\mathrm{eff}}$ - mean effective hyperfine magnetic field on ^{57}Fe nuclei $B_{\mathrm{eff}} = |\vec{B}_{\mathrm{hf}} - \vec{B}_{\mathrm{ext}}|$ (where $\vec{B}_{\mathrm{hf}}$ is the hyperfine magnetic field) and its distribution width ΔB_{eff}, A - area fraction of the given component, b - ratio of line intensities $I_{2,5}/I_{3,4}$, θ_{m} - mean angle between the γ-beam and the $\vec{B}_{\mathrm{eff}}$ vector.

Sample	Component	IS [mm/s]	QS [mm/s]	$\bar{B}_{\mathrm{eff}}$ [T]	A	b	θ_{m} [°]
MZF(0.21)	$(Fe^{3+})_1$	0.40(3)	0.00(3)	57.6(1)	0.29(2)	3.29(7)	72(1)
	$[Fe^{3+}]_2$	0.50(2)	-0.02(3)	45.3(3)	0.71(2)		
MZF(0.32)	$(Fe^{3+})_1$	0.37(3)	0.00(3)	57.3(2)	0.25(2)	3.29(7)	72(1)
	$[Fe^{3+}]_2$	0.48(2)	0.00(3)	45.3(3)	0.75(2)		
MZF(0.41)	$(Fe^{3+})_1$	0.39(3)	0.01(3)	57.2(2)	0.24(2)	3.15(8)	70(1)
	$[Fe^{3+}]_2$	0.47(2)	0.03(3)	45.4(3)	0.76(2)		
MZF(0.54)	$(Fe^{3+})_1$	0.37(3)	-0.02(3)	56.9(3)	0.24(2)	3.07(8)	69(1)
	$[Fe^{3+}]_2$	0.47(2)	0.02(3)	45.4(3)	0.76(2)		
MZF(0.63)	$(Fe^{3+})_1$	0.37(3)	-0.01(3)	56.6(3)	0.24(2)	2.97(6)	67(1)
	$[Fe^{3+}]_2$	0.47(3)	0.02(3)	45.5(3)	0.76(2)		

particle size, the effect of the surface is enhanced and results in greater deviation of θ_{m}. If the thickness of the magnetically disordered shell is assumed to be 1 nm (estimate based on the lattice constant and observations presented in [P6]), then the Mössbauer results can be related to the mean size of the crystallites listed in table 4.6. The calculated values of b then correspond well to the experimental data even under the simplifying assumption that the thickness of the shell remains constant with decreasing magnetocrystalline anisotropy, which is consistent with the core-shell model.

Nanoparticles of the selected composition MZF(0.41) (intermediate zinc content of $x = 0.41$ in the series) were subjected to a neutron diffraction study at 2 K to confirm the magnetic order and determine magnetic moments of magnetic cations in the tetrahedral and octahedral sublattices (m_{T} = -3.30 μ_{B} and m_{O} = 3.47 μ_{B} per site occupied in a fully stoichiometric spinel system yielding a total magnetic moment of 3.63 μ_{B} per formula unit). In combination with the results of in-field Mössbauer spectroscopy, it is shown that the cation distribution in spinel ferrite nanoparticles can be significantly altered from their bulk counterparts, even for metal cations with a strong preference for particular coordination, such as Zn^{2+}. Assuming the same f-factors for the individual spectral components, the relative amounts of iron in the tetrahedral and octahedral sites were evaluated to 24(2) % and 76(2) %, respectively. The combination of this result with the Rietveld analysis of neutron diffraction data provided the occupancies of 25 % Mn + 28 % Zn + 47 % Fe in the tetrahedral site and 19 % Mn + 6 % Zn + 75 % Fe in the octahedral site.

The formation of a partially inverse spinel structure with $\approx 1/3$ of Zn^{2+} cations located in the octahedral sites can be attributed to hydrothermal preparation at a low temperature of 180 °C, which could have led to a non-equilibrium (metastable) cation distribution. Moreover, the almost random distribution of Mn^{2+} between the two crystallographic sites also suggests a non-equilibrium situation, supported furthermore by the supplemental DFT study.

Similar MZF magnetic cores with narrow size distributions coated in silica and titania appear promising as contrast agents for magnetic resonance imaging (MRI), since they do not show any significant cytotoxic effects and exhibit a high transverse relaxivity of specific temperature dependence. Analysis of relaxometric data in magnetic fields of 0.5 T and 11.75 T indicates that some thermally activated processes that occur in the porous shell of titania-coated particles may lead to an initial enhancement of relaxivity with increasing temperature [P8].

4.3 Mn-Co ferrite nanoparticles

The similarities among the samples of Mn-Co ferrite particles (denoted as MCF) in terms of particle (crystallite) size distribution characteristics allowed the interpretation of the presented results exclusively on the basis of the actual composition, beyond the influence of other structural or morphological parameters. The study [P4] attempts to describe in detail the evolution of magnetic and structural properties with a variable Co/Mn molar ratio in a series of strictly 10 nm oleate-capped (17 wt%) MCF particles. Five samples with an approximate composition of $Mn_{1-x}Co_xFe_2O_4$ ($x = 0.19$–0.77) were prepared using a single-step oleate-based solvothermal method at a rather low temperature of 220 °C [86].

By assuming the absence of anion vacancies, the chemical formula was calculated from inductively coupled plasma optical emission spectroscopy (ICP-OES) spectra, and together with other structural and magnetic characteristics is provided in table 4.9. XRPD confirmed the single-phase character of cubic spinel MCF nanoparticles in the entire composition range. Moreover, a thorough Rietveld refinement led to lattice parameters a in agreement with those determined by single-peak analysis in parallel. The decrease in the lattice parameter with an increase in the Co content was attributed to the smaller effective ionic radius of Co^{2+} compared to high-spin Mn^{2+} [90]. Bright-field TEM micrographs showed well-separated polygonal/spheroidal nanoparticles for all samples, with a mean particle size close to the crystallite size determined by XRPD, and unimodal size

Table 4.9: Structural and magnetic characteristics of the Mn-Co ferrite magnetic nanoparticles. Parameter designations: a - lattice constant, d_X - mean apparent size determined by XRPD or mean particle size determined by TEM, SD - respective standard deviation, M - magnetization.

Designation	Sample	a [Å]	d_{XRPD} [nm]	d_{TEM} [nm]	SD_{TEM} [%]	M @ 300 K, 7 T [Am^2/kg]
MCF(0.19)	$Mn_{0.65}Co_{0.19}Fe_{2.11}O_4$	8.471(1)	10.0(1)	10.3	16	74(2)
MCF(0.31)	$Mn_{0.52}Co_{0.31}Fe_{2.11}O_4$	8.449(2)	10.1(1)	10.9	14	77(2)
MCF(0.59)	$Mn_{0.34}Co_{0.49}Fe_{2.11}O_4$	8.422(1)	9.6(1)	9.7	14	76(2)
MCF(0.66)	$Mn_{0.23}Co_{0.66}Fe_{2.07}O_4$	8.412(1)	9.8(1)	9	13	79(2)
MCF(0.77)	$Mn_{0.13}Co_{0.77}Fe_{2.07}O_4$	8.399(1)	11.6(1)	9.2	14	80(2)

distributions. Magnetic measurements in DC fields using the vibrating sample magnetometer (VSM) showed a single-magnet behavior for all samples. In this time window, the samples already showed superparamagnetic behavior at room temperature, completely different with respect to what was observed by Mössbauer spectroscopy. The shift of the blocking temperature toward higher values with increasing Co/Mn ratio, as observed in the temperature dependencies of magnetization, seems to be defined by magnetic anisotropy in particular.

In the paper [86] published earlier, room-temperature Mössbauer spectra of the MCF samples were recorded by RNDr. Daniel Ňižňanský, Ph.D. of Faculty of Science CUNI. In contrast to magnetic measurement, the particles were observed to be in a blocked state with increasing relaxation effects on the spectra as the Co/Mn ratio decreases. On the basis of the isomer and quadrupole shift values, the absence of Fe^{2+} and cubic symmetry were confirmed. A decrease in the hyperfine magnetic field values was observed with an increase in the Mn content for both octahedral and tetrahedral sites, with a stronger effect for the latter one due to the preference of Mn^{2+} cations for four-fold coordination.

The rationale for the application of in-field Mössbauer spectroscopy and the processing of the acquired spectra follow the procedures described in Section 4.1 with the difference of the software used. Mössbauer spectra acquired at 4.2 K evidence for a long-range ferrimagnetic order for all MCF samples based on change of in-field spectra from those without (not presented here). The in-field spectra (see figure 4.8(right) at the end of the Chapter) resolved two sextets with a distribution of hyperfine fields - the one centered at a hyperfine magnetic field of

Table 4.10: Spectral characteristics determined from the Mössbauer spectra of the MCF samples acquired at liquid helium temperature (4.2 K) in external magnetic field of 6 T. Individual components are designated by parentheses ( ) or [ ] to indicate the tetrahedral or octahedral sites, respectively. The parameter designations: B_{ext} - applied external magnetic field, IS - isomer shift, QS - quadrupole shift, $\bar{B}_{\mathrm{eff}}$ - mean effective hyperfine magnetic field on ^{57}Fe nuclei $B_{\mathrm{eff}} = |\vec{B}_{\mathrm{hf}} - \vec{B}_{\mathrm{ext}}|$ (where $\vec{B}_{\mathrm{hf}}$ is the hyperfine magnetic field) and its distribution width ΔB_{eff}, A - area fraction of the given component, b - ratio of line intensities $I_{2,5}/I_{3,4}$, θ_{m} - mean angle between the γ-beam and the $\vec{B}_{\mathrm{eff}}$ vector.

Sample	Component	IS [mm/s]	QS [mm/s]	$\bar{B}_{\mathrm{eff}}$ [T]	A	b	θ_{m} [°]
MCF(0.19)	$(Fe^{3+})_1$	0.39(3)	-0.02(3)	56.2(3)	34.7(9)	3.1(1)	69.3(7)
	$[Fe^{3+}]_2$	0.49(2)	0.01(3)	46.3(3)	65.3(9)		
MCF(0.31)	$(Fe^{3+})_1$	0.37(2)	-0.01(2)	56.5(2)	33.3(6)	3.22(8)	70.8(4)
	$[Fe^{3+}]_2$	0.49(2)	0.01(2)	47.1(2)	66.7(6)		
MCF(0.59)	$(Fe^{3+})_1$	0.37(2)	0.00(3)	56.1(3)	39.3(7)	3.17(9)	70.1(5)
	$[Fe^{3+}]_2$	0.49(2)	0.01(3)	47.5(3)	60.7(7)		
MCF(0.66)	$(Fe^{3+})_1$	0.37(3)	0.00(3)	56.3(2)	41.2(6)	3.22(9)	70.8(6)
	$[Fe^{3+}]_2$	0.48(2)	0.01(3)	47.8(3)	58.8(6)		
MCF(0.77)	$(Fe^{3+})_1$	0.37(2)	0.00(2)	56.4(2)	41.2(6)	3.0(1)	68.3(7)
	$[Fe^{3+}]_2$	0.48(3)	0.00(2)	48.0(3)	58.8(6)		

56 T with relatively smaller isomer shifts is associated with Fe^{3+} in the tetrahedral sites, while the other centered at a hyperfine magnetic field of 47 T to Fe^{3+} in the octahedral sites. The strong correlation of the individual distributions of effective hyperfine fields did not allow for unambiguous assignment of the spectral intensity at the contact points, as can be seen from the artifacts occurring at the boundaries of distributions in figure 4.8(right). Nevertheless, regardless of the choice of physically reasonable cut-off of effective hyperfine fields during fitation, every fit provided the same area fraction of the given component (i.e., the relative occupancies assuming the same f-factor) and hyperfine parameters within the experimental error. These together with other characteristics of the spectra are listed in table 4.10.

Consistent with room-temperature measurements [86], the mean effective field $\bar{B}_{\mathrm{eff}}$ appears almost constant for Fe^{3+} cations at the tetrahedral sites. For those in the octahedral sites, it systematically increases with increasing cobalt content until a plateau is reached for the two Co-richest samples, indicating a strong correlation of the hyperfine magnetic field on ^{57}Fe resonating nuclei located in the octahedral sites with the magnetocrystalline anisotropy constant, which is related to the cobalt and manganese contents. If the dependence shown in figure 4.7 is fitted by the equation 3.8, the curve approaches a saturation hyperfine field $B_0 \sim 47.9$ T. With increasing manganese content, more symmetric distributions of effective hyperfine fields are observed for the octahedral sites, whereas those for the tetrahedral sites become broader. This again indicates a preference of Mn^{2+} cations for the tetrahedral coordination.

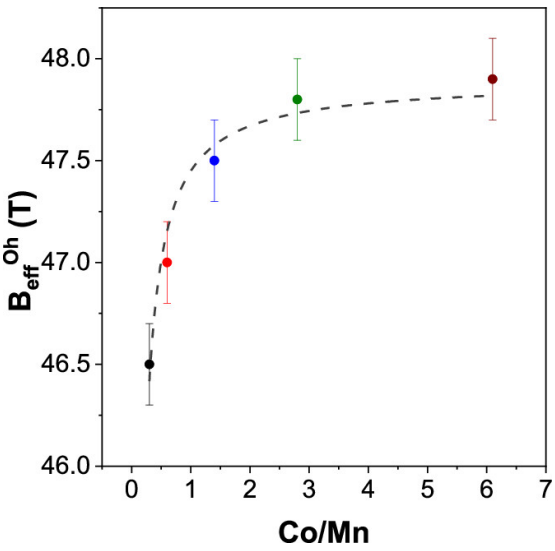

Figure 4.7: Evolution of the mean effective hyperfine field on ^{57}Fe resonating nuclei located in the octahedral (O_{h}) sites as a function of the Co/Mn ratio in the MCF samples. Fit by the equation 3.8 is shown by the dashed line. Adapted from [P4].

The narrow variance of the mean angle between the γ-beam and the $\vec{B}_{\mathrm{eff}}$ vector θ_{m}, defined in Section 2.4, around $\sim 70°$ is in excellent agreement with the similarity in the mean sizes of nanoparticles within the sequence of studied MCF samples, determined by both XRPD and TEM, which is consistent with the core-shell model.

Furthermore, the Co^{2+} and Mn^{2+} cation distributions were hypothesized based on the Co, Mn, and Fe contents of ICP-OES, saturation magnetization, magnetocrystalline anisotropy constant values along with the inversion degree obtained by Mössbauer spectroscopy. According to the Néel model, which accounts for the existence of two magnetic sublattices in cubic ferrites, and assuming no vacancies in the structure, the values revealed some general trends as a function of the MCF composition. In particular, samples can be distinguished into two groups: (i) those with a manganese content up to about 40 % of total divalent cations, characterized by Mn^{2+} ions equally distributed in both tetrahedral and octahedral sites, and Co^{2+} present only in the octahedral sites, and (ii) Co-richer samples having all Mn^{2+} cations in the octahedral sites (see Supplementary information of [P4]).

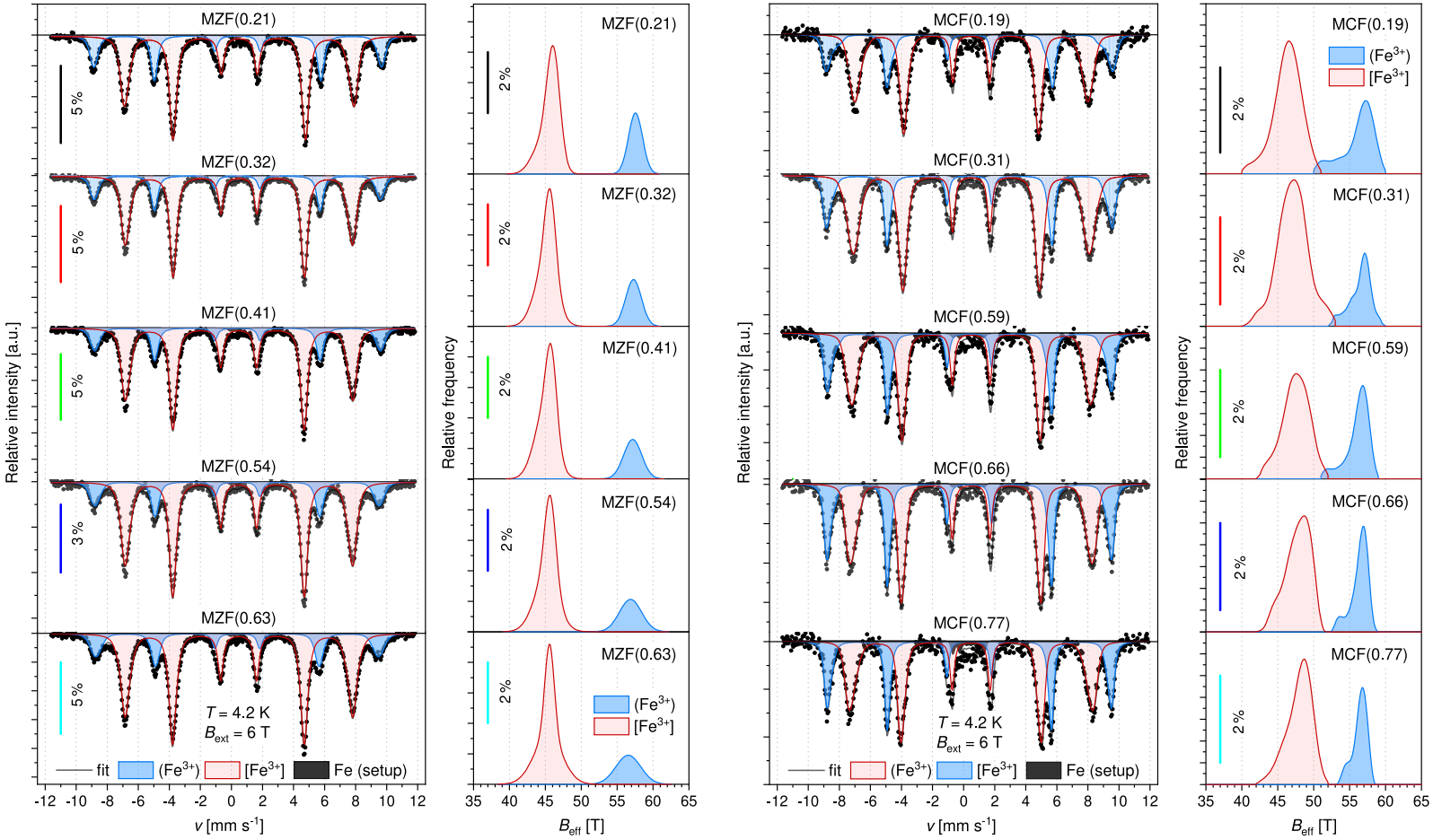

Figure 4.8: Mössbauer spectra of the MZF and MCF magnetic nanoparticles acquired at liquid helium temperature (4.2 K) in an external magnetic field of 6 T with distributions of effective hyperfine magnetic field $B_{\mathrm{eff}} = |B_{\mathrm{hf}} - B_{\mathrm{ext}}|$. The blue component represents Fe^{3+} in the tetrahedral sublattice, and the red component Fe^{3+} in the octahedral sublattice. The minor doublet represents a parasitic signal originating from the experimental setup. The vertical bars scale the observed Mössbauer effect.

5. Magnetic particle spectroscopy

5.1 Fundamental principles

Magnetic particle imaging (MPI) introduced in 2005 [92] is an emerging noninvasive tomographic method based on the nonlinear response of superparamagnetic tracers to a sinusoidal AC magnetic field. The technique is gaining an increasing interest for direct anatomical imaging among the well-established alternatives - nuclear magnetic resonance (MRI), X-rays (CT), or ultrasound (sonography) - since the method has been speculated to greatly improve spatial and temporal resolution (i.e. sensitivity). Moreover, MPI does not require any ionizing radiation and relies only on the presence of superparamagnetic tracers and the application of an external magnetic field. Due to much faster response compared to MRI, MPI is able to monitor the flow of blood in the body in real time, however, it needs to be complemented by anatomical information from other imaging techniques as solely the spatial distribution of the tracer is detected.

The time-dependent response of the nanoparticle superspin to the varying magnetic field and respective magnetic particle spectrum obtained by Fourier transformation of the detected signal consist of odd higher harmonics of the drive field frequency and is governed by two fundamental mechanisms, whose relative contributions vary significantly depending on the tracer properties. In case of pure Brownian (Debye) process [93], the entire particle rotates with respect to the fluid while the magnetic dipole moment remains fixed with respect to the crystalline lattice. The corresponding Brownian relaxation time is

$$\tau_{\mathrm{B0}} = \frac{3\eta V_{\mathrm{h}}}{k_{\mathrm{B}}T}, \tag{5.1}$$

where η is the viscosity of the fluid surrounding the particle and V_{h} is its hydrodynamic volume. For a pure Néel process [94], the magnetic dipole moment within the particle rotates with respect to the crystalline lattice (internal relaxation). Respective relaxation time is given by

$$\tau_{\mathrm{N0}} = \frac{\sqrt{\pi}\beta(1+\alpha'^2)M_{\mathrm{s}}}{4\gamma\alpha'(\beta K)^{3/2}} e^{\beta K}, \tag{5.2}$$

where M_{s} is the saturation magnetization, $\beta = V_{\mathrm{c}}/(k_{\mathrm{B}}T)$, V_{c} is the core volume, K is the anisotropy constant, α' is the damping constant, and γ is the electron gyromagnetic ratio. The combination of both processes in real systems of nanoparticles is described by the effective relaxation time [95, 96] that is also applicable for non-zero-field relaxation times, i.e.,

$$\tau = \frac{\tau_{\mathrm{B}}\tau_{\mathrm{N}}}{\tau_{\mathrm{B}} + \tau_{\mathrm{N}}}. \tag{5.3}$$

In addition to the technical properties of the actual MPI scanner, resolution of the MPI strongly depends on the tracers used. Therefore, the main experimental challenge still lies in optimizing the nanoparticle properties to shape their non-linear magnetization response. Since MPI is extremely sensitive to the particle magnetic moment, relaxation characteristics, superparamagnetic behavior at

scanning frequencies, and particle mobility in the suspension, the applicability of magnetic particles in MPI is closely linked to the structure and magnetic properties of magnetic cores, core size, and particle coating. According to the Langevin theory, MPI resolution should improve significantly with increasing nanoparticle size [97, 98], which in turn also affects relaxation mechanisms and may lead to signal reduction due to phase lag at working frequencies [99] or limitations in the drive field [100].

Magnetic particle spectroscopy (MPS) [101, 102], also interpreted as zero-dimensional MPI scanner, was primarily designed to assess the properties of potential MPI tracers [103] but proved to be extremely useful for direct insight into Néel and Brownian relaxations. An important parameter of magnetic nanoparticles with respect to MPI use is the amplitude ratio of the fifth over the third harmonics R53 due to its dependence on the frequency of the drive field. The harmonics ratio R53 reflects both the static characteristics of the samples (the Langevin dependence of equilibrium magnetization on the applied field) and the effects of Brownian and Néel types of relaxation with their complex dependence on the instantaneous value of the oscillating magnetic field.

5.2 Experimental equipment

To test the response of nanoparticle suspensions to an alternating magnetic field, a functional MPS single excitation field setup was constructed as part of the dissertation thesis. The current apparatus used in the Laboratory of Mössbauer spectroscopy is shown in figure 5.1 and offers a range of external parameters summarized in table 5.1.

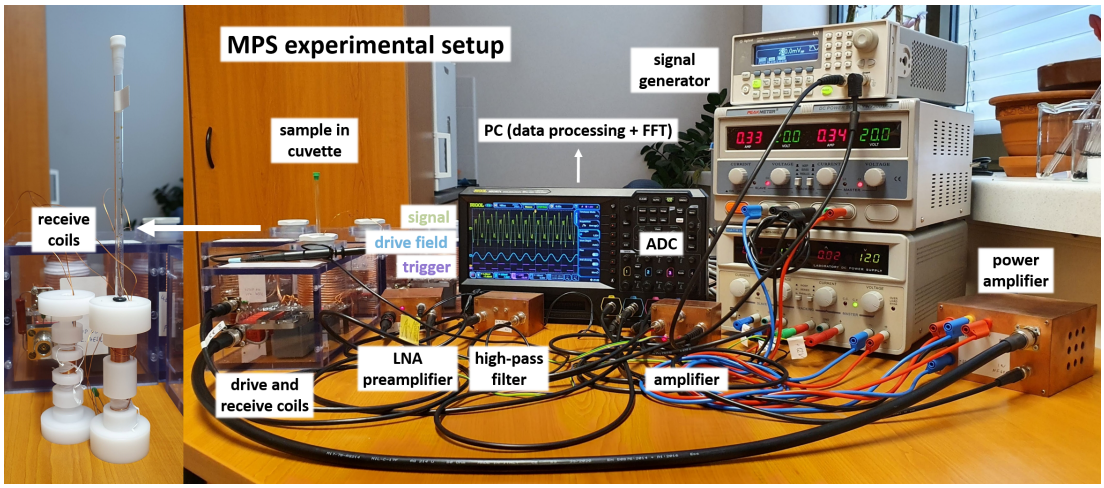

Figure 5.1: Photography of the constructed MPS single excitation field setup during operation.

The flow diagram of the constucted MPS setup is shown in figure 5.2. The excitation coils are made of litz wire (Elektrisola OSP18 natur, 0.00491 Ohm/m) woven from 480×100µm single wires, wound on a delrin bore of 40 mm diameter with a total height of 80 mm and 23 turns per layer. The coils are tuned and impedance-matched to frequencies of ∼ 10, 15, 25, 35, and 50 kHz, oscillating purely sinusoidal with a magnetic induction of up to 20 mT. The drive field fre-

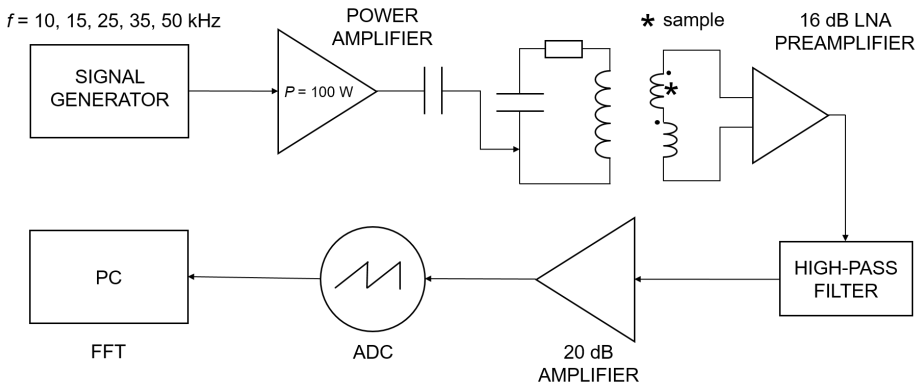

Figure 5.2: Flow diagram of the constructed MPS single-excitation field setup adapted from [P1].

quencies and field strength limitations were selected to roughly correspond to preclinical MPI scanners used for imaging of animal models in order to have another point of reference and to increase the applicability of the developed apparatus. The investigated suspension of magnetic nanoparticles with a known concentration and volume of $\sim$ 100 µL is carefully pippeted in an NMR cuvette of 5 mm diameter placed in the center of the excitation coils to ensure maximum homogeneity of the magnetic field that affects the magnetization of the particles, as discussed later in the text. The magnetic induction in place of the imaging volume is maintained by a 100 Watt power amplifier. Inside the field-generating coils, a receiver coil is placed near the imaging volume to maximize the sensitivity. To substantially increase the Q-factor of the resonating circuit, wherever it was technically possible, the metallic materials were not placed in the vicinity of the coils.

To reduce the dynamic range of the signal induced by the nanoparticles in the receiver coil and to increase SNR, we have designed MPS setup that combines both filtering and cancellation method adapted from [104]. Contrary to this reference, the sinusoidal magnetic field (drive field) which couples into the receiver coil is filtered by an analog high-pass (low-stop) filter that suppresses a signal at all frequencies below the second harmonics, specifically designed for each excitation

Table 5.1: Summary of MPS setup parameters and other characteristics.

Power amplifier	100 W, 18–100 kHz				
Drive field	0-16 mT				
f	10.156 kHz	14.975 kHz	24.990 kHz	34.555 kHz	50.390 kHz
Δf (FWHM)	140 Hz	200 Hz	315 Hz	400 Hz	360 Hz
U_{pp}	150 V	185 V	240 V	275 V	300 V
high-pass filter attenuation (1^{st} harmonics)	53 dB	57 dB	60 dB	60 dB	55 dB
Litz wire layers	3	3	3	2	2
LNA preamplifier	16 dB				
Amplifier	20 dB				

coil. All higher harmonics of the excitation frequency should pass through the filter without attenuation. To detect the particle magnetization, a gradiometer receiver coil, described later in the text, is used, in which the temporal change of the magnetization is induced as a voltage signal. The induced voltage in the receiver coil is amplified by a 16 dB low-noise amplifier (LNA) to adjust the signal into the 8-bit input range of the ADC Rigol oscilloscope just after passing the high-pass filter and linear 20 dB amplifier, where the signals are digitized with a sampling rate of 10 Msps. The quality is further enhanced by averaging over 1024 sets of 1 µs samples. The resulting time-dependent signal is preprocessed and transformed into the frequency domain by using the fast Fourier transform (FFT) algorithm (the script might be found in Attachments), which allows one to deduce the amplitudes of higher harmonics of the drive field frequency and also the amplitude ratio of the fifth (f_5) and third (f_3) harmonics (R53 parameter).

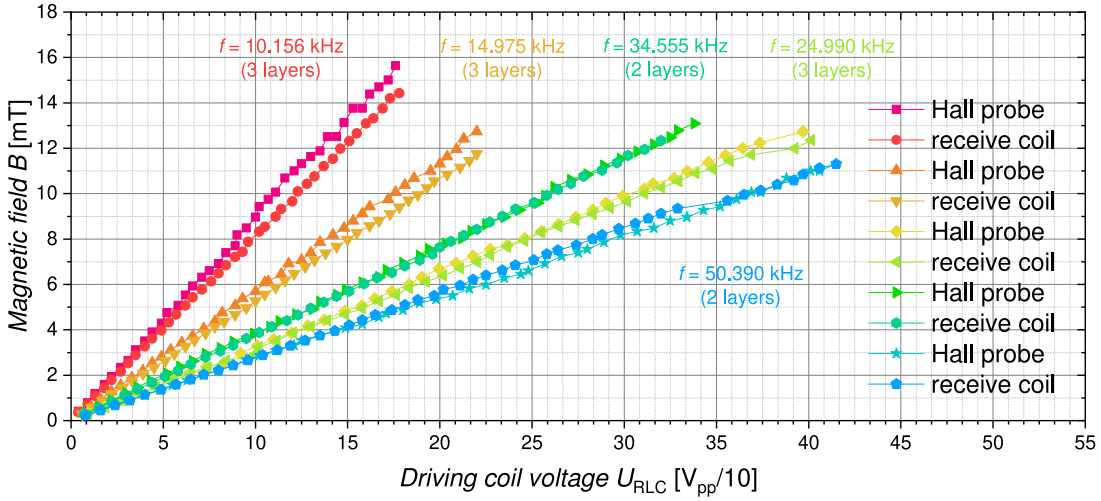

Figure 5.3: Calibration curves of the excitation coils - dependence of magnetic induction amplitude on the voltage on the Hall probe and in the circuit of receiver coil (0.5 mm, 18 turns).

To find a relation between variable excitation coil voltage and magnetic induction in the center of the excitation coils, a Hall probe and for-the-purpose designed receiver coil (a copper wire of 0.5 mm diameter around 10-millimeter bore, 18 turns) were employed. SS49E Hall probe by Honeywell (with a frequency range up to 50 kHz) was calibrated using two permanent reference magnets with magnetic inductions of ±20.3 mT and ±51.1 mT by MAGMESS. The magnetic field, detected by the Hall probe, is given by the relation $B = (U_{\mathrm{Hall}}{+}2596) \times 0.071(2) - 185(5)$, where U_{Hall} is the voltage induced across the probe. The voltage induced on the contacts of the receiver coil is related to the magnetic field strength by

$$B = \frac{U}{2n\pi^2 r_{\mathrm{c}}^2 f}, \tag{5.4}$$

where n is the number of turns, r_{c} the radius of the receiver coil (assuming finite dimensions of the wire), and f is the frequency of the driving field. The respective calibration curves measured up to a maximum voltage, provided by the power

Table 5.2: Linear regression coefficients of the excitation coils calibration curves.

	$B=a+b\times U_{\mathrm{RLC}}$				$U_{\mathrm{RLC}}=c+d\times B$	
	Hall probe		receiver coil		receiver coil	
f [khz]	a	b [10 mT/V_{pp}]	a	b [10 mT/V_{pp}]	c	d [10 mT/V_{pp}]
10	-0.01115	1.124672	0.001375	1.227203	-0.000048	0.814743
15	0.02159	1.741085	0.054871	1.877684	-0.02837	0.532496
25	0.076771	3.039231	0.022601	3.141774	0.000804	0.317888
35	-0.07835	2.600442	0.140938	2.593127	-0.05249	0.38552
50	-0.18614	3.713041	-0.22111	3.622039	0.069785	0.275659

source, are shown in figure 5.3 and the linear regression coefficients are given in table 5.2. It should be noted that the litz wire of high-frequency excitation coils (> 30 kHz) is wound in two layers instead of three, which leads to a relatively less steep slope of the calibration curves. At the same time, the nonlinear behavior of the probe starts to appear above the frequency of 30 kHz according to the SS49E datasheet, so the relation 5.4 is better suited for setting the magnetic field at higher frequencies.

Due to the finite dimensions of the excitation coils, the amplitude of the axially symmetric magnetic field inside the coils is expected to vary along the axis and, by extension, the sample volume. The height of the coil was designed so as to ensure a sufficient homogeneity of the field in this region so that the sample height might reach up to 10 mm. The field variance was tested using the above-mentioned receiver coil with the driving voltage set to generate a field close to 9 mT in the center of the coils. As can be seen in figure 5.4, the field in the experimental volume can be considered homogeneous. The shift of the sample position or an increase of the experimental volume about 10 mm would lead to a 0.5 mT offset in the amplitude of the field compared to the center.

A gradiometer receiver coil is constructed as a Helmholtz coil pair located in the excitation coil - a receiver coil surrounding the imaging volume filled with suspension of magnetic particles, and another, identical cancelling coil with an

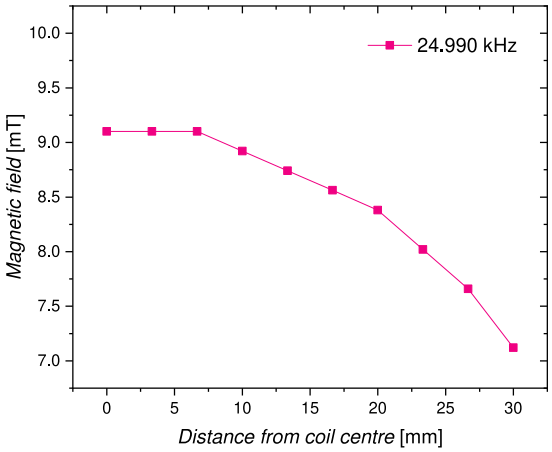

Figure 5.4: Spatial dependence of the magnetic field amplitude along the axis of excitation coils. The connecting lines are meant to only guide the eye.

opposite winding direction further away from the imaging volume. This construction is effective as the particle signal in the receiver coil is much stronger than in the cancellation coil while all field components that couple in both coils in the same way (mostly the first harmonics frequency) are cancelled out [104]. Optimization of the thickness of the receiver coil wire to provide the best SNR with respect to the geometric restrictions of the excitation coils was based on the SNR calculation script, described in Section 5.3. This was carried out by student Matyáš Rozprým working on his student faculty grant "*Optimization of the receive coil for magnetic particle spectroscopy*" who constructed and tested three variations of coil winding from a single copper wire of 0.16 (n=46, 0.89 Ohm/m), 0.3 (n=27) and 0.5 mm (n=20). The hollow delrin bore has a diameter of 10 mm and coils' height is around 10 mm. The measured signal of the Resovist® sample [55] (for structural and magnetic characteristics, see table 6.1) at the magnetic fields of 10 and 12 mT in the excitation coil for every frequency was processed using the script described in Chapter 5.3 (also see Attachments). In all cases, the receiver coil with 0.16-millimeter wire showed 2-3 times better performance compared to a 0.5-millimeter wire coil, and a 0.3-millimeter wire coil 1.5 times the advantage over the same 0.5-millimeter wire coil.

Because of the significant resistivity of the wire used in the winding, the excitation coils tend to heat the experimental volume over the time of operation at higher amplitudes of the drive field, manifested in a gradual linear change of the amplitude and phase of higher harmonics of the studied suspensions of nanoparticles. In figure 5.5, the order of magnitude of the parameter evolution during a typical MPS experiment of a batch of samples is demonstrated. It should be noted that each measurement takes about 10 seconds and the mean background signal measured without a sample is subtracted from the real signal to reduce the effect of temperature fluctuation and to further decrease parasitic signals induced by the drive (see Section 5.3 for reference). After 25 minutes, the relative change in the R53 ratio and, hence, the phase difference is ~ 3 %.

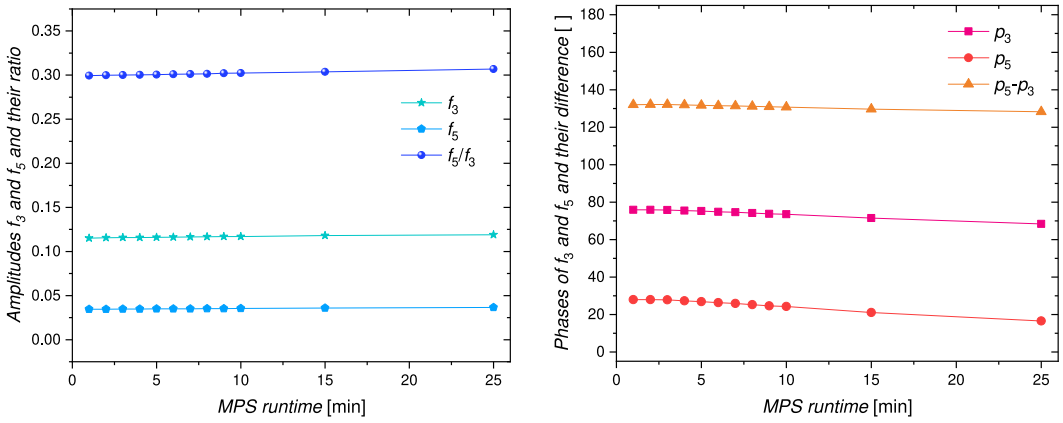

Figure 5.5: MPS spectral parameters of the Resovist® signal obtained in a 25.31 kHz excitation coil with a magnetic field of 9.1 mT. The connecting lines are meant to only guide the eye.

5.3 Computational methods

The current version of the MPS data processing script is implemented in the latest Wolfram Mathematica 13.3 release. The script was developed with the intention of providing an interface between the oscilloscope and the output required by the end user (scientist). In addition to signal preprocessing and user-friendly data reporting, the script implements the subtraction of the mean background signal from the actual measurement according to [104] (in the reference denoted as air measurement, taken before and after signal acquisition), parameterized FFT, a routine for peak detection and labeling, signal truncation based on SNR calculation (as described later in the chapter), and respective deliverable calculation (peak position and intensity, R35 and its inverse, phase shift with respect to the drive field, etc.). The complete script can be found in Attachments.

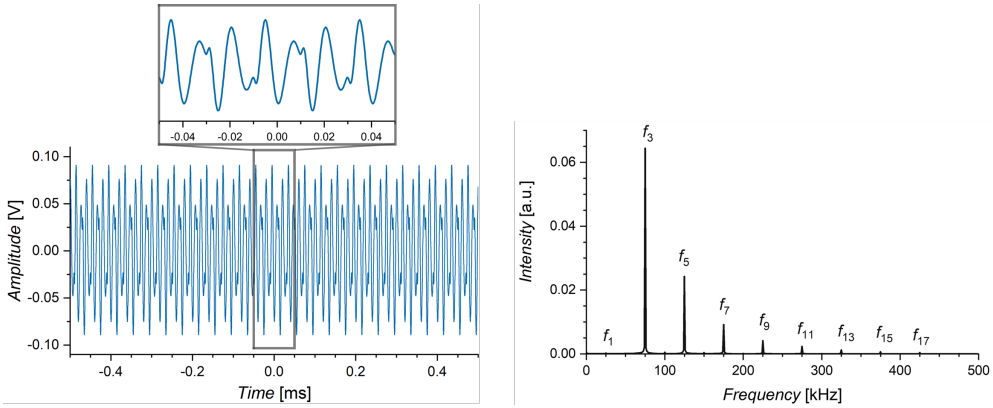

Figure 5.6: Typical time and frequency domains of the signal recorded by the constructed MPS single-excitation field setup with a drive field frequency of ~ 25 kHz and an amplitude of 13 mT. Adapted from [P1].

The idea of peak detection lies in finding a significant variation of the signal from the noise. The FFT signal integrated over the frequency domain is automatically distributed in the histogram bins according to the Freedman-Diaconis rule. As a first approximation, the histogram is fitted by the lognormal distribution function to detect the background level given by the mode of distribution. Around this value, a symmetric distribution is inscribed to fit the 'background only' data and standard deviation of this Gaussian-like distribution, $\sigma = \mathrm{FWHM}/2\sqrt{2\ln 2}$, is calculated. To accept the peak as distinguishable, its intensity must be above the $m + \sigma$ threshold (where m is the mean noise value coinciding with the mentioned mode), and the peak frequency must be placed close to the multiple of frequency of the drive field. The SNR for each harmonics is simply given as the peak magnitude divided by this standard deviation (SD) of the noise.

5.4 Simulation of the magnetization response

The computer simulation of the response of the system of uniaxial single-domain non-interacting magnetic nanoparticles (model of dilute ferrofluid) to an oscillating external magnetic field $\vec{B}(t)$ might provide a deeper insight into the relaxation mechanisms behind the spectral characteristics of the experimentally observed

```
{bins, counts} = HistogramList[fftdata[[1 ;; 5000, 2]], "FreedmanDiaconis"];
centers = MovingAverage[bins1, 2];
model = s / (σ * x * Sqrt[2 * Pi]) * E^(-((Log[x] - μ)^2 / (2 * σ^2)));
pars = FindFit[{centers, counts}^T, model, {{μ, μ_start}, {s, s_start}, {σ, σ_start}}, x]
Show[Histogram[fftdata[[1 ;; 5000, 2]], "FreedmanDiaconis"],
 Plot[model /. pars // Evaluate, {x, 0, fourier[[1, 2]] * 200000}]]
mode = E^(μ - σ^2) /. pars // Evaluate;
f[x] = model /. pars;
RS = f[x] /. x → mode;
y = x /. FindRoot[f[x] == RS / 2, {x, 0.001, mode}];
FWHM = 2 * Abs[y - mode];
Print["max = ", RS, " at ", mode]
Print["FWHM = ", FWHM]
```

Figure 5.7: Script for the peak detection of higher harmonics from the MPS signal.

MPS signal. In the adiabatic limit of a slowly varying field ($\tau \ll 1/f$), the behavior of the system can be understood on the basis of the Langevin function [105], while for longer relaxation times $\sim$ µs, the Fokker-Planck equation (FPE) [106] must be considered. In principle, in any system both the Brownian and Néel mechanisms can influence the field-responding magnetization $\vec{M}(t)$ of nanoparticle ferrofluids. The simple weighted product given by equation 5.3, that assumes that the Brownian and Néel processes are decoupled, is commonly used in MPI and MPS to treat such relaxation even though they are coupled. Here, τ_{B} and τ_{N} are zero-field relaxation times despite the fact that the field is non-zero and the Néel relaxation time decreases much more rapidly than the Brownian relaxation time with increasing field strength [107]. However, treating the coupling properly is difficult [108] and thus often overlooked.

To model the pure Brown or Néel relaxation process accordingly, one must numerically solve FPE given by relation 5.5, which represents a set of coupled partial differential equations. Based on the information and approaches used in references [107, 109, 110], a script that can be found in Attachments was developed under the roof of the MathWorks Matlab R2023b platform. The system can be described as 'stiff' because the limit cycle has portions where the solution components change slowly, alternating with regions of very sharp change. Therefore, the 'ode15s' ordinary differential equation integration routine (so-called solver) [111] was employed which proved to be an appropriate choice. The script offers the options provided similarly in [107] to model the magnetization response to a step function magnetic field, sinusoidal, or linearly ramped field. Thus,

$$\begin{cases} 2\tau_{\mathrm{B0}} \dfrac{\partial W}{\partial t} = \dfrac{\partial}{\partial x}\left[(1-x^2)\left(\dfrac{\partial W}{\partial x} - \alpha(t) W\right)\right] \text{ for Brown relaxation,} \\ 2\tau_{\mathrm{N}^*} \dfrac{\partial W}{\partial t} = \dfrac{\partial}{\partial x}\left[(1-x^2)\left(\dfrac{\partial W}{\partial x} - \alpha(t) W - \alpha_{\mathrm{K}} x W\right)\right] \text{ for Néel relaxation,} \end{cases} \tag{5.5}$$

where $W(x,t)$ is a normalized distribution of dipole-moment orientations x in time t, the parameters α can be expressed by the properties of the system as

$$\begin{aligned}\alpha(t) &\equiv \frac{m_0}{k_\mathrm{B}T}B(t) = \frac{M_\mathrm{s}V_\mathrm{c}}{k_\mathrm{B}T}B(t),\\ \alpha_\mathrm{K} &\equiv 2K_\mathrm{eff}\beta = \frac{2K_\mathrm{eff}V_\mathrm{c}}{k_\mathrm{B}T},\end{aligned} \tag{5.6}$$

and τ_{N^*} is connected with $\tau_{\mathrm{N}0}$ via

$$\tau_{\mathrm{N}0} = \frac{\sqrt{\pi}}{2}\tau_{\mathrm{N}^*}\frac{e^{\beta K}}{(\beta K)^{3/2}}. \tag{5.7}$$

To numerically solve FPE, $W(x,t)$ is expanded in terms of Legendre polynomials $P_n(x)$ with weights $a_n(t)$, i.e.,

$$W(x,t) = \sum_{n=0}^{\infty} a_n(t)P_n(x), \qquad a_0(t) = 1/2, \tag{5.8}$$

where x is a direction cosine of the polar angle between the particle moment and the vector of the external magnetic field (in direction $\vec{e}_\mathrm{B}$). Equation 5.8 is consequently substituted into the equation 5.5 that leads to the set of coupled ordinary differential equations for $a_n(t)$, i.e.,

$$\begin{aligned}\frac{2\tau_{\mathrm{B}0}}{n(n+1)}\frac{da_n}{dt} &= -a_n + \alpha(t)\left[\frac{a_{n-1}}{2n-1} - \frac{a_{n+1}}{2n+3}\right],\\ \frac{2\tau_{\mathrm{N}^*}}{n(n+1)}\frac{da_n}{dt} &= -a_n + \alpha(t)\left[\frac{a_{n-1}}{2n-1} - \frac{a_{n+1}}{2n+3}\right] +\\ &\quad \alpha_\mathrm{K}\left[\frac{(n-1)a_{n-2}}{(2n-3)(2n-1)} + \frac{na_n}{(2n-1)(2n+1)} - \right.\\ &\quad \left.\frac{(n+1)a_n}{(2n+1)(2n+3)} - \frac{(n+2)a_{n+2}}{(2n+3)(2n+5)}\right].\end{aligned} \tag{5.9}$$

Once $W(x,t)$ for a given system is known, the magnetization is calculated as $\vec{M}(t) = nm_0\langle x(t)\rangle\vec{e}_\mathrm{B}$, with n being the nanoparticle number density and $\langle x(t)\rangle = \int_{-1}^{1} xW(x,t)\,dx$, and might be transformed to frequency-domain by FFT to determined respective spectral parameters. To count in all the dominant contributions to $W(x,t)$, at least 30 or 50 terms of the matrix (defined by equations 5.9) for the Brown or Néel relaxation, respectively, must be taken into account. The initial (boundary) conditions are chosen to allow fast convergence to a steady solution. The field-dependent Néel relaxation time is calculated by the following relation developed by Brown [94], i.e.,

$$\tau_\mathrm{N} = \sqrt{\pi}\left(\frac{\alpha_\mathrm{K}}{2}\right)^{-3/2}\frac{\tau_{\mathrm{N}0}}{(1-h^2)}[(1+h)e^{\frac{\alpha_\mathrm{K}}{2}(1+h)^2} + (1-h)e^{\frac{\alpha_\mathrm{K}}{2}(1-h)^2}]^{-1}, \tag{5.10}$$

where $h = \alpha/\alpha_\mathrm{K}$.

To illustrate the script performance, we simulated a system of Néel relaxating 20-nanometer particles with parameters similar to [109] (i.e., *pdi*=0.13, T=300 K, η=1.0049 mPa s, K_eff=20000 J/m^3, M_s=474000 J/m^{3}T, damping α'=0.1)

and let the solution of FPE evolve for a sufficiently long time to obtain steady oscillations of the $a_n(t)$ coefficients in harmony with sinusoidally varying magnetic field (f=10, 100 kHz). The time evolution for 15 mT field, oscillating with a frequency of 100 kHz (limit case of fast oscillating strong field), is presented in figures 5.8 and 5.9.

To develop the code further, we assumed the lognormal distribution of particle sizes, which translates also to the distribution of hydrodynamic sizes and magnitudes of magnetic moments. However, shortly after some testing, it be-

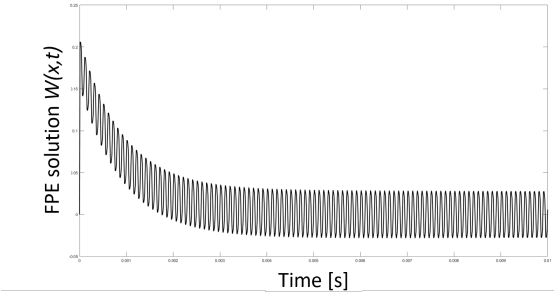

Figure 5.8: Time evolution of FPE solution $W(x,t)$ for 20-nanometer nanoparticles in a sinusoidal drive field of 15 mT, oscillating with a frequency of 100 kHz, let to evolve for 10 ms to reach steady state.

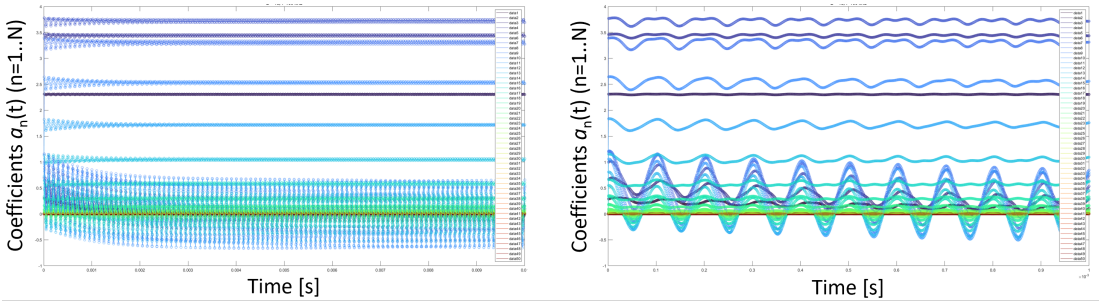

Figure 5.9: (Left) 10 ms time evolution of the $a_n(t)$ (n=1..50) coefficients computed for a sinusoidal drive field of 15 mT, oscillating with a frequency of 100 kHz, (right) zoom of the first millisecond, where the initial boundary conditions still play a role in the time evolution of the $a_n(t)$ coefficients.

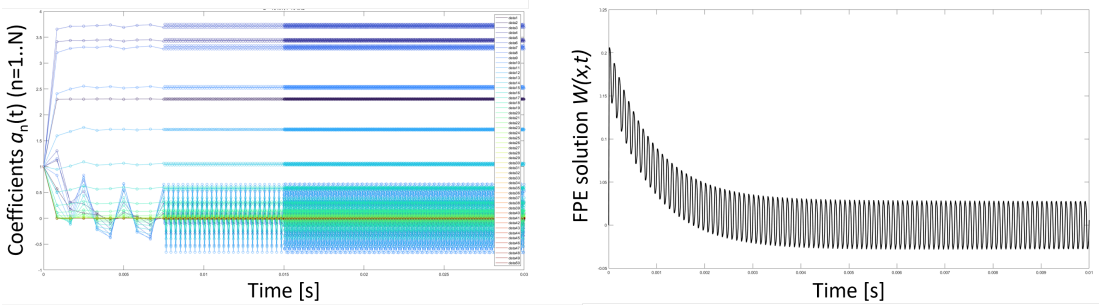

Figure 5.10: (Left) time evolution of the $a_n(t)$ coefficients for the same nanoparticle system after optimization of the sampling space that led to higher computational efficiency, (right) time evolution of FPE solution $W(x,t)$ for the same nanoparticle system.

came obvious that for the fraction of relatively large particles (> 100 nm), the simulation did not converge and the choice of the authors to simulate unimodal 10-nanometer spherical particles of the same hydrodynamic size became clear. Several modifications of the code to simulate real systems of nanoparticle suspensions that are interesting from the MPI point of view are suggested later, but these are not the purpose of the submitted thesis. We plan to implement them in the future. On the other hand, a simple resampling of the time vector (in the code provided in Attachments, look for the parameter 'tspan' that defines boundaries and spacing), so that for initial stages of solution development with time the sampling is rather sparse, increases computational efficiency by focusing the resources on the region of a steady run, as is demonstrated in figure 5.10. The next logical step would be to implement automation of the matrix size limit (determination of maximal n needed) and the estimation of initial boundary conditions that play a key role in simulation time.

6. Magnetic particle spectroscopy of real systems

6.1 Systems of real nanoparticles

Suspensions of particles with various chemical composition, morphologies, and magnetic properties were synthesized at the Institute of Physics CAS by the team of Ing. Mgr. Ondřej Kaman, Ph.D. The samples are described in detail in the publications referenced in table 6.1 summarizing their overall characteristics. Multiple series of ferrite-based magnetic cores with several types of surface modification synthesized by thermal decomposition (td) [87], or under solvothermal (s) or hydrothermal (h) conditions were chosen for the MPS experiment. Their performance was compared to the commercially available Resovist® product (0.5 mmol(Fe)/mL) [55], widely used as a golden-standard reference in the MPI- and MPS-related literature [103] due to having a high r_2/r_1 relaxivity ratio and being a very accessible SPION model.

The encapsulation of the nanoparticles prepared by thermal decomposition in reverse microemulsion [113] led to individually coated ferrite particles. On the contrary, the encapsulation procedure applied to the hydrothermally/solvothermally prepared nanoparticles provided silica-coated clusters as can be seen in

Table 6.1: Characteristics of the magnetic cores for further encapsulated for MPS experiments. Parameter designations: a - lattice constant, d_X - mean apparent size determined by XRPD or mean particle size determined by TEM, SD - respective standard deviation, M - magnetization.

Identification	Designation	Composition	Synthesis	a [Å]	d_{XRPD} [nm]	d_{TEM} [nm]	SD_{TEM} [nm]	M @ 300 K, 3 T [Am^2/kg]
A101	CF-td	$Co_{0.68}Fe_{2.30}O_4$	thermal dec.	8.3886(1)	16	12	4	67.6
A133	CF-h	$Co_{1.06}Fe_{1.94}O_4$	hydrothermal	8.3735(2)	8	-	-	59.0
A128	ZF-td	$Zn_{0.34}Fe_{2.51}O_4$	thermal dec.	8.3946(1)	12	11	4	71.8
A136	ZF-s(@cit)	$Zn_{0.32}Fe_{2.52}O_4$	solvothermal	8.4075(2)	12	13	3	80.5
Resovist®	Resovist	Fe_2O_3/Fe_3O_4	NA	8.359(3) [112]	9.9 [112]	4.2	NA	94.4

Table 6.2: Properties of silica-coated and citrate-stabilized nanoparticles for MPS experiments. Parameter designations: SD - standard deviation, $d_{Z,DLS}$ - Z-average hydrodynamic size determined by DLS, pdi_{DLS} - respective polydispersity index.

Designation	Surface modification	Mean shell thickness from TEM [nm]	SD_{TEM} [nm]	$d_{Z,DLS}$ [nm]	pdi_{DLS}	Further parameters
CF-td@sil	silica	6	1	129	0.16	silica-coated clusters of particles
CF-h@sil	silica	6	1	97	0.17	silica-coated individual particles
ZF-td@sil	silica	6.4	0.8	124	0.14	silica-coated individual particles
ZF-td@sil-agg	silica	4.8	0.7	142	0.36	silica-coated clusters of particles
ZF-s@cit	citrate	monolayer	NA	110	0.35	
ZF-s@sil	silica	5	1	114	0.14	silica-coated individual particles
ZF-s@sil-t	silica	17	2	128	0.22	
Resovist	carboxydextran	R_{min}=19 - R_{max}=186	NA	62	NA	carboxydextran-coated clusters

figure 6.1, the fine fraction of which was isolated by mass fractionation. The structural properties of these particles are summarized in table 6.2. All suspensions prepared from these magnetic nanoparticles were adjusted to the same weight concentration of magnetic cores of 15.2 mg/g (corresponding to a molar concentration of metal ions of 0.191–0.195 mol(Me)/L), and the sample volume used for MPS experiments was 100 µL.

To model the influence of the environment of various viscosities on the relaxation mechanisms of particle magnetic moments in an oscillating external magnetic field of various amplitudes and frequencies, two series of zinc ferrite cores prepared by thermal decomposition and encapsulated in a thin layer of silica by reverse microemulsion method, dispersed in suspensions with changing glycerol-water ratios, were prepared by rigorous weighting of purified water, high-purity glycerol, and particle suspensions of concentrations determined a priori. Individual silica-coated particles ('K' series) showed better performance compared to silica-coated clusters of particles ('U' series).

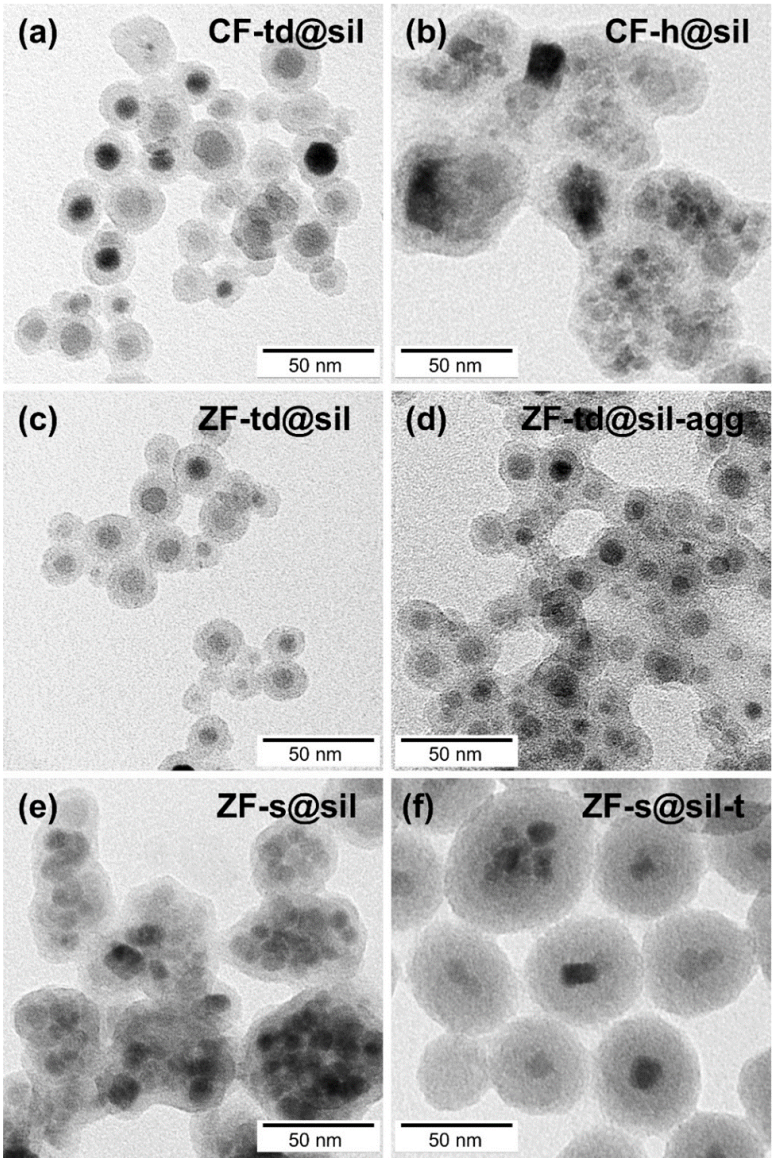

Figure 6.1: TEM micrographs of silica-coated ZF and CF products. Adapted from [P1].

6.2 Results of magnetic particle spectroscopy

For the MPS experiments presented in this thesis, the most recent version of the MPS apparatus described in Section 5.2 was employed. The script used to process the raw output data is presented in Section 5.3. Each sample, stored in the refrigerator, was allowed to thermally equilibrate under ambient conditions, gently centrifuged (< 5000 rpm), and ultrasonicated (~ 2 min) before measurement. Detailed magnetic field dependencies at two various frequencies of the oscillating field, ~ 10 and 25 kHz, are shown in figures 6.3 and 6.4 to demonstrate how the design of the magnetic core, surface layer, and concentration of the particles in suspension manifest themselves in the experimentally observed spectral parameters. Details of the samples can be found in tables 6.1 and 6.2. The amplitudes of the higher harmonics, given only in arbitrary units, are strictly recalculated to equal molar amounts of metal cations in suspensions of magnetic nanoparticles based on the real mass of the sample and the actual chemical formula. Strong variations in spectral parameters at small drive fields of ≤ 3 mT, where the relative error of the method increases rapidly, justify the use of working fields above ~ 6 mT in the so-called 'linear' region when comparing various MPS devices and nanoparticle systems found in the literature. Some of the original results presented here were recently published in [P1].

Up to 23 higher harmonics could be discerned in a MPS signal of particles measured in a magnetic field of 13 mT, oscillating with frequency of ~ 25 kHz. If shown on a logarithmic scale (see figure 6.2(left)), the amplitudes of higher harmonics are decreasing nearly linearly with frequency. Compared to Resovist®, all zinc ferrite samples show a slightly steeper drop. In strong contrast to Resovist®, the magnetic response is heavily suppressed for cobalt ferrite samples, which can be attributed to about one-order larger magnetic anisotropy, effectively freezing the direction of the particle superspins in the crystal lattice (a blocked state) and forcing them to respond to the drive field purely by a rather slow Brownian

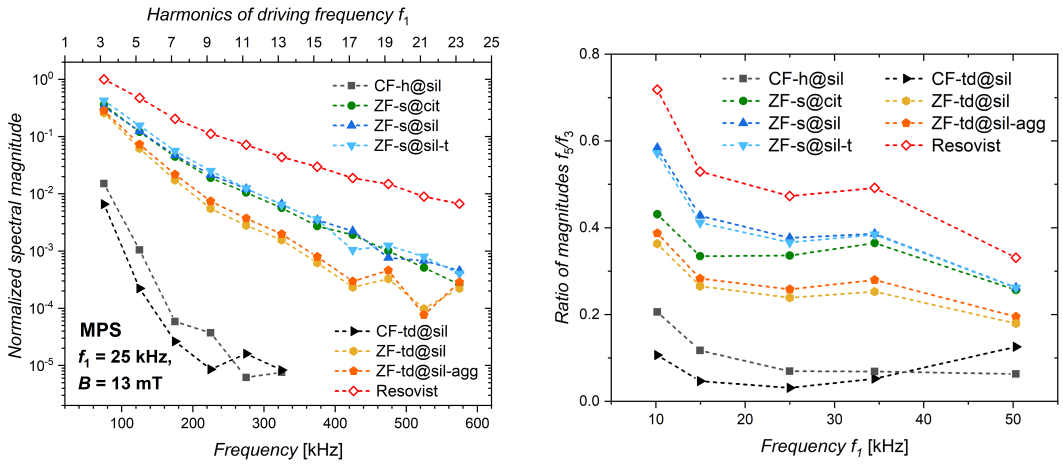

Figure 6.2: (Left) amplitudes of higher harmonics normalized so that the magnitude of the 3rd harmonics of Resovist® is unit. (Right) frequency dependence of R53 parameter for various samples determined with a 24.990 kHz excitation coil and a magnetic field of 13 mT. Adapted from [P1], the connecting lines are meant to only guide the eye.

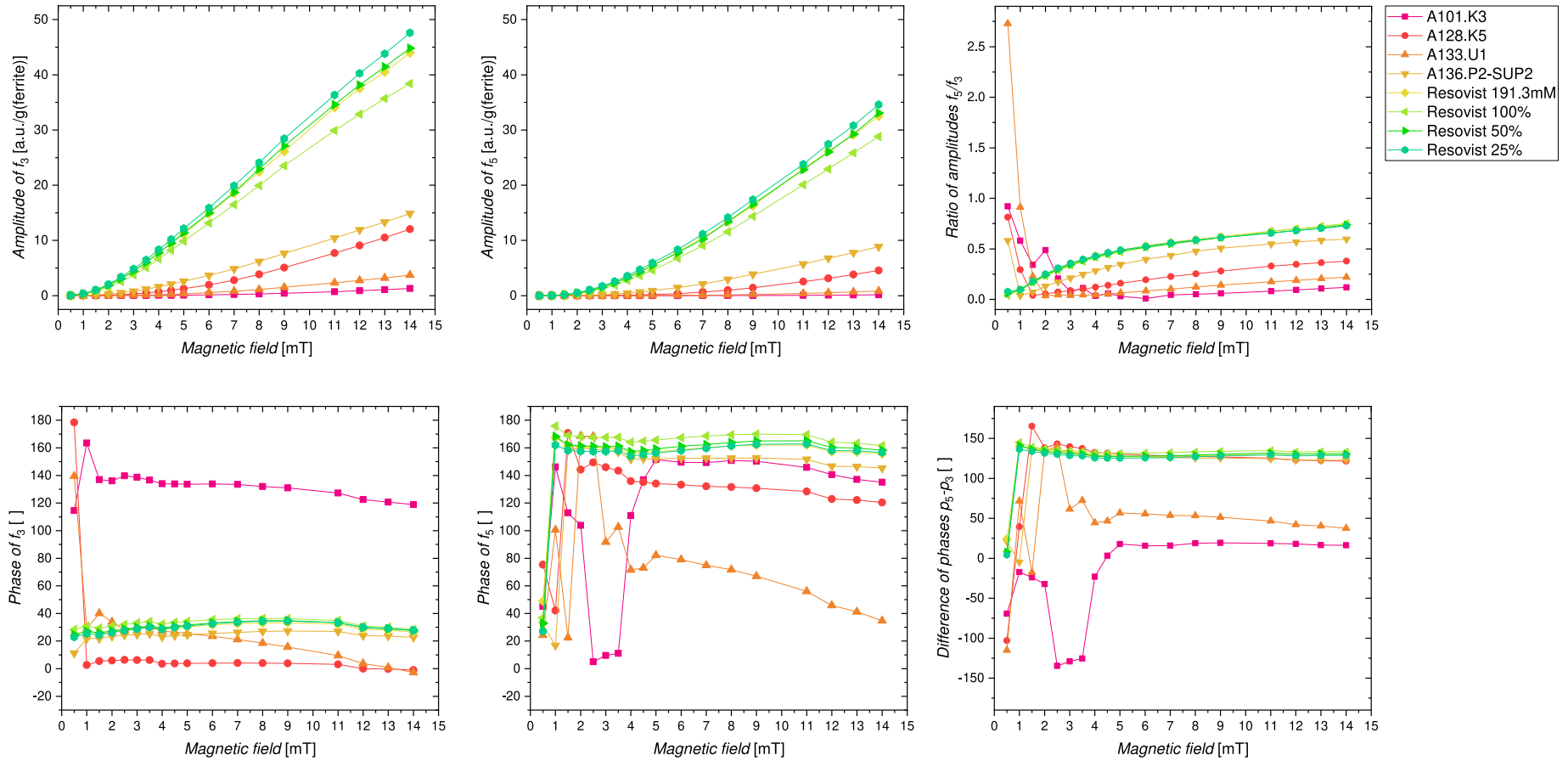

Figure 6.3: Magnetic field dependence of the spectral parameter of various suspensions of magnetic nanoparticles in f=10.156 kHz excitation coil. The percentages in the legend indicate the concentration of Resovist® in the suspension. The connecting lines are meant to only guide the eye. A hardware switch of the range setting caused a reversible fluctuation in the circuitry around 10 mT depending on the drive coil used. The error was revealed only after the measurement and this data point out of the 3σ rule range was neglected as a gross error.

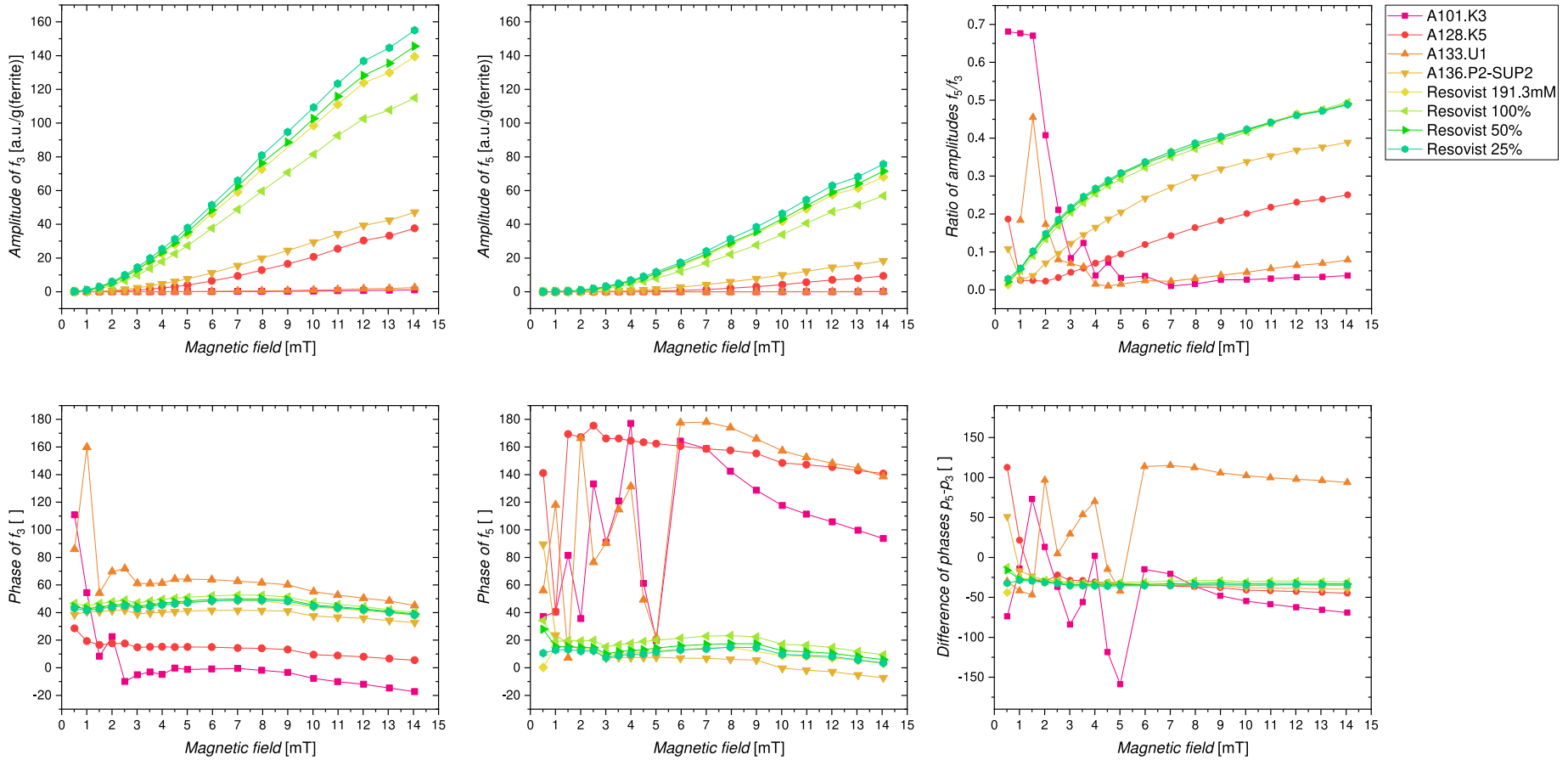

Figure 6.4: Magnetic field dependence of the spectral parameter of various suspensions of magnetic nanoparticles in f=24.990 kHz excitation coil. The percentages in the legend indicate the concentration of Resovist® in the suspension. The connecting lines are meant to only guide the eye.

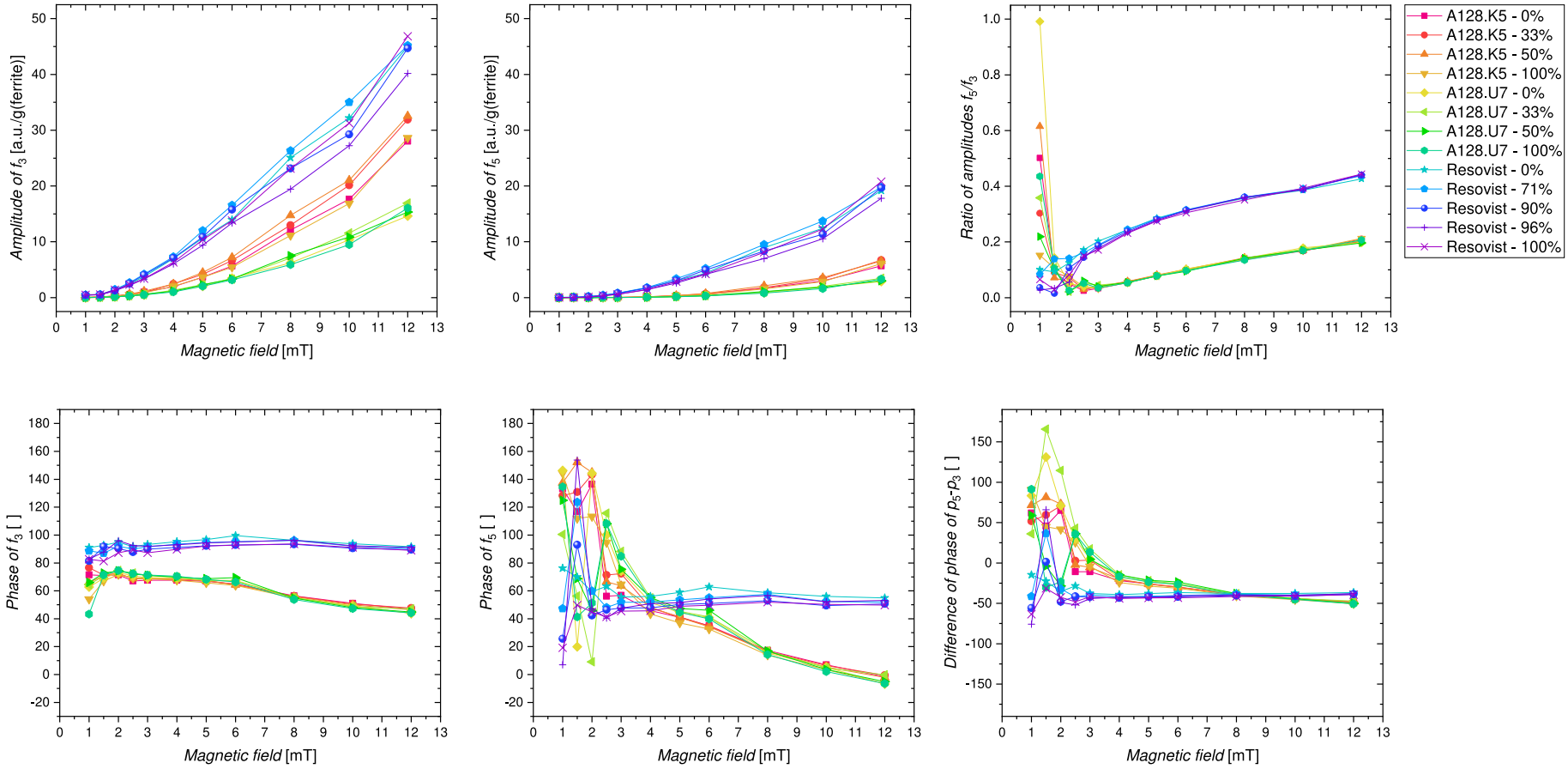

Figure 6.5: Dependence of the spectral parameter of various suspensions of magnetic nanoparticles with varying viscosity of the medium (wt% of glycerol in water-glycerol suspension) in f=50.390 kHz excitation coil. The connecting lines are meant to only guide the eye.

process. For detailed discussion see [P1].

To model the influence of the environment of various viscosities on the relaxation mechanisms of particle magnetic moments, first, viscous suspensions of zinc ferrite nanoparticles with glycerol concentrations of $\sim$ 0, 33, 50 and 100 wt% were prepared so that the weight of the nanoparticles in each sample was approximately the same. A significant effect of the glycerol concentration was observed only at higher concentrations. Based on this observation, we have prepared viscous Resovist® suspensions with a higher concentration of glycerol of $\sim$ 0, 71, 90, 96 and 100 wt% only. The structural, magnetic, and other characteristics of the samples are summarized in tables 6.1 and 6.2. The effect of the drive field amplitude on the higher harmonics frequencies of the MPS signal was studied at $\sim$ 50 kHz, for which the highest magnitudes of the parameters are expected, and weak signals could possibly also be discerned. Some research activities were carried out by student Alexandra Mészárošová working on her student faculty grant "*Magnetic particle spectroscopy of particles in a viscous medium*", who participated in the preparation of Resovist® suspensions and performed MPS experiments on a series of suspensions with different viscosity. Before MPS measurement, suspensions in cuvettes with a higher concentration of glycerol had to be ultrasonicated at an increased temperature to decrease viscosity during homogenization, however, still below 80 °C to prevent liquid evaporation and change in concentration.

The experimental curves presented in figure 6.5 and a follow-up study of frequency dependence at a drive field amplitude of 13 mT (not presented here) do not provide a systematic correlation of the spectral parameters with the viscosity of the medium in which the particle moments oscillate. Apparently, regardless of the concentration of glycerol, similar chemical environments are formed close to the surface of the individual particles, and besides the Néel relaxation that is more sensitive to changes in magnetic field [107], the moments relax by the Brown mechanism in these micelles. On the other hand, it is clear that the structure of the cores and net magnetization play a crucial role rather than their surface.

6.3 Computer simulations

To simulate the response of magnetization of the particles that presumably relax mainly by the Néel mechanism, a system with small magnetocrystalline anisotropy and large hydrodynamic volume (see Section 6.2) was idealized and experimentally realized by SPM maghemite-decorated SiO_2 balls, shown in figure 6.6. This model decreases the size of functional particles and, at the same time, reduces the agglomeration and increases the hydrodynamic size of the whole system, thus combining the advantages of each to ensure close contact of water molecules with rotating spins of the iron oxide particles in MPI applications. For the simulation of time development of normalized distribution of dipole moment orientations $W(x,t)$, the same parameters stated in Section 5.4 with the difference in particle core diameters d_c and hydrodynamic diameters, assumed to be $d_\mathrm{h} = d_\mathrm{c} + 2 \times d_\mathrm{magnemite}$ were used. The approximation of the particle hydrodynamic diameters corresponding to the particle core size led to a significant variation in the relaxation times, as can be seen in figure 6.7. The simulation confirmed that the Néel relaxation mechanism is dominant in this model system and showed a descending trend of relaxation times with the magnetic field amplitude.

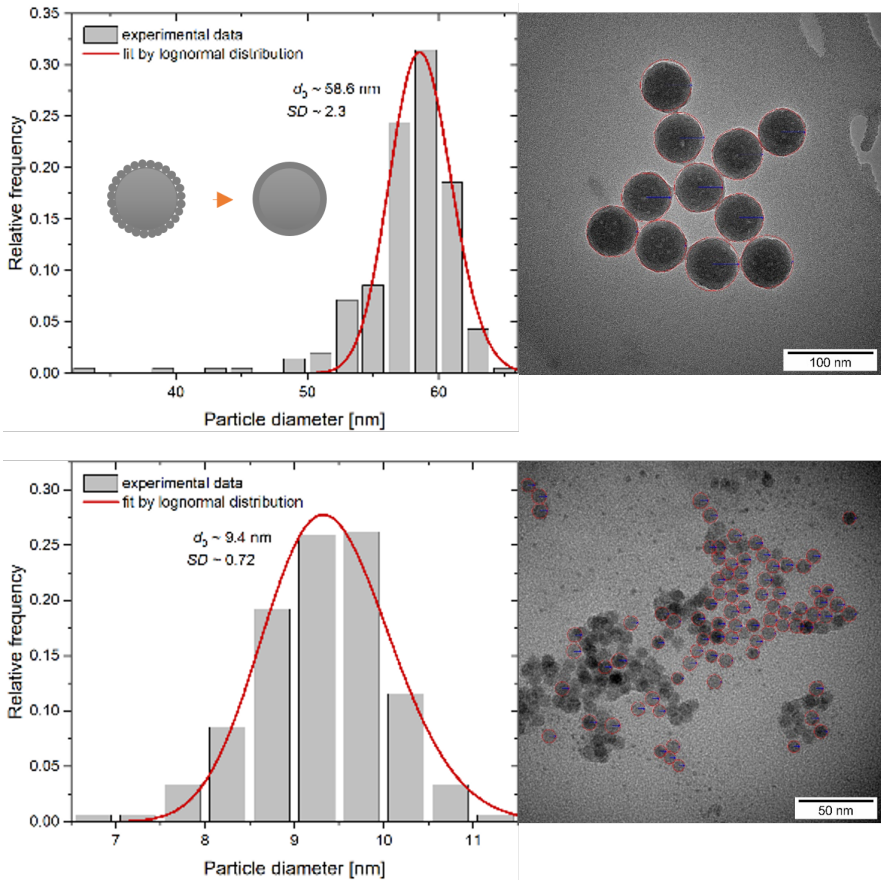

Figure 6.6: (Left) particle size distribution histograms calculated from an ensemble of $\sim$ 300 nanoparticles with an inset of idealized model used in simulation, (right top) typical TEM micrograph of SiO_2 nanoparticles used as cores for the model system with indicated determination of particle sizes, and (right bottom) maghemite nanoparticles used to decorate SiO_2 cores.

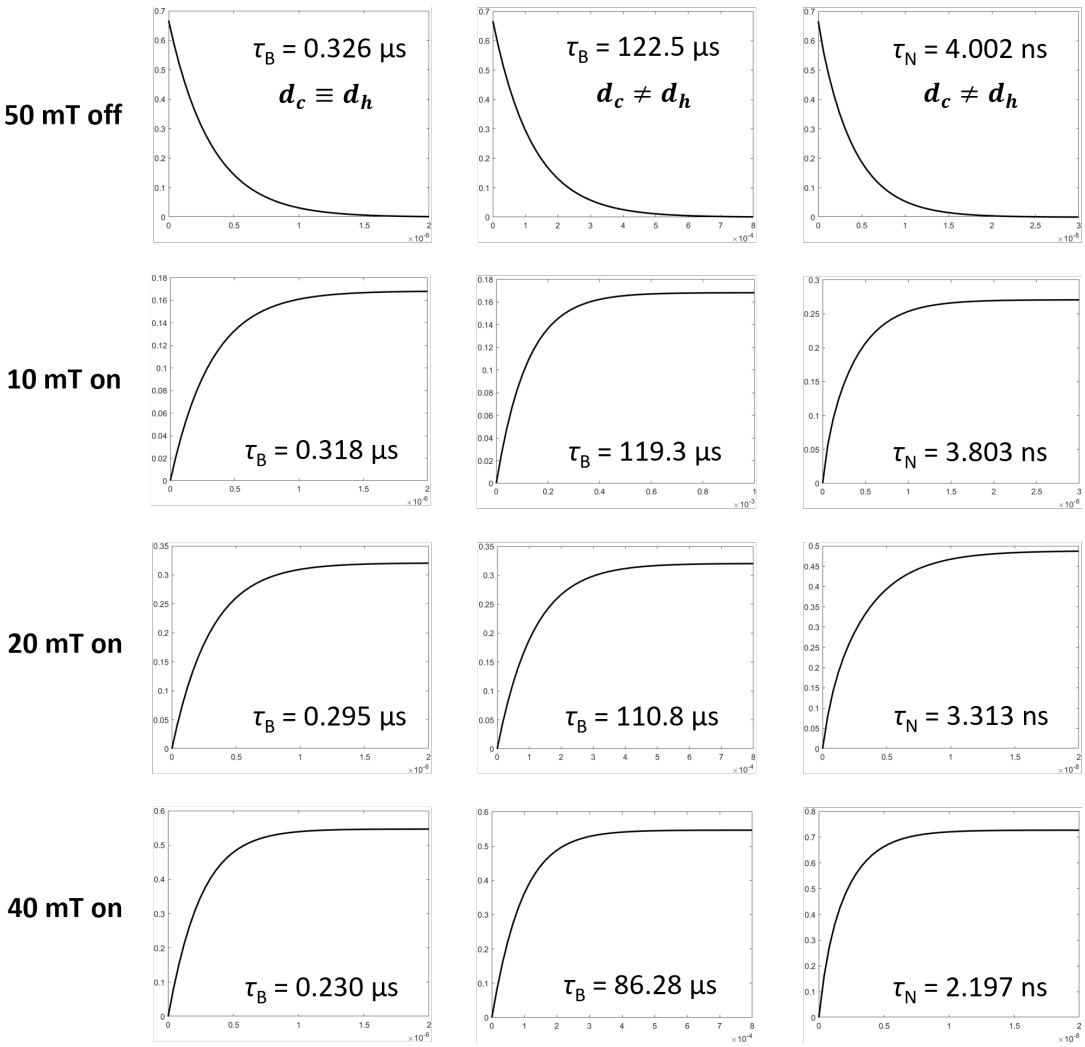

Figure 6.7: Brown and Néel relaxation times of the maghemite-decorated SiO_2 system responding to switching off or switching on step function magnetic field of various magnitudes ($W(x,t)$ versus time). The numbers for the relaxation times were determined from the eigenvalue calculations.

7. Conclusions

Main contribution of the research work

The presented doctoral thesis aimed to investigate key physical characteristics of selected nanoparticle systems based on ferric oxides and substituted magnetite-maghemite with an intended application for emerging diagnostic imaging methods and novel therapeutic interventions. To meet their high requirements for the nanoparticles, it is necessary to precisely control the phase purity, crystal structure, nanoparticle morphology, size, and distribution width, and tailor their magnetic properties, strongly connected also with the cationic occupation of crystallographic positions. A number of various magnetic nanoparticles and their functionalized derivatives synthetized by different routes were investigated primarily by ^{57}Fe Mössbauer spectroscopy (see Chapters 3 and 4), which was further advanced for specific use in nanoparticle research (see Chapter 2).

Because admixtures of multiple polymorphs typically occur in synthesized ferric iron oxide nanoparticles, we showed that only a combination of complementary methods can provide sufficient comprehensive information to identify all phases of Fe_2O_3 (α, β, γ and ε). In our particular case, we employed a synergy of XRPD, DC magnetic measurements, and MS to provide a reliable estimate of the phase composition with a detection limit for each polymorph below 1 wt%. The optimal conditions for preparation of ε-Fe_2O_3-rich sample were established with the yield of 91 %, particle size of $\sim$ 25 nm, together with the very low relative content of parasitic α-Fe_2O_3. It was observed that with an increase in the mass fraction of Fe_2O_3 in the initial mixture of precursors, the optimal annealing temperature decreases, while the width of the particle size distribution tends to increase. Spatial restriction during particle growth in defined pores of a mesoporous amorphous silica matrix proved to be a decisive factor in maximizing the yield of ε-Fe_2O_3 nanoparticles. As a result, high purity nanoparticles with impurities below 2 % (most probably of α-Fe_2O_3 nature) were obtained and their Mössbauer spectra were studied in detail. According to MS, the magnetic order is lost at the Curie temperature $\sim$ 505 K and no other high-temperature magnetically-ordered ε-phase was observed. Upon decreasing temperature, the quadrupole shifts at three nonequivalent iron cation sites approach zero below the spin-reorientation transition, which was correlated with the rotation of magnetic moments pointing along the a axis at higher temperatures to the [110] crystallographic direction based on DFT spin-polarized electronic calculation of respective EFG tensors. In a specific geometric configuration of in-field MS, when an external magnetic field is applied in parallel direction with the incident γ-beam, the nonzero intensities of the second and fifth lines of the spectrum even at 7 T are in accordance with the core-shell model described in Section 2.4. Moreover, increased magnetization of the nanoparticles and suppression of the spin-reorientation transition were achieved by substitution of Al^{3+} that preferentially occupies tetrahedral sites. The coated ε-$Al_{0.23}Fe_{1.77}O_3$ nanoparticles of low toxicity showed comparable performance in ultra-high-field MRI at 11.75 T to that of Resovist®.

A spin reorientation transition from AF to WF spin ordering occurs upon heating at the so-called Morin temperature T_M in bulk α-Fe_2O_3. We synthe-

sized α-Fe_2O_3 nanoparticles of various mean diameters and crystallite shapes and showed that the characteristic shape of the particles has only a limited effect on T_M. Given some limitations, we can conclude that the Heisenberg 3D model and the Ising model correlate relatively well with the equivalent diameter of the particles, determined by TEM analysis, whereas the mean-field approach is better suited for the minimal projection. Both the Heisenberg 3D model and the Ising model provide parameters compatible with the experimental values of T_M of the bulk material. α-Fe_2O_3 nanoparticles smaller than $\sim$ 10 nm do not pass through the Morin transition and keep the WF ordering down to the liquid helium temperature. If we assumed that the EFG tensor components do not change with decreasing size of the nanoparticles, the mean deviation angle between the basal plane and the magnetic moments of the WF phase point to an anticipated influence of the surface-to-volume ratio on spin canting within the nanoparticles. Moreover, because the blocking temperature strongly depends on the particle size, the developed theoretical model that describes the AF→WF spin-reorientation transition proved to be applicable for other systems of nanoparticles with a size distribution that pass from a magnetically blocked state to a superparamagnetic (SPM) state under some simplifying assumptions, and was further developed to determine the volume-weighted distribution of blocking temperatures.

To study the effect of surface (charge) modification on the performance of MPI tracers, γ-Fe_2O_3 magnetic cores with an average diameter $\sim$ 8 nm were stabilized as a cationic or anionic colloid and, in addition to basic characterization, tested in vitro in a field-free point MPI scanner. Compared to the commercially available SPION suspension Resovist®, the coated and uncoated cationic particles provided an insignificantly lower SNR, the uncoated anionic particles a slightly higher SNR, while the coated anionic particles had identical SNR.

By means of MS and supporting characterization methods we confirmed that the synthesis conditions play a significant role in the cation distribution and consequent magnetic properties for nanoparticles of substituted magnetite-maghemite. MS of all presented magnetic nanoparticle systems provides evidence for a long-range ferrimagnetic order, with a different degree of SPM behavior at room temperature.

$Zn_cFe_{3-c}O_4$ nanoparticles with mean diameter $\sim$ 11 nm that differ in Zn concentration ($c = 0, 0.05, 0.36$) were prepared by two-step thermal decomposition in the presence of surfactants at temperatures lower than 300 °C followed by rapid cooling. Unlike the bulk material, regardless of the strong Zn^{2+} preference to occupy the tetrahedral site, synthesis at relatively low temperature leads to a non-equilibrium distribution of Zn^{2+} cations, and nearly half of them occupy the octahedral sites. The presence of zinc atoms in the spinel ferrite structure led to an increase in net magnetization that is important for MRI and MPI applications. Silica-coated $Zn_{0.36}Fe_{2.45}\square_{0.19}O_4$ nanoparticles in SPM regime at room temperature showed slightly higher transversal relaxivities $\sim$ 324 $mM(Fe)^{-1}s^{-1}$ at 3 T for the silica coating thickness of 6.9(8) nm compared to Resovist®.

Roughly 10 nm-sized nanoparticles of $Mn_{1-x}Zn_xFe_2O_4$ (x = 0.21–0.63), synthetized by a surfactant-free hydrothermal procedure at a rather low temperature of 180 °C, proved to be suitable candidates for MRI and MPI applications, where careful adjustment of relaxation behavior and reasonably high magnetization are important. Analysis of the broadening of the XRPD line provided a mean

crystallite size that gradually decreased with increasing zinc content, which was attributed to a slightly smaller size of Zn^{2+} cations compared to Mn^{2+}. Room-temperature Mössbauer spectra together with magnetic measurements provided valuable insight into the blocking behavior of particles on two distinct time scales and demonstrated that Néel relaxation can be enhanced by increasing the zinc content. The combination of MS, analysis of neutron diffraction data, and furthermore supported by DFT study, revealed the formation of a partially inverse spinel structure with $\approx 1/3$ of Zn^{2+} cations located in the octahedral sites and almost random distribution of Mn^{2+} between the two crystallographic sites.

The similarities among the samples of strictly 10 nm-sized $Mn_{1-x}Co_xFe_2O_4$ (x = 0.19–0.77) nanoparticles, synthetized using an oleate-based solvothermal method at a rather low temperature of 220 °C, in terms of particle (crystallite) size distribution characteristics allowed the interpretation of the presented results exclusively on the basis of the actual composition, beyond the influence of other structural or morphological parameters. Assuming there are no vacancies in the structure, samples can be distinguished into two groups - those with a manganese content of up to about 40 % of total divalent cations, characterized by Mn^{2+} cations equally distributed in both tetrahedral and octahedral sites, and Co^{2+} present only in the octahedral sites, and Co richer samples that have all Mn^{2+} cations in the octahedral sites. In comparison to the manganese zinc ferrite nanoparticles, Co substitution led to an increased net magnetization; however, magnetic nanoparticles with this composition may not be preferred in medical applications, because cobalt in the structure could potentially increase the toxicity of the nanoparticles.

Although a distinction between the contributions of the core and the shell to the MS spectra was not possible in the mentioned nanoparticle systems based on substituted magnetite-maghemite, the magnitude of the mean angle between the γ-beam and the $\vec{B}_{\text{eff}}$ vector correlated with the variations in the mean particle size. On the other hand, the relative content of the shell volume in ε-Fe_2O_3/SiO_2 nanoparticles could be determined by MS, and under some simplifying assumptions, it leads to a shell thickness of 1.83(5) nm.

Upon the investigation of magnetic nanoparticles of potential use in medical applications, a new direction emerged for the doctoral project, which resulted in the construction of a magnetic particle spectrometer (see Chapters 5 and 6) that combines the filtering and cancellation method, with a broad spectrum of operating frequencies ($\sim$ 10, 15, 25, 35, and 50 kHz) and the driving field oscillating purely sinusoidal with a magnetic induction of up to 20 mT. Drive field frequencies and field strength limitations were selected to roughly correspond to the preclinical MPI scanners used for imaging of animal models. The script for the processing of the time-dependent signal from MPS was developed to deduce the amplitudes of higher harmonics of the drive field frequency and other relevant parameters.

To study relaxation mechanisms by MPS, we provided the characterization of magnetic nanoparticles of two different compositions, synthetized at relatively low temperatures below 300 °C, based on cobalt and zinc ferrites that were chosen because of their different magnetic behavior at room temperature. The $Zn_{0.34}Fe_{2.51}O_4$ nanoparticles prepared by a two-step thermal decomposition (TD) and solvothermally prepared $Zn_{0.32}Fe_{2.52}O_4$ nanoparticles evidenced the prefer-

ence of Zn^{2+} to occupy the tetrahedral site over the octahedral site regardless of the synthesis method. Almost a random distribution of Co^{2+} over both crystallographic sites was observed for the nanoparticles of $Co_{1.06}Fe_{1.94}O_4$ prepared under hydrothermal conditions, while in $Co_{0.68}Fe_{2.30}O_4$ nanoparticles prepared by two-step thermal decomposition, Co^{2+} predominantly occupies the octahedral sites. Up to 23 higher harmonics could be discerned in a MPS signal of particles measured in a magnetic field of 13 mT, oscillating with frequency of $\sim$ 25 kHz. Although magnetic cores do not perform as well as Resovist®, the study provides information relevant for further research in this area. On a logarithmic scale, all zinc ferrite samples show a slightly steeper drop in the amplitudes of higher harmonics with frequency. The magnetic response is heavily suppressed for the cobalt ferrite samples, which can be attributed to about one-order larger magnetic anisotropy manifested in a blocked state of nanoparticles, forcing them to respond to the drive field purely by a rather slow Brownian relaxation process.

Another two series of $Zn_{0.34}Fe_{2.51}O_4$ magnetic cores encapsulated in silica as individual particles and clusters of particles coated with silica, and dispersed in suspensions with changing glycerol-water ratios, were prepared to model the influence of the environment of various viscosity on the relaxation mechanisms of particle magnetic moments in an oscillating external magnetic field of various amplitudes and frequencies. A significant effect of viscosity was observed only at higher concentrations of glycerol, and no systematic correlation of the spectral parameters with the viscosity of the medium in which the particle moments oscillate was observed.

A system that combines the advantages of small functional particles with low magnetocrystalline anisotropy and large total hydrodynamic volume was idealized to ensure close contact of water molecules with rotating spins of iron oxide particles in MPI applications, and was experimentally realized by SPM maghemite-decorated SiO_2 balls that, at the same time, led to reduced agglomeration. The script was implemented to numerically solve FPE assuming a pure Brown or Néel relaxation process. The simulation of the response of magnetization of such particles confirmed that the Néel relaxation mechanism is dominant and showed a descending trend of relaxation times with the magnetic field amplitude.

Future outlook

In the Mössbauer spectra of ε-Fe_2O_3 nanoparticles, the lineshape asymmetry toward smaller hyperfine magnetic fields might be caused by embedding of the Si^{4+} cations from the silica matrix in the structure of nanoparticles during nucleation process. However, follow-up studies of high-purity ε-Fe_2O_3 nanoparticle composite by STEM and ab initio calculations have not yet provided clear evidence for this hypothesis.

To further develop the code for the simulation of the magnetization response in an oscillating magnetic field, the next logical step would be to implement automation of the matrix size limit and the estimation of initial boundary conditions that play a key role in simulation duration.

To correlate the simulated signal with the MPS experiment, we plan to study the limit cases of relaxation mechanisms. There are several possibilities of how to increase the contribution of Néel relaxation over the Brownian one, e.g., to

increase the magnetic moment per particle or to decrease the magnetocrystalline anisotropy, both of which can be achieved by chemical substitutions; or to optimize particle morphology by decreasing mean core size and width of the size distribution, and by increasing hydrodynamic volume. To experimentally model purely Néel relaxation using Resovist®, we will restrain the motion of the nanoparticles by embedding them into a solid matrix (e.g. wax).

In a similar manner for Brown relaxation and based on our experience with this material, we will prepare a highly concentrated suspension of ε-Fe_2O_3 nanoparticles that are unique due to their high magnetocrystalline anisotropy and extremely large coercive field at room temperature. Moreover, we plan to implement a simpler Langevin model with linear Debye dynamics [114] for particles relaxing by the Brown mechanism that also covers the dynamics of higher harmonics in the frequency domain. Compared to the numerical solution of FPE, this is supposed to be computationally very efficient and might be used to fit the MPS signal to determine the particle properties.

Bibliography

[1] E. Pollert, P. Veverka, M. Veverka, O. Kaman, K. Závěta, S. Vasseur, R. Epherre, G. Goglio, E. Duguet, *Progress in Solid State Chemistry* **2009**, *37*, 1–14, DOI 10.1016/j.progsolidstchem.2009.02.001.

[2] Y. Wang, H. Gu, *Advanced Materials* **2015**, *27*, 576–585, DOI 10.1002/adma.201401124.

[3] P. Veverka, L. Kubíčková, Z. Jirák, V. Herynek, M. Veverka, O. Kaman, *Materials Chemistry and Physics* **2021**, *260*, 124178, DOI 10.1016/j.matchemphys.2020.124178.

[4] T. Sun, Y. S. Zhang, B. Pang, D. C. Hyun, M. Yang, Y. Xia, *Angewandte Chemie International Edition* **2014**, *53*, 12320–12364, DOI 10.1002/anie.201403036.

[5] M. Sanna Angotzi, V. Mameli, C. Cara, A. Musinu, C. Sangregorio, D. Niznansky, H. L. Xin, J. Vejpravova, C. Cannas, *Nanoscale Adv.* **2020**, *2*, 3191–3201, DOI 10.1039/D0NA00134A.

[6] I. Dirba, C. Chandra, Y. Ablets, J. Kohout, T. Kmječ, O. Kaman, O. Gutfleisch, *Journal of Physics D: Applied Physics* **2023**, *56*, DOI 10.1088/1361-6463/aca0a9.

[7] J. Stergar, Z. Jirák, P. Veverka, L. Kubíčková, T. Vrba, J. Kuličková, K. Knížek, F. Porcher, J. Kohout, O. Kaman, *Journal of Magnetism and Magnetic Materials* **2019**, *475*, 429–435, DOI 10.1016/j.jmmm.2018.11.020.

[8] K. Závěta, J. Kohout, A. Lančok, *Čs. čas. fyz.* **2012**, *62*, 51–58.

[9] R. L. Mössbauer, *Die Naturwissenschaften* **1958**, *45*, 538–539, DOI 10.1007/bf00632050.

[10] R. L. Mössbauer, *Zeitschrift für Physik* **1958**, *151*, 124–143, DOI 10.1007/bf01344210.

[11] R. L. Mössbauer, *Zeitschrift für Naturforschung A* **1959**, *14*, 211–216, DOI 10.1515/zna-1959-0303.

[12] U. Gonser, *Mössbauer Spectroscopy (Topics in applied physics, Volume 5)*, Springer Berlin, Heidelberg, **2014**.

[13] P. Gütlich, E. Bill, A. Trautwein, *Mössbauer Spectroscopy and Transition Metal Chemistry: Fundamentals and Applications*, Springer Berlin, Heidelberg, **2010**.

[14] F. Fernandini Parodi, A. Trujillo Quinde, M. Mejía Santillán, S. Cuadros Gómez, *Boletín de Arqueología PUCP* **2019**, 49–66, DOI 10.18800/boletindearqueologiapucp.201902.003.

[15] WissEl - Wissenschaftliche Elektronik GmbH 2024, Mössbauer systems and related equipment, http://www.wissel-instruments.de/, accessed 19.02.2024.

[16] Goodfellow 2024, https://www.goodfellow.com/uk/en-gb/displayitemdetails/p/fe00-fl-000210/iron-foil, accessed 19.02.2024.

[17] Model 12CNDT-6T Mössbauer insert Operational manual, tech. rep.

[18] Cernox data sheet, tech. rep.

[19] T. Kmječ, PhD thesis, Faculty of Mathematics od Physics, Charles University, **2021**.

[20] T. Žák, Y. Jirásková, *Surface and Interface Analysis* **2006**, *38*, 710–714, DOI 10.1002/sia.2285.

[21] Z. Klencsár, E. Kuzmann, A. Vértes, *Journal of Radioanalytical and Nuclear Chemistry* **1996**, *210*, 105–118, DOI doi.org/10.1007/BF02055410.

[22] M. E. Matsnev, V. S. Rusakov, *AIP Conference Proceedings* **2012**, *1489*, 178–185, DOI 10.1063/1.4759488.

[23] V. Veselý, T. Zemčík, *Hyperfine Interactions* **1990**, *58*, 2679–2685, DOI 10.1007/BF02398397.

[24] Z. Klencsár, *Nuclear Instruments and Methods in Physics Research Section B: Beam Interactions with Materials and Atoms* **1997**, *129*, 527–533, DOI 10.1016/S0168-583X(97)00314-5.

[25] K. Levenberg, *Quarterly of Applied Mathematics* **1944**, *2*, 164–168, DOI 10.1090/QAM/10666.

[26] D. W. Marquardt, *Journal of the Society for Industrial and Applied Mathematics* **1963**, *11*, 431–441, DOI 10.1137/0111030.

[27] N. Blaes, H. Fischer, U. Gonser, *Nuclear Instruments and Methods in Physics Research Section B: Beam Interactions with Materials and Atoms* **1985**, *9*, 201–208, DOI 10.1016/0168-583X(85)90683-4.

[28] Z. Klencsár, *AIP Conference Proceedings* **2014**, *1622*, 30–39, DOI 10.1063/1.4898608.

[29] M. Blume, J. A. Tjon, *Phys. Rev.* **1968**, *165*, 446–456, DOI 10.1103/PhysRev.165.446.

[30] D. H. Jones, K. K. P. Srivastava, *Phys. Rev. B* **1986**, *34*, 7542–7548, DOI 10.1103/PhysRevB.34.7542.

[31] D. Rancourt, J. Ping, *Nuclear Instruments and Methods in Physics Research Section B: Beam Interactions with Materials and Atoms* **1991**, *58*, 85–97, DOI 10.1016/0168-583X(91)95681-3.

[32] K. Lagarec, D. Rancourt, *Nuclear Instruments and Methods in Physics Research Section B: Beam Interactions with Materials and Atoms* **1997**, *129*, 266–280, DOI 10.1016/S0168-583X(97)00284-X.

[33] A. Stubna, D.-H. Jo, M. Costas, W. W. Brenessel, H. Andres, E. L. Bominaar, E. Münck, L. Que, *Inorganic Chemistry* **2004**, *43*, 3067–3079, DOI 10.1021/ic030296k.

[34] F. Grandjean, G. J. Long, *Chemistry of Materials* **2021**, *33*, 3878–3904, DOI 10.1021/acs.chemmater.1c00326.

[35] E. De Grave, A. Van Alboom, *Physics and Chemistry of Minerals* **1991**, *18*, 337–342, DOI 10.1007/BF00200191.

[36] S. M. Dubiel, J. Cieślak, *Journal of Physics D: Applied Physics* **2016**, *49*, 135401, DOI 10.1088/0022-3727/49/13/135401.

[37] H. L. Zhang, *Geoscience Frontiers* **2022**, *13*, 101316, DOI 10.1016/j.gsf.2021.101316.

[38] H.-D. Pfannes, U. Gonser, *Applied physics* **1973**, *1*, 93–102, DOI 10.1007/BF00887072.

[39] E. Tronc, A. Ezzir, R. Cherkaoui, C. Chanéac, M. Noguès, H. Kachkachi, D. Fiorani, A. Testa, J. Grenèche, J. Jolivet, *Journal of Magnetism and Magnetic Materials* **2000**, *221*, Proceedings of the 3rd Euroconference on Magnetic Properties of Fine Particles and their Relevance to Materials Science, 63–79, DOI 10.1016/S0304-8853(00)00369-3.

[40] N. Joudeh, D. Linke, *Journal of Nanobiotechnology* **2022**, *20*, DOI 10.1186/s12951-022-01477-8.

[41] S. Ganguly, S. Margel, *Pharmaceutics* **2023**, *15*, DOI 10.3390/pharmaceutics15020686.

[42] S. Mørup, D. E. Madsen, C. Frandsen, C. R. H. Bahl, M. F. Hansen, *Journal of Physics: Condensed Matter* **2007**, *19*, 213202, DOI 10.1088/0953-8984/19/21/213202.

[43] J. Zhao, F. E. Huggins, Z. Feng, G. P. Huffman, *Physical review. B Condensed matter* **1996**, *54*, 13403–3407, DOI 10.1103/physrevb.54.3403.

[44] L. Néel in Annales de géophysique, *Vol. 5*, **1949**, pp. 99–136.

[45] P. W. Anderson, *Journal of the Physical Society of Japan* **1954**, *9*, 316–339, DOI 10.1143/JPSJ.9.316.

[46] S. Dattagupta, M. Blume, *Phys. Rev. B* **1974**, *10*, 4540–4550, DOI 10.1103/PhysRevB.10.4540.

[47] J. M. D. Coey, *Phys. Rev. Lett.* **1971**, *27*, 1140–1142, DOI 10.1103/PhysRevLett.27.1140.

[48] D. Kubániová, bachelors thesis, Faculty of Mathematics od Physics, Charles University, **2012**.

[49] L. Machala, J. Tuček, R. Zbořil, *Chemistry of Materials* **2011**, *23*, 3255–3272, DOI 10.1021/cm200397g.

[50] R. Zboril, M. Mashlan, D. Petridis, *Chemistry of Materials* **2002**, *14*, 969–982, DOI 10.1021/cm0111074.

[51] J. Tuček, L. Machala, S. Ono, A. Namai, M. Yoshikiyo, K. Imoto, H. Tokoro, S.-i. Ohkoshi, R. Zbořil, *Scientific Reports* **2015**, *5*, DOI 10.1038/srep15091.

[52] R. B. Bergmann, A. Bill, *Journal of Crystal Growth* **2008**, *310*, 3135–3138, DOI 10.1016/j.jcrysgro.2008.03.034.

[53] S. Sakurai, A. Namai, K. Hashimoto, S.-i. Ohkoshi, *Journal of the American Chemical Society* **2009**, *131*, 18299–18303, DOI 10.1021/ja9046069.

[54] V. Herynek, M. Babič, O. Kaman, H. Charvátová, M. Veselá, L. Šefc, *International Journal on Magnetic Particle Imaging* **2020**, Vol 6 No 2 Suppl. 1 (2020), DOI 10.18416/IJMPI.2020.2009019.

[55] P. Reimer, T. Balzer, *European Radiology* **2003**, *13*, 1266–1276, DOI 10.1007/s00330-002-1721-7.

[56] L. Corbellini, C. Lacroix, D. Ménard, A. Pignolet, *Scripta Materialia* **2017**, *140*, 63–66, DOI 10.1016/j.scriptamat.2017.07.005.

[57] S. Sakurai, J. Jin, K. Hashimoto, S.-i. Ohkoshi, *Journal of the Physical Society of Japan* **2005**, *74*, 1946–1949, DOI 10.1143/JPSJ.74.1946.

[58] M. Gich, C. Frontera, A. Roig, E. Taboada, E. Molins, H. R. Rechenberg, J. D. Ardisson, W. A. A. Macedo, C. Ritter, V. Hardy, J. Sort, V. Skumryev, J. Nogués, *Chemistry of Materials* **2006**, *18*, 3889–3897, DOI 10.1021/cm0609931.

[59] Y.-C. Tseng, N. M. Souza-Neto, D. Haskel, M. Gich, C. Frontera, A. Roig, M. van Veenendaal, J. Nogués, *Physical Review B* **2009**, *79*, DOI 10.1103/physrevb.79.094404.

[60] J. L. García-Muñoz, A. Romaguera, F. Fauth, J. Nogués, M. Gich, *Chemistry of Materials* **2017**, *29*, 9705–9713, DOI 10.1021/acs.chemmater.7b03417.

[61] J. Kuriplach, "unpublished results".

[62] C. Frandsen, S. Mørup, *Phys. Rev. Lett.* **2005**, *94*, 027202, DOI 10.1103/PhysRevLett.94.027202.

[63] Ö. Özdemir, D. J. Dunlop, T. S. Berquó, *Geochemistry Geophysics Geosystems* **2008**, *9*, Q10Z01, DOI 10.1029/2008GC002110.

[64] R. E. Vandenberghe, E. De Grave, C. Landuydt, L. H. Bowen, *Hyperfine Interactions* **1990**, *53*, 175–195, DOI 10.1007/BF02101046.

[65] H. M. Lu, X. K. Meng, *The Journal of Physical Chemistry C* **2010**, *114*, 21291–21295, DOI 10.1021/jp108703b.

[66] T. Ambrose, C. L. Chien, *Phys. Rev. Lett.* **1996**, *76*, 1743–1746, DOI 10.1103/PhysRevLett.76.1743.

[67] X. Wang, J. Zhuang, Q. Peng, Y. Li, *Nature* **2005**, *437*, 121–124, DOI 10.1038/nature03968.

[68] N. Amin, S. Arajs, *Phys. Rev. B* **1987**, *35*, 4810–4811, DOI 10.1103/PhysRevB.35.4810.

[69] M. Vasquez-Mansilla, R. Zysler, C. Arciprete, M. Dimitrijewits, D. Rodriguez-Sierra, C. Saragovi, *Journal of Magnetism and Magnetic Materials* **2001**, *226-230*, Proceedings of the International Conference on Magnetism (ICM 2000), 1907–1909, DOI 10.1016/S0304-8853(00)00858-1.

[70] G. J. Muench, S. Arajs, E. Matijević, *physica status solidi (a)* **1985**, *92*, 187–192, DOI 10.1002/pssa.2210920117.

[71] American Regent, Inc, 2022, https://www.venofer.com/, accessed 19.02.2024.

[72] Y. V. Knyazev, D. A. Balaev, V. L. Kirillov, O. A. Bayukov, O. N. Mart'yanov, *JETP Letters* **2018**, *108*, 527–531, DOI 10.1134/S0021364018200092.

[73] S. Mørup, H. Topsøe, *Applied physics* **1976**, *11*, 63–66, DOI 10.1007/BF00895017.

[74] B. Knight, L. H. Bowen, R. D. Bereman, S. Huang, E. De Grave, *Journal of Inorganic Biochemistry* **1999**, *73*, 227–233, DOI 10.1016/S0162-0134(99)00020-3.

[75] J. I. Langford, A. J. C. Wilson, *Journal of Applied Crystallography* **1978**, *11*, 102–113, DOI 10.1107/S0021889878012844.

[76] G. Salazar-Alvarez, J. Qin, V. Šepelák, I. Bergmann, M. Vasilakaki, K. N. Trohidou, J. D. Ardisson, W. A. A. Macedo, M. Mikhaylova, M. Muhammed, M. D. Baró, J. Nogués, *Journal of the American Chemical Society* **2008**, *130*, 13234–13239, DOI 10.1021/ja0768744.

[77] V. G. Harris, V. Šepelák, *Journal of Magnetism and Magnetic Materials* **2018**, *465*, 603–610, DOI 10.1016/j.jmmm.2018.05.100.

[78] A. R. West, *Solid state chemistry and its applications*, John Wiley & Sons, Ltd. Chichester, West Sussex, **2014**.

[79] R. W. Grimes, A. B. Anderson, A. H. Heuer, *Journal of the American Chemical Society* **1989**, *111*, 1–7, DOI 10.1021/ja00183a001.

[80] J. M. D. Coey, *Magnetism and Magnetic Materials*, Cambridge University Press, **2010**.

[81] D. Peddis, N. Yaacoub, M. Ferretti, A. Martinelli, G. Piccaluga, A. Musinu, C. Cannas, G. Navarra, J. M. Greneche, D. Fiorani, *Journal of Physics: Condensed Matter* **2011**, *23*, 426004, DOI 10.1088/0953-8984/23/42/426004.

[82] K. Vamvakidis, M. Katsikini, D. Sakellari, E. C. Paloura, O. Kalogirou, C. Dendrinou-Samara, *Dalton Trans.* **2014**, *43*, 12754–12765, DOI 10.1039/C4DT00162A.

[83] A. Kozlowski, Z. Kakol, R. Zalecki, K. Knight, J. Sabol, J. M. Honig, *Journal of Physics: Condensed Matter* **1999**, *11*, 2749, DOI 10.1088/0953-8984/11/13/011.

[84] P. Novák, H. Št ěpánková, J. Englich, J. Kohout, V. A. M. Brabers, *Phys. Rev. B* **2000**, *61*, 1256–1260, DOI 10.1103/PhysRevB.61.1256.

[85] E. J. W. VERWEY, *Nature* **1939**, *144*, 327–328, DOI 10.1038/144327b0.

[86] M. S. Angotzi, V. Mameli, A. Musinu, D. Ňižňanský, *Journal of nanoscience and nanotechnology* **2019**, *19*, 5008–5013, DOI 10.1166/jnn.2019.16793.

[87] O. Kaman, T. Kořínková, Z. Jirák, M. Maryško, M. Veverka, *Journal of Applied Physics* **2015**, *117*, 17C706, DOI 10.1063/1.4907232.

[88] V. Šepelák, K. Becker, *Materials Science and Engineering: A* **2004**, *375–377*, 861–864, DOI 10.1016/j.msea.2003.10.178.

[89] M. R. J. Carroll, R. C. Woodward, M. J. House, W. Y. Teoh, R. Amal, T. L. Hanley, T. G. S. Pierre, *Nanotechnology* **2009**, *21*, 035103, DOI 10.1088/0957-4484/21/3/035103.

[90] R. D. Shannon, *Acta Crystallographica Section A* **1976**, *32*, 751–767, DOI 10.1107/S0567739476001551.

[91] K. Ohta, *Journal of the Physical Society of Japan* **1963**, *18*, 685–690, DOI 10.1143/JPSJ.18.685.

[92] B. Gleich, J. Weizenecker, *Nature* **2005**, *435*, 1214–1217, DOI 10.1038/nature03808.

[93] P. Debye, *Journal of the Society of Chemical Industry* **1929**, *48*, 1036–1037, DOI 10.1002/jctb.5000484320.

[94] W. F. Brown, *Phys. Rev.* **1963**, *130*, 1677–1686, DOI 10.1103/PhysRev.130.1677.

[95] M. D. Cowley, *Journal of Fluid Mechanics* **1989**, *200*, 597–599, DOI 10.1017/S0022112089220773.

[96] B. K. P. Scaife, *Journal of Physics D: Applied Physics* **1986**, *19*, L195, DOI 10.1088/0022-3727/19/10/001.

[97] P. W. Goodwill, S. M. Conolly, *IEEE Transactions on Medical Imaging* **2010**, *29*, 1851–1859, DOI 10.1109/tmi.2010.2052284.

[98] J. Weizenecker, J. Borgert, B. Gleich, *Physics in Medicine and Biology* **2007**, *52*, 6363–6374, DOI 10.1088/0031-9155/52/21/001.

[99] R. M. Ferguson, K. R. Minard, K. M. Krishnan, *Journal of Magnetism and Magnetic Materials* **2009**, *321*, 1548–1551, DOI 10.1016/j.jmmm.2009.02.083.

[100] L. R. Croft, P. W. Goodwill, J. J. Konkle, H. Arami, D. A. Price, A. X. Li, E. U. Saritas, S. M. Conolly, *Medical Physics* **2016**, *43*, 424–435, DOI 10.1118/1.4938097.

[101] K. Wu, D. Su, R. Saha, D. Wong, J.-P. Wang, *Journal of Physics D: Applied Physics* **2019**, *52*, 173001, DOI 10.1088/1361-6463/ab03c0.

[102] K. Wu, D. Su, R. Saha, J. Liu, V. K. Chugh, J.-P. Wang, *ACS Applied Nano Materials* **2020**, *3*, 4972–4989, DOI 10.1021/acsanm.0c00890.

[103] S. Biederer, T. Knopp, T. F. Sattel, K. Lüdtke-Buzug, B. Gleich, J. Weizenecker, J. Borgert, T. M. Buzug, *Journal of Physics D: Applied Physics* **2009**, *42*, 205007, DOI 10.1088/0022-3727/42/20/205007.

[104] M. Graeser, T. Knopp, M. Grüttner, T. F. Sattel, T. M. Buzug, *Medical Physics* **2013**, *40*, 042303, DOI 10.1118/1.4794482.

[105] C. Kittel, P. McEuen, *Introduction to Solid State Physics*, John Wiley & Sons, **2018**.

[106] J. Weizenecker, *Physics in Medicine & Biology* **2018**, *63*, 035004, DOI 10.1088/1361-6560/aaa186.

[107] R. J. Deissler, Y. Wu, M. A. Martens, *Medical Physics* **2014**, *41*, 012301, DOI 10.1118/1.4837216.

[108] M. I. Shliomis, V. I. Stepanov in *Advances in Chemical Physics*, John Wiley & Sons, Ltd, **1994**, Chapter 1, pp. 1–30, DOI 10.1002/9780470141465.ch1.

[109] R. M. Ferguson, K. R. Minard, A. P. Khandhar, K. M. Krishnan, *Medical Physics* **2011**, *38*, 1619–1626, DOI 10.1118/1.3554646.

[110] K. Wu, L. Tu, D. Su, J.-P. Wang, *Journal of Physics D: Applied Physics* **2017**, *50*, 085005, DOI 10.1088/1361-6463/aa590b.

[111] MathWorks 2024, https://www.mathworks.com/help/matlab/ref/ode15s.html, accessed 19.02.2024.

[112] R. Borny, PhD thesis, Medical University of Vienna, **2014**.

[113] M. Zhang, B. L. Cushing, C. J. O'Connor, *Nanotechnology* **2008**, *19*, 085601, DOI 10.1088/0957-4484/19/8/085601.

[114] T. Wawrzik, T. Yoshida, M. Schilling, F. Ludwig, *IEEE Transactions on Magnetics* **2015**, *51*, Publisher Copyright: © 2014 IEEE., 5300404, DOI 10.1109/TMAG.2014.2332371.

Author's thesis related papers

[P1] O. Kaman, D. Kubániová, L. Kubíčková, V. Herynek, P. Veverka, Z. Jirák, M. Pashchenko, T. Kmječ, M. Veverka, M. Štorkán, U. G. Hofmann, J. Kohout, "Magnetic particle spectroscopy and magnetic particle imaging of zinc and cobalt ferrite nanoparticles – distinct relaxation mechanisms", *Journal of Alloys and Compounds* **2023**, 173022, DOI 10.1016/j.jallcom.2023.173022.

[P2] V. Herynek, M. Babič, O. Kaman, H. Charvátová, M. Veselá, O. Buchholz, M. Vosmanská, D. Kubániová, J. Kohout, U. Hofmann, L. Šefc, "Maghemite nanoparticles coated by methacrylamide-based polymer for magnetic particle imaging", *Journal of Nanoparticle Research* **2021**, *23*, DOI 10.1007/s11051-021-05164-x.

[P3] O. Kaman, D. Kubániová, K. Knížek, L. Kubíčková, M. Klementová, J. Kohout, Z. Jirák, "Structure and magnetic state of hydrothermally prepared Mn-Zn ferrite nanoparticles", *Journal of Alloys and Compounds* **2021**, *888*, DOI 10.1016/j.jallcom.2021.161471.

[P4] M. Sanna Angotzi, V. Mameli, D. Zákutná, D. Kubániová, C. Cara, C. Cannas, "Evolution of the magnetic and structural properties with the chemical composition in oleate-capped $Mn_xCo_{1-x}Fe_2O_4$ nanoparticles", *Journal of Physical Chemistry C* **2021**, *125*, 20626–20638, DOI 10.1021/acs.jpcc.1c06211.

[P5] L. Kubíčková, O. Kaman, P. Veverka, V. Herynek, P. Brázda, M. Vosmanská, T. Kmječ, P. Dvořák, D. Kubániová, J. Kohout, "The ϵ-$Al_xFe_{2-x}O_3$ nanomagnets as MRI contrast agents: Factors influencing transverse relaxivity", *Colloids and Surfaces A: Physicochemical and Engineering Aspects* **2020**, *589*, DOI 10.1016/j.colsurfa.2020.124423.

[P6] D. Kubániová, P. Brázda, K. Závěta, T. Kmječ, M. Klementová, J. Kohout, "Identification of ferric oxide polymorphs in nanoparticles prepared by sol-gel method and maximization of ϵ-Fe_2O_3 content", *Journal of Magnetism and Magnetic Materials* **2019**, *472*, 96–103, DOI 10.1016/j.jmmm.2018.09.107.

[P7] D. Kubániová, L. Kubíčková, T. Kmječ, K. Závěta, D. Nižňanský, P. Brázda, M. Klementová, J. Kohout, "Hematite: Morin temperature of nanoparticles with different size", *Journal of Magnetism and Magnetic Materials* **2019**, *475*, 611–619, DOI 10.1016/j.jmmm.2018.11.126.

[P8] O. Kaman, J. Kuličková, M. Maryško, P. Veverka, V. Herynek, R. Havelek, K. Královec, D. Kubániová, J. Kohout, P. Dvořák, Z. Jirák, "Mn-Zn ferrite nanoparticles with silica and titania coatings: Synthesis, transverse relaxivity, and cytotoxicity", *IEEE Transactions on Magnetics* **2017**, *53*, DOI 10.1109/TMAG.2017.2721365.

[P9] L. Kubíčková, J. Kohout, P. Brázda, M. Veverka, T. Kmječ, D. Kubániová, P. Bezdička, M. Klementová, E. Šantavá, K. Závěta, "Impact of silica environment on hyperfine interactions in ϵ-Fe_2O_3 nanoparticles", *Hyperfine Interactions* **2016**, *237*, DOI 10.1007/s10751-016-1356-8.

[P10] J. Kohout, P. Brázda, K. Závěta, D. Kubániová, T. Kmječ, L. Kubíčková, M. Klementová, E. Šantavá, A. Lančok, "The magnetic transition inϵ-Fe_2O_3 nanoparticles: Magnetic properties and hyperfine interactions from Mössbauer spectroscopy", *Journal of Applied Physics* **2015**, *117*, DOI 10.1063/1.4907610.

Other author's papers

[O1] N. Chistyakova, A. Antonova, V. Rusakov, D. Kubaniova, J. Kohout, T. Kiseleva, M. Chernov, E. Lukyanova, V. Sedykh, D. Zavarzina, "Comparative study of siderites of hydrothermal, sedimentary, and bacterial origin by physical methods", *Crystallography Reports* **2023**, *68*, 459–467, DOI 10.1134/S1063774523700177.

[O2] D. Smržová, P. Ramteke, P. Ecorchard, J. Šubrt, P. Bezdička, D. Kubániová, M. Kormunda, R. Maršálek, X. Vislocká, A. Vykydalová, S. Singh, R. Wathore, V. Shinde, N. Labhasetwar, "Simultaneous removal of selenium and microbial contamination from drinking water using modified ferrihydrite-based adsorbent", *Journal of Water Process Engineering* **2023**, *56*, DOI 10.1016/j.jwpe.2023.104337.

[O3] T. Kmječ, M. Adamec, D. Kubániová, B. Argymbek, J. Plocek, M. Dopita, P. Cejpek, V. Chlan, J. Hraníček, S. Kichanov, K. Závěta, B. Detlefs, M. Cesnek, M. Veverka, H. Štěpánková, J. Kohout, "Magnetic phase diagram, phase transitions, and cation distribution in $Pb_{1-x}Ba_x(Fe_{0.5}Nb_{0.5})O_3$ perovskites", *Materials Science and Engineering: B* **2022**, *278*, DOI 10.1016/j.mseb.2022.115627.

[O4] T. Kmječ, M. Adamec, D. Kubániová, J. Plocek, M. Dopita, M. Cesnek, V. Chlan, J. Bednarčík, K. Závěta, M. Maryško, J. Kohout, "^{57}Fe-enriched perovskites $M(Fe_{0.5}Nb_{0.5})O_3$ (M – Pb, Ba) studied by Mössbauer spectroscopy, NMR and XRD in the wide temperature range 4.2–533 K", *Journal of Magnetism and Magnetic Materials* **2019**, *475*, 334–344, DOI 10.1016/j.jmmm.2018.11.087.

[O5] M. Cesnek, D. Kubániová, J. Kohout, P. Křišťan, H. Štěpánková, K. Závěta, A. Lančok, M. Štefánik, M. Miglierini, "Hyperfine interactions in nanocrystallized NANOPERM-type metallic glass containing Mo", *Hyperfine Interactions* **2016**, *237*, DOI 10.1007/s10751-016-1345-y.

[O6] D. Kubániová, M. Cesnek, O. Milkovič, J. Kohout, M. Miglierini, "Composition of α-Fe nanoparticles precipitated from CuFe alloy studied by hyperfine interactions", *Hyperfine Interactions* **2016**, *237*, DOI 10.1007/s10751-016-1340-3.

[O7] J. Kohout, P. Křišťan, D. Kubániová, T. Kmječ, K. Závěta, H. Štepánková, A. Lančok, L. Sklenka, P. Matúš, M. Miglierini, "Low temperature behavior of hyperfine fields in amorphous and nanocrystalline FeMoCuB", *Journal of Applied Physics* **2015**, *117*, DOI 10.1063/1.4915098.

List of figures

List of tables

List of abbreviations

AAS atomic absorption spectroscopy with flame atomization.

AC alternating-current.

ADC analog-to-digital converter.

AF antiferromagnetic.

CAS Czech Academy of Sciences.

CEMS conversion electron Mössbauer spectroscopy.

CME collective magnetic excitations.

CT computed tomography.

CUNI Charles University.

CXMS conversion X-ray Mössbauer spectroscopy.

DC direct-current.

DFT density functional theory.

DLS dynamic light scattering.

EFG electric field gradient.

FFT fast Fourier transformation.

FPE Fokker-Planck equation.

HRTEM high-resolution transmission electron microscopy.

ICP-MS inductively coupled plasma mass spectrometry.

ICP-OES inductively coupled plasma optical emission spectroscopy.

LAPW linearized augmented plane wave.

LNA low-noise amplifier.

MAR motional averaging regime.

MCS magnetic core-shell.

ME Mössbauer effect.

MPI magnetic particle imaging.

MPS magnetic particle spectroscopy.

MRI (nuclear) magnetic resonance imaging.

MS Mössbauer spectroscopy.

PBE-GGA generalized gradient approximations of Perdew-Burke-Ernzerhof.

SD standard deviation.

SNR signal-to-noise ratio.

SPION superparamagnetic iron oxide nanoparticles.

SPM superparamagnetic.

SQUID superconducting quantum interference device.

STEM scanning transmission electron microscopy.

TEM transmission electron microscopy.

VASP Vienna Ab initio Simulation Package.

VSM vibrating sample magnetometer.

WF weakly ferromagnetic.

WOS Web of Science.

XRF X-ray fluorescence.

XRPD X-ray powder diffraction.

Attachments

A.1 Script for Morin transition fit

```
Clear[data, picture, f, Morin, up, down, nlf, par, par1, TMinf, d, d0, σ, ξ, λ, K, T]
SetOptions[EvaluationNotebook[], DockedCells → {}]
SetDirectory[NotebookDirectory[]];
```

Import of data for fitting procedure, remove first row, properly transform units (e.g.Tesla to Gauss) in such manner that the calculation is dimensionless, and (*switch the columns*), optionally. Data can be trimmed from both sides by modification of "***Take***" function arguments.

```
Clear[datafile, dat1, dat2, dat3, datAF, datWF]
datafile = "TM_α-Fe2O3_all.xlsx";
dat1 = Import[datafile, {"Data", 1}];
dat2 = Take[dat1, {2, Length[dat1]}];
dat3 = dat2[[All, {5, 6, 8, 10}]];
datAF1 = dat3[[All, {1, 2}]];
datAF = Take[datAF1, {1, 17}];
datWF = dat3[[All, {1, 3}]];
ListPlot[{datAF, datWF}, PlotTheme → "Scientific"]
```

Distribution of particle size is fitted by log-normal distribution (see below), which is used in fittation procedure as a weighting function.

```
f[d0_?NumberQ, σ_?NumberQ, d_?NumberQ] := 1 / (Sqrt[2 * Pi] * σ * d) * Exp[-Log[d / d0]^2 / (2 * σ^2)];
```

Fitting functions. Assume Langevin function for superparamagnetic material, or general function for magnetically ordered material, respectively. Change the upper integration limit to cut-off the integration over bigger particles according to your desire. These are not present in the sample and are an artifact from particle distribution fitted by the log-normal distribution, which decays too slowly.

```
up[K_?NumberQ, TMinf_?NumberQ, d0_?NumberQ, σ_?NumberQ, ξ_?NumberQ, λ_?NumberQ, T_?NumberQ] :=
  K * NIntegrate[TMinf * (1 - (ξ / d)^λ) * f[d0, σ, d] * HeavisideTheta[d - ξ],
    {d, ξ * (1 - T / TMinf)^(-1 / λ), Infinity}, Method → "GaussKronrodRule"];
down[TMinf_?NumberQ, d0_?NumberQ, σ_?NumberQ, ξ_?NumberQ, λ_?NumberQ] :=
  NIntegrate[TMinf * (1 - (ξ / d)^λ) * f[d0, σ, d], {d, 0, Infinity}, Method → "GaussKronrodRule"];
Morin[K_?NumberQ, TMinf_?NumberQ, d0_?NumberQ, σ_?NumberQ, ξ_?NumberQ, λ_?NumberQ, T_?NumberQ] =
  If[T < TMinf, up[K, TMinf, d0, σ, ξ, λ, T] / down[TMinf, d0, σ, ξ, λ], 0];
```

Non-linear fitting of given data. It is not possible to display the function as it is calculated numerically at each input call (-> null). Magnetization ***Ms*** is given emu/g, mean particle diameter ***d0*** in nm and polydispersity $\boldsymbol{\sigma}$ is dimensionless.

```
nlf = NonlinearModelFit[datAF, {Morin[K, TMinf, d0, σ, ξ, 1, T],
      {0.93 > K > 0.89, 266 > TMinf > 261 && 120 > d0 > 60 && 0.95 > σ > 0.3 && 10 > ξ > 3}},
    {{K, 0.91}, {TMinf, 264.2}, {d0, 92.2031}, {σ, 0.5}, {ξ, 8.76969}}, T, MaxIterations → Infinity]; // Timing
par = nlf["BestFitParameters"]
par1 = Grid[Transpose[{#, nlf[#]} &[{"BestFitParameters", "ParameterErrors", "AdjustedRSquared", "RSquared"}]],
  Alignment → Left]
Export["TM_α-Fe2O3_morin_MF_par.xlsx", par1, "XLSX"];

K = K /. par;
TMinf = TMinf /. par;
d0 = d0 /. par;
σ = σ /. par;
ξ = ξ /. par;
picture = Show[{ListPlot[datAF, PlotTheme → "Scientific"], Plot[Morin[K, TMinf, d0, σ, ξ, 1, T], {T, 4.2, 350},
    AxesLabel → {T, "Relative Content (%)"}, PlotStyle → {Thick, Blue}]}, PlotRange → {{0, 300}, {-0.05, 1}}]
Export["TM_α-Fe2O3_morin_MF.png", picture, "PNG", ImageResolution → 300] ;
```

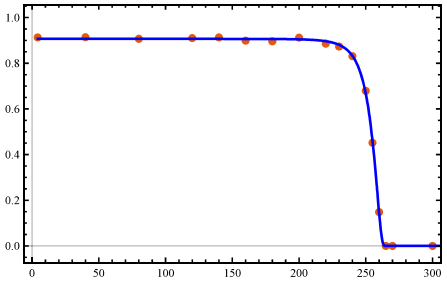

A.2 MPS signal processing

```
Clear[names, par, parAmps, parR35, parR53, parP35, parP53, parPhase,
 parAmpsSort, parR35Sort, parR53Sort, parPhaseSort, parP35Sort, parP53Sort, sorted]
SetOptions[EvaluationNotebook[], DockedCells → {}]
SetDirectory[NotebookDirectory[]];
names = FileNames["*0.csv"]

par = {{"sample", ""}, {"threshold", ""}, {"R35", ""}, {"R53", ""},
    {"", ""}, {"f1", ""}, {"f3", ""}, {"f5", ""}, {"f7", ""}, {"f9", ""}, {"f11", ""},
    {"f13", ""}, {"f15", ""}, {"f17", ""}, {"f19", ""}, {"f21", ""}, {"f23", ""}};
parAmps = {{"sample"}, {"f1"}, {"f3"}, {"f5"}, {"f7"},
    {"f9"}, {"f11"}, {"f13"}, {"f15"}, {"f17"}, {"f19"}, {"f21"}, {"f23"}};
parR35 = {{"sample"}, {"R35"}};
parR53 = {{"sample"}, {"R53"}};
parPhase = {{"sample"}, {"f1"}, {"f3"}, {"f5"},
    {"f7"}, {"f9"}, {"f11"}, {"f13"}, {"f15"}, {"f17"}, {"f19"}, {"f21"}, {"f23"}};
parP35 = {{"sample"}, {"P35"}};
parP53 = {{"sample"}, {"P53"}};
For[i = 1, i < Length[names] + 1, i++,
 Clear[dat0, dat1, dat2, namesy, namesx, backgroundStart,
  backgroundEnd, backgroundAvg, backgroundAvgExport, dat3, dat4, dat5, dat6];
 namesy = StringDelete[ToString[names[[i]]], "0.csv"];
 dat0 = Map[Import[#, "Data"] &, FileNames[namesy <> "0.csv"]];
 namesx = FileNames[namesy <> "*.csv"];
 dat1 = Map[Import[#, "Data"] &, namesx];
 dat2 = Map[Import[#, "Data"] &, FileNames[namesy <> "9.csv"]];

 backgroundStart = dat0[[1]]; backgroundEnd = dat2[[1]];
 dat3 = Take[backgroundStart, {2, 10001}];
 dat4 = Take[backgroundEnd, {2, 10001}];
 backgroundAvg = Transpose[{dat3[[All, 1]], (dat3[[All, 2]] + dat4[[All, 2]]) / 2}];
 backgroundAvgExport = TableForm[backgroundAvg];
 Export[namesy <> "-bg.csv", backgroundAvgExport, "CSV"];
 dat5 = Take[backgroundAvg, {1, 10000}];
 dat6 = dat5[[All, {1, 2}]];

 For[j = 2, j < Length[namesx], j++,
  Clear[dat7, dat8, data, name, signalExport, t, tuples, freq, amps, R35, R53, P35, P53, phas, phase, phases, column,
   columnAmps, columnR35, columnR53, columnPhase, columnP35, columnP53, fourier, fftData, fftExport];
  dat7 = Take[dat1[[j]], {2, 10001}];
  dat8 = dat7[[All, {1, 2}]];
  data = Table[Null, {k, 1, Length[dat8]}, {l, 1, 2}];
  data[[All, 1]] = dat8[[All, 1]];
  data[[All, 2]] = dat8[[All, 2]] - dat6[[All, 2]];
  signalExport = TableForm[data];
  name = StringDelete[ToString[namesx[[j]]], ".csv"];
  Export[name <> "-sg.csv", signalExport, "CSV"];

  time = 0.001;
  tinc = time / 9999;
  sampls = data[[All, 2]];
  nyquist = 1 / (2 * tinc);
  len = Length@sampls;
  prefft = Fourier[sampls];
  fft = Sqrt[4 / len] * Abs@prefft;
  phase = 180 / Pi * ArcTan[Im[prefft] / Re[prefft]];
  freq = 24990; (*Hz*);
  grids[min_, max_] := Table[freq * j, {j, 1, 30, 1}];
  ftics := Table[freq * k, {k, 1, 30, 1}];

  t = Mean[fft[[4800 ;; 5000]]] + 3 * StandardDeviation[fft[[4800 ;; 5000]]];
  peakpositions = FindPeaks[fft, 1, Automatic, t, Padding → "Periodic", InterpolationOrder → 1];
  peakpos = Table[x, {x, 0, (len - 1) / time, (len - 1) / (time * len)}];
  peakfreqs = peakpos[[#]] & @@@ peakpositions;
  amps = fft[[#]] & @@@ peakpositions;
  phas = phase[[#]] & @@@ peakpositions;
  phases = Flatten[MapAt[{# + 180} &, phas, Position[phas, _?NonPositive]]];
  tuples = Transpose[{peakfreqs, amps, phases}];
  ind = Nearest[tuples[[All, 1]] → "Index", {freq, 3 * freq, 5 * freq, 7 * freq, 9 * freq, 11 * freq,
      13 * freq, 15 * freq, 17 * freq, 19 * freq, 21 * freq, 23 * freq}, {1, freq / 3}] /. {} → {25};
  fourier = tuples[[Flatten[ind]]];
```

```
  If[fourier[[2, 2]] / fourier[[3, 2]] < 1, R35 = Null, R35 = fourier[[2, 2]] / fourier[[3, 2]]];
  If[fourier[[3, 2]] / fourier[[2, 2]] > 1, R53 = Null, R53 = fourier[[3, 2]] / fourier[[2, 2]]];
  P35 = fourier[[2, 3]] - fourier[[3, 3]];
  P53 = fourier[[3, 3]] - fourier[[2, 3]];

  ListLinePlot[fft, PlotRange → {{0, 600 000}, All}, DataRange → {0, (len - 1) / time},
    Frame → True, GridLines → {grids, None}, GridLinesStyle → Directive[Red, Dashed],
    FrameTicks → {{All, All}, {All, ftics}}, AspectRatio → 1 / 4] // Print;
  ListLinePlot[phase, PlotRange → {{0, 600 000}, {-90, 90}}, DataRange → {0, (len - 1) / time},
    Frame → True, GridLines → {grids, None}, GridLinesStyle → Directive[Red, Dashed],
    FrameTicks → {{All, All}, {All, ftics}}, AspectRatio → 1 / 4] // Print;
  ListLinePlot[fourier[[All, 3]], PlotRange → {{1, 12}, {0, 180}},
    Frame → True, GridLines → {grids, None}, GridLinesStyle → Directive[Red, Dashed],
    FrameTicks → {{All, All}, {All, ftics}}, AspectRatio → 1 / 4] // Print;

  column =
   Join[{{name, "", ""}, {t, "", ""}, {R35, "", ""}, {R53, "", ""}, {"f (Hz)", "amp", "phase (deg)"}}, fourier];
  Do[par[[i]] = Join[par[[i]], column[[i]], {i, Length@par}];
  columnAmps = Join[{{name}}, Partition[fourier[[All, 2]], 1]];
  Do[parAmps[[i]] = Join[parAmps[[i]], columnAmps[[i]], {i, Length@parAmps}];
  columnR35 = Join[{{name}}, {{R35}}];
  Do[parR35[[i]] = Join[parR35[[i]], columnR35[[i]], {i, Length@parR35}];
  columnR53 = Join[{{name}}, {{R53}}];
  Do[parR53[[i]] = Join[parR53[[i]], columnR53[[i]], {i, Length@parR53}];
  columnPhase = Join[{{name}}, Partition[fourier[[All, 3]], 1]];
  Do[parPhase[[i]] = Join[parPhase[[i]], columnPhase[[i]], {i, Length@parPhase}];
  columnP35 = Join[{{name}}, {{P35}}];
  Do[parP35[[i]] = Join[parP35[[i]], columnP35[[i]], {i, Length@parP35}];
  columnP53 = Join[{{name}}, {{P53}}];
  Do[parP53[[i]] = Join[parP53[[i]], columnP53[[i]], {i, Length@parP53}];

  fftData = Table[Null, {i, 1, 500}, {j, 1, 2}];
  fftData[[All, 1]] = Take[Rescale[peakpos, {0, (len - 1) / time}] * (len - 1) / time, 500];
  fftData[[All, 2]] = Take[fft, 500];
  fftExport = TableForm[fftData];
  Export[name <> "-freq.csv", fftExport, "CSV"];

  ClearAll[picture, r, p, c];
  r = ListLinePlot[fft, PlotRange → {{0, 600 000}, All}, DataRange → {0, (len - 1) / time}];
  p = ListPlot[fourier[[All, {1, 2}]], PlotStyle → {Black, PointSize[0.013]},
    Joined → True, Mesh → All, PlotLegends → Placed[{R35}, {Right, Center}],
    LabelStyle → Directive[Black, Smaller, FontFamily → "Calibri"]];
  c = ListPlot[fourier[[All, {1, 2}]], PlotStyle → {Black, PointSize[0.013]}, Filling → Axis,
    FillingStyle → Directive[Thick, Red], PlotLegends → Placed[{R53}, {Right, Center}],
    LabelStyle → {"f1", "f3", "f5", "f7", "f9", "f11", "f13", "f15", "f17", "f19", "f21", "f23"}];
  picture = Labeled[Show[r, p, c, PlotRange → {{0, 600 000}, All},
     PlotLabel → Style[name, Black, Larger, Bold, FontFamily → "Calibri"]],
    {HoldForm["Amplitude"], HoldForm["Frequency"]}, {Left, Bottom}, RotateLabel → True,
    LabelStyle → Directive[Black, Larger, Bold, FontFamily → "Calibri"]];
  Export[name <> ".png", picture, "PNG", ImageResolution → 150];
  picture // Print;
  fourier // Print
]]
Export["results_fourier.xlsx", par, "XLSX"];
Export["results_amps.xlsx", parAmps, "XLSX"];
Export["results_R35.xlsx", parR35, "XLSX"];
Export["results_R53.xlsx", parR53, "XLSX"];
Export["results_phase.xlsx", parPhase, "XLSX"];
Export["results_P35.xlsx", parP35, "XLSX"];
Export["results_P53.xlsx", parP53, "XLSX"];
parAmpsSort =
  Transpose[Join[{parAmps[[All, 1]]}, Sort[Join[StringCases[Transpose[parAmps][[2 ;;, 1]], DigitCharacter],
       Transpose[parAmps][[2 ;;, 2]]][[All, 2 ;;]]]];
parR35Sort =
  Transpose[Join[{parR35[[All, 1]]}, Sort[Join[StringCases[Transpose[parR35][[2 ;;, 1]], DigitCharacter],
       Transpose[parR35][[2 ;;, 2]]][[All, 2 ;; 3]]]];
parR53Sort =
  Transpose[Join[{parR53[[All, 1]]}, Sort[Join[StringCases[Transpose[parR53][[2 ;;, 1]], DigitCharacter],
       Transpose[parR53][[2 ;;, 2]]][[All, 2 ;; 3]]]];
parPhaseSort =
```

```
  Transpose[Join[{parPhase[[All, 1]]}, Sort[Join[StringCases[Transpose[parPhase][[2 ;;, 1]], DigitCharacter],
       Transpose[parPhase][[2 ;;]], 2]][[All, 2 ;;]]]];
parP35Sort =
  Transpose[Join[{parP35[[All, 1]]}, Sort[Join[StringCases[Transpose[parP35][[2 ;;, 1]], DigitCharacter],
       Transpose[parP35][[2 ;;]], 2]][[All, 2 ;; 3]]]];
parP53Sort =
  Transpose[Join[{parP53[[All, 1]]}, Sort[Join[StringCases[Transpose[parP53][[2 ;;, 1]], DigitCharacter],
       Transpose[parP53][[2 ;;]], 2]][[All, 2 ;; 3]]]];
parAmpsSort[[1, 1]] = "amp";
parPhaseSort[[1, 1]] = "phase";
sorted =
  Join[parR35Sort, {{}}, parR53Sort, {{}}, parAmpsSort, {{}}, parPhaseSort, {{}}, parP35Sort, {{}}, parP53Sort];
Export["results_sorted.xlsx", sorted, "XLSX"];
```

A.3 MPS signal simulation

```
function [tout,Xmean]=run_fokker_planck()

    clearvars;
    clear all; close all; clc;

    %------------------------------ Reality ----------------------------------%

%     drive field DF=25 kHz, amplitude=12 mT
%     selection field (SF) 0-2.5 T/m
%     detection bandwidth <=1.25 MHz
%     linear ramping +B .. 1s measurement in relaxed state .. -B ..1s measurement in relaxed state ..↙
repeat
%     M satur á 0.3 Am2/kg(susp.) of an aliquot of 200 ?l
%     superparamagnetic core
%     dc=8nm
%     PI=0.13
%     dw=10nm ???
%     dh=88nm
%     DLS data confirmed a stabilizing role of the coating polymer
%     The uncoated nanoparticles aggregated even with low elevation of ionic strength and their↙
polydispersity index increased above 0.2
%     The coated particles were stable

    %------------------------------ Variables --------------------------------%

    dc_N = 20*10^(-9);                %Number-weighted mean core diameter (m)
    dh_N = dc_N;                  %Number-weighted mean hydrodynamic diameter (m)
    PIc_Nd = 0.13;                    %Polydispersity index of d-distribution
    PIh_Nd = PIc_Nd;
    PIc_Nv = 3*PIc_Nd;                %Polydispersity index of V-distribution
    PIh_Nv = 3*PIh_Nd;
    T = 300;                                                %Temperature (K)
    eta = 1.0049*10^(-3);                  %Fluid viscosity (Pa.s), Pa=kg/(m.s^2)
    K = 20000;                %Anisotropy constant (Joule/m^3), Joule=kg.m^2/s^2
    Ms = 474000;                           %Saturation magnetization (Joule/m^3.T)
    alphaprime = 0.1;     %Damping constant, 10^-3-10^-2 for bulk, nano smaller
    tau_set = 'neel';                                       %neel OR brownian

    if strcmp(tau_set,'neel')
        N = 50;
    elseif strcmp(tau_set,'brownian')
        N = 30;
    else
        error('Error. \nDefine tau properly.')
    end

    %------------------------------ Driving field ----------------------------%

    drive_field = 'sinusoidal';   % on OR off OR sinusoidal OR lin_ramped
    o1 = 0.015; % Driving field B=B(t) (Tesla), T=kg/(s^2·A)
    o2 = 10000;  % Frequency for 'sinusoidal', Hz
    o3 = 0.000170;  % Ramp time for 'lim_lamped', s
    field_set = {drive_field,o1,o2,o3};

    %------------------------------ ODE set ----------------------------------%

    fp_options = [tau_set,N,field_set,dc_N,dh_N,T,eta,K,Ms,alphaprime];
    tstart=0;
    tend=0.03;       % seconds 0.0000014, 20nm;
    tbreakpoints=[tend/2];   % vector of breakepoints in linspace
%     tspan=exp(linspace(log(tstart+1e-12),log(tend),50)); %[tstart tend];
    tspan=[linspace(tstart,tbreakpoints(1),10),linspace(tbreakpoints(1)+(tend-tbreakpoints(1))/100,↙
tend,100)];
    ainit=zeros(N,1);
    if ismember(drive_field, {'off';'sinusoidal'})
        ainit(1:N)=1;
    end

    cmap = turbo(N); % acts on @odeplot
    colororder(cmap)
```

```
    options = odeset('InitialStep',1e-5,'Stats','on','Refine',1,'RelTol',1e-8,'AbsTol',1e-
10,'OutputFcn',@odeplot);
    sol = ode15s(@(t,a) fokker_planck(t,a,fp_options),tspan,ainit,options);

    %------------------------- Mean x(t) calculation -------------------------%

    tout = tspan;
    aout = deval(sol,tout);
    syms x;
    LP = sym(zeros(N,1));
    S = size(tout,2);
    W = sym(zeros(S,1));
    Wprime = sym(zeros(S,1));
    X = sym(zeros(S,1));
    Xmean = sym(zeros(S,1));

    for li = 1:N
        LP(li) = legendreP(li,x);
    end

    for ti = 1:S
        W(ti) = aout(:,ti)'*LP + 0.5*legendreP(0,x); % 1/2 is the a0(t)*legendreP(0,x)=a0(t) term
        fun = W(ti); % matlabFunction(
        if isreal(W(ti)) % deals with problem of constants are not evaluated as @(x)
           Wprime(ti) = 0.5;
           continue
        else
%         norm = int(fun,-1,1);
% %         norm = integral(fun,-1,1); @(x) USE SYMBOLIC INT!!! DUE TO LIMIT ON
% %         INTERVALS IN USE
%         Wprime(ti) =  W(ti)/norm;
        Wprime(ti) =  W(ti);
        end
    end

    for ti = 1:S
        X(ti) = x*Wprime(ti);
        fun = X(ti); % matlabFunction(
        if isreal(X(ti)) % deals with problem of constants are not evaluated as @(x)
           Xmean(ti) = @(x) 0.0;
           continue
        else
        Xmean(ti) = @(x) int(fun,-1,1);
        end
    end

    %--------------------------- Tau calculation -----------------------------%

    [dadt,M] = fokker_planck(tend,1,fp_options);
    Mmax = max(M,[],'all');
    tau_real = - 1/Mmax *10^6; % (microseconds)
    fprintf('tau = %.4g microseconds\n',tau_real);

    if strcmp(drive_field,'sinusoidal')
        drive_field_period = 1/o2 *10^6; % (microseconds)
        fprintf('drive field period = %.4g microseconds\n',drive_field_period);
    end

    %---------------------------------- Plot ---------------------------------%

    f = figure(1);
    xlabel('t(s)');
    ylabel('Coefficients a_n(t) (n=1..N)');
    if ismember(drive_field, {'on';'off'})
        title(['B = ',num2str(o1*1000),' mT turned ',drive_field,' (',tau_set,')']);
    elseif strcmp(drive_field,'sinusoidal')
        title(['B = ',num2str(o1*1000),' mT',', f=',num2str(o2/1000),' kHz']);
    elseif strcmp(drive_field,'lin_ramped')
        title(['B = ',num2str(o1*1000),' mT',', \Deltat=',num2str(o3*100000),' \mus']);
    end
```

```
    hold on

    for i = 1:N
         hi = plot(tout,aout(i,:));
         h(i) = hi(1);
    end

    legend(h)
    hold off


    figure(2)
    xlabel('t(s)');
    ylabel('<x>');
    ylim([-1 1]);
    if ismember(drive_field, {'on';'off'})
        title(['B = ',num2str(o1*1000),' mT turned ',drive_field,' (',tau_set,')']);
    elseif strcmp(drive_field,'sinusoidal')
        title(['B = ',num2str(o1*1000),' mT turned ',', f=',num2str(o2/1000),' kHz']);
    elseif strcmp(drive_field,'lin_ramped')
        title(['B = ',num2str(o1*1000),', \Deltat=',num2str(o3*100000),' \mus']);
    end

    plot(tout,Xmean(:,1),'Color','black','LineWidth',2);

    %---------------------------------- Fit ----------------------------------%

%     s = fitoptions('Method','NonlinearLeastSquares','Display','iter'); %'StartPoint', [1 1]
%     f = fittype(@(c,tfit,x) c*exp(-x/tfit),'options',s);
%     myfit = fit(tout',Xmean(:,1),f);
%     plot(myfit,tout,Xmean(:,1))

end
```

```
function [dadt,M] = fokker_planck(t,a,fp_options)

    %------------------------------ Define constants -------------------------%
    dc_N = fp_options{7};                                       %Core diameter (m)
    dh_N = fp_options{8};                                       %Hydrodynamic diameter (m)
    T = fp_options{9};                                                 %Temperature (K)
    eta = fp_options{10};                %Fluid viscosity (Pa.s), Pa=kg/(m.s^2)
    K = fp_options{11};                %Anisotropy constant (Joule/m^3), Joule=kg.m^2/s^2
    Ms = fp_options{12};                        %Saturation magnetization (Joule/m^3.T)
    alphaprime = fp_options{13};                                       %Damping constant
    gamma = 1.75*10^11;                  %Electron gyromagnetic ratio (rad/s.T)
    k = 1.3806485*10^(-23);                %Boltzmann constant (kg.m^2/(s^2.K))

    %------------------------------ Calculations -----------------------------%

%     dist_Vc = 1/(sqrt(2*pi)*PIc_Nv*v) * exp( -log(v/Vc_N)^2/(2*PIc_Nv^2) );
%     dist_Vh = 1/(sqrt(2*pi)*PIh_Nv*v) * exp( -log(v/Vh_N)^2/(2*PIh_Nv^2) );

    Vc_N = 1/6*pi*dc_N^3;               %Number-weighted mean core volume (m^3)
    Vh_N = 1/6*pi*dh_N^3;       %Number-weighted mean hydrodynamic volume (m^3)
    m0 = Ms*Vc_N;                          %Magnitude of dipole moment (Joule/T)
    %Characteristic zero-field Brownian relaxation time (s)
    tauB0 = 3*eta*Vh_N/(k*T);
    %Characteristic zero-field Néel relaxation time (s)
    tauN0 = Vc_N*(1+alphaprime^2)*Ms/(2*k*T*gamma*alphaprime);
    alphaK = 2*K*Vc_N/(k*T);                       %Anisotropy contribution ([])

    %------------------------------ Define Matrix ----------------------------%

    N = fp_options{2};

    function V = fill_vector(N,q)
      V = zeros(N,1);
      for n = 1:N
        V(n) = q(t,n);
      end
    end

    function Y = step(X)
        Y = zeros(size(X),'like',X);
        Y(X <= 0) = 1;
    end

    if strcmp(fp_options{3},'on')
        B = @(t) fp_options{4}*heaviside(t);

    elseif strcmp(fp_options{3},'off')
        B = @(t) fp_options{4}*step(t);

    elseif strcmp(fp_options{3},'sinusoidal')
        B = @(t) fp_options{4}*cos(2*pi*fp_options{5}*t);

    elseif strcmp(fp_options{3},'lin_ramped')
        syms ramp(t);
        ramp(t) = piecewise(t<-fp_options{6}/2, -1, -fp_options{6}/2<t<fp_options{6}/2, 2*t/fp_options
{6}, t>fp_options{6}/2, 1);
        B = @(t) fp_options{4}*ramp(t);

    else
        error('Error. \nDefine driving field properly.')
    end

    alpha = @(t) m0*B(t)/(k*T);             %Driving field contribution, B=B(t)
%     fplot(@(t) alpha(t), [-1 1])

    if strcmp(fp_options{1},'neel')
        tau = tauN0;
        A = zeros(N,N);
        B = zeros(N,1);

        s1 = @(t,n) n*(n+1)/(2*tau)*( -1 + n*alphaK/((2*n-1)*(2*n+1)) - (n+1)*alphaK/((2*n+1)*(2*n+3))
```

```
);
        p1 = @(t,n) -n*(n+1)*alpha(t)/(2*tau*(2*n+3));
        u1 = @(t,n) n*(n+1)*alpha(t)/(2*tau*(2*n-1));
        v1 = @(t,n) -n*(n+1)*(n+2)*alphaK/(2*tau*(2*n+3)*(2*n+5));
        w1 = @(t,n) n*(n+1)*(n-1)*alphaK/(2*tau*(2*n-3)*(2*n-1));
        s = fill_vector(N,s1);
        p = fill_vector(N,p1);
        u = fill_vector(N,u1);
        v = fill_vector(N,v1);
        w = fill_vector(N,w1);

        p = p(1:end-1);
        u = u(2:end);
        v = v(1:end-2);
        w = w(3:end);

        A = diag(s) + diag(p,1) + diag(u,-1) + diag(v,2) + diag(w,-2);
        B([1 2]) = [alpha(t)/(2*tau) alphaK/(2*tau)];
        tau_real = (sqrt(pi)/2)*(alphaK/2)^(-3/2)*exp(alphaK/2)*tau*10^6; % (microseconds)

    elseif strcmp(fp_options{1},'brownian')
        tau = tauB0;
        A = zeros(N,N);
        B = zeros(N,1);

        s1 = @(t,n) -n*(n+1)/(2*tau);
        p1 = @(t,n) -n*(n+1)*alpha(t)/(2*tau*(2*n+3));
        u1 = @(t,n) n*(n+1)*alpha(t)/(2*tau*(2*n-1));
        s = fill_vector(N,s1);
        p = fill_vector(N,p1);
        u = fill_vector(N,u1);

        p = p(1:end-1);
        u = u(2:end);

        A = diag(s) + diag(p,1) + diag(u,-1);
        B(1) = alpha(t)/(2*tau);
    end

    %A(  1:1+N:N*N) = diag;
    %A(N+1:1+N:N*N) = +1;
    %A(  2:1+N:N*N-N) = -1;

    dadt = zeros(N,1);
    dadt = A*a + B;    % ODE equations

    persistent Mout
    e = real(eig(A));
    Mmax = max(e,[],'all');
    if isempty(Mout)
       Mout = [];
    end
    Mout = [Mout Mmax];
    M = Mout;    % vector of A eigenvalues for calculation of tau
end
```

A.4 Author's thesis related papers